Laser transmission welding of natural fibre reinforced thermoplastic composites

Rowshni Jabeen

IMT Nord Europe
École Mines-Télécom
IMT-Université de Lille

Université de Lille

THÈSE

présentée en vue d'obtenir le grade de

DOCTEUR

en

Mécanique des solides, des matériaux, des structures et des surfaces

par

Rowshni JABEEN

DOCTORAT DE L'UNIVERSITÉ DE LILLE DELIVRÉ PAR IMT NORD EUROPE

LASER TRANSMISSION WELDING OF NATURAL FIBRE REINFORCED THERMOPLASTIC COMPOSITES

Soutenance le 07 décembre 2022 devant le jury d'examen

Rapporteuse	**CHABERT France, Maître de conférences, HDR**	ENI Tarbes
Rapporteuse	**ROCHA DA SILVA Luisa, Professeur**	Ecole Centrale de Nantes
Examinateur	**DESPLENTERE Frederik, Professeur**	KU Leuven
Examinateur	**LAURE Patrice, Directeur de recherche**	Mines ParisTech
Directeur de thèse	**PARK Chung Hae, Professeur**	IMT Nord Europe
Co-encadrant de thèse	**COSSON Benoît, Maître assistant**	IMT Nord Europe
Co-encadrant de thèse	**AKUE ASSEKO André Chateau, Maître assistant**	IMT Nord Europe

Laboratoire d'accueil
Centre d'Enseignement, de Recherche et d'Innovation (CERI)
Matériaux et Procédés de IMT Nord Europe

Ecole Doctorale SMRE 104 (U. Lille, U. Artois, ULCO, UPHF, Centrale Lille, Chimie Lille, IMT Nord Europe)

Dedicated to

Waheed, Jyothi, Reshma and Nanda.

Acknowledgements

I begin by thanking my thesis supervisor Prof. Chung Hae Park for all your guidance and your immense patience during my time at IMT. Thank you to the pillars of this thesis, Benoît and André for all the encouragement and providing great knowledge for this thesis. It has been a great pleasure working with you.

I express my deepest gratitude to the members of the jury, Prof. Rocha Da Silva, Dr. Chabert, Prof. Desplentere and Dr. Laure for agreeing to be a part of this dissertation and acknowledging my work.

Special thanks go to the project of INTERREG ATHENS for funding this work, and to the team, especially, Leila Bonnaud, Frederik Desplentere and Sofie Verstraete for the collaborations and discussions during the project.

Thank you to my colleagues Xavier and Patrice, who have always come to the rescue when machines pulled tantrums and for being my unofficial french language teachers.

My friends at Douai made my life better than I could ever imagine. Your company kept me strong and I always knew you guys were there for me. Anurag, I can write a new thesis only to describe you and your influence on my life. Thank you for being my 'know-it-all' friend. Amulya, you have a special place in my heart. We vibe! Thank you for being my 'aww-so-caring' friend. Aniket, your stories and your experiences inspire me. Thank you for being my 'this-guy-is-so-amazing' friend. Abhilash (a.k.a Amulya's husband), you are my 'never-say-I-dont-know' friend, you taught me how to show confidence even if you don't know the answer. Thank you Keerthi for being my 'beshht' friend.

A huge shout out to my friends who have accompanied me through the thick and thin in life, Abhilash, Pasha, Uthkarsha, Rinky, Nawaz, Chandu, and Chaitanya. My new family in Europe, Sneha and Kaushik, thank you for giving me great moments and food that I will always cherish.

My heartfelt gratitude to my parents, Waheed and Jyothi, who are the reason for who I am today and for always being proud of me. You both are my true inspiration. Reshma, you are the best sister one can ever have. Thank you for being hopeful and believing that I am here for you. Finally, my sweetheart husband, Nanda, who stood by me in all my emotions during this journey. Thank you Nanda for showering all the love and support and not quitting to believe in me.

Contents

List of Figures

List of Tables

Introduction

The use of fiber-reinforced plastics enables manufacturers in the automotive sector to build light, yet reliable structures. This is in line with the evolution towards minimizing vehicle weight and maximizing payload, for both freight and passenger transport as part of an overarching effort to reduce the ecological footprint of transportation sector.

The optimal technical performance of lightweight structures contributes to their ecological sustainability, but owes to the basic materials used and the production processes used. In this respect, natural fiber reinforced thermoplastic plastic structures offer a solution that is attractive both for its technologically superior performance and reduced environmental impact.

With respect to manufacturers benefiting from the sustainable materials, focus needs to be put on the assembly of individual structures. The use of plastics as a base material by definition allows a number of different joining techniques such as adhesive bonding, welding and mechanical joining.

Project INTERREG ATHENS

This thesis is part of INTERREG Europe. The project name is ATHENS, which is an abbreviation to **Assembly Technologies for Hybrid structurEs of Natural fibre compositeS**. ATHENS is an integrated cross-border collaboration between the Belgian regions of Flanders and Wallonia, and France, aimed at the development of various techniques for assembling bio-composites. This project focuses on two assembly techniques suitable for bio-composites, namely laser transmission welding and adhesive bonding, and addresses related challenges.

The project partners include KU Leuven, IMT Nord Europe, Materia NOVA among others.

The project goals can be construed in three parts:

1. **Optimisation of natural fiber reinforced plastics with respect to assembly** - From the point of view of material composition and industrially applied design processes, natural fiber reinforced plastics are optimized (surface energy, fiber orientation, fibre volume fraction etc.) for both welding and adhesive joining technologies. A synergy between numerical simulations and targeted experiments is provided with respect to material properties crucial for these joining techniques.

2. **Analysis and optimisation of joining technologies** - The focus is on optimisation of process parameters to determine bond strength achieved by adhesives and laser welding. Adhesives are developed and tested on natural fibre reinforced polymers. Process parameters are examined to determine the optimal conditions for each assembly technique. Numerical modelling and mechanical validations are carried out.

3. **Development of demonstrators** - Semi-industrial scale demonstrators are developed that will enable researchers to fully characterize and validate the mechanical performance of both assembly technologies in an industrially relevant manner. The 'know-how' of this project is generated and the optimized joining techniques are intended to be disseminated to a broad industrial network.

IMT Nord Europe carried out a module to model and optimise laser transmission welding of bio-composites. The objective of this module was to optimize assembly technologies for welding of simple structures produced by the other partner KU Leuven. The basic characteristics of the assembly process were identified and compared with the performance expected by the industrial assembly process.

For the joining of thermoplastic composites, the samples were preprocessed according to current industrial best practices (pre-treatment and application). The model of a welding process of composite materials consisting of a thermoplastic matrix and short natural fibres was developed based on IMT Nord Europe's previous works on continuous glass fibre reinforced composite materials.

The motivation of this thesis is to identify the challenges of welcoming bio-sourced composites for laser transmission welding and model the process to allow the industry to adapt it.

Outline of the dissertation

- In chapter 1, the working principle of laser transmission welding is presented. The influence of thermal and optical properties of thermoplastic composites involved in the welding process are discussed, followed by a literature survey of numerical models to approach laser transmission welding.
- In chapter 2, optical properties of short fibre reinforced composites are discussed. The influence of fibres on the propagation of laser beam is investigated and numerically analysed.
- In chapter 3, absorption phenomenon of short flax fibre reinforced thermoplastic composites is studied. Heat transfer analysis is presented to address the attenuation of laser energy that should form a weld.
- In chapter 4, interfacial interdiffusion of polymer chains is studied. Various models to determine healing process in the weld zone are discussed. A model to predict weld strength developed in fibre reinforced composites is proposed, implemented and validated.
- In chapter 5, the dissertation is summarised and recommendations for future works are presented.

Chapter 1

Laser transmission welding of bio-sourced thermoplastic composites

Composite materials offer an advancement to traditional materials such as metal, plastic or wood in terms of strength, weight and environmental impact. Strength of composites is attributed to the reinforcing element in the polymer matrix [1]. It can be designed to exhibit the best qualities of their constituents to produce properties better than the constituents alone possess. Glass fibers are widely used in reinforcing polymeric matrices due to their high strength-to-cost ratio, while carbon fibers are also used frequently for specialty and advanced applications due to their unparalleled mechanical properties. Natural fibers like flax and wood among others, are emerging as low cost, lightweight and environmentally superior alternatives to any synthetic fibers [2]. More importantly, natural fibers uniquely bring about environmental benefits such as sustainable production, CO_2 neutrality, and minimal energy embodiment [3].

As part of industrial need to manufacture complex structures with good mechanical properties, composite materials have contributed a big share. Historically metallic parts in transport could provide all the needs, but weight has always been a drawback. Composite materials, of course could fulfil this drawback. Automotive industry, especially European manufacturers, has been embracing natural fiber composites as reinforcements

in different parts of the automobile. To be competitive, car manufacturers need to increase their responsiveness to market demand fluctuations and variability adaptive to complex assembly systems [4]. Future automotive production systems have to handle a variety of materials and products of various customized geometries [5]. For some products, joining is required due to the limitation of manufacturing complex parts with available resources.

However, the path to manufacture composite parts comes with its own concerns. One of these is, developing a fast and reliable assembly of composite parts. The capability of thermoplastics to melt and consolidate, welding techniques can be considered here as an added advantage. Welding of two thermoplastic composite parts requires a physical contact and sufficient amount of energy at the interface of the substrates to melt the local thermoplastic volume [6].

Many welding techniques are available to join thermoplastics, such as ultrasonic welding, linear vibration welding, hot-tool welding, resistance implant welding and dielectric welding [7, 8, 9, 10]. Welding techniques such as, vibration welding, ultrasonic welding, friction welding, and spin welding uses mechanical movement to generate heat while techniques such as infrared welding, induction welding and microwave welding employ direct electromagnetism to induce heat at the interface.

Laser transmission welding (LTW) is a popular joining process for thermoplastic parts not just in automotive, but also in medical and electronic sectors, especially when the control of heat source location, size and magnitude is critical [11]. Every welding process inherits its own merits and limitations, and are chosen based on the assembly requirements such as joint configuration, cost, speed etc. Laser transmission welding is one of the prominent welding methods that employ external heat source.

Advantages of LTW [12]:

1. Majority of the designs of joints are simple flat-to-flat surfaces.
2. Possibility to generate quick welds, taking < 1 second on an average
3. Non-contact between the user and specimens
4. No vibrations, thus removing the possibility of mechanically induced changes in the structures

5. No particulate generation
6. Precise placement of welds
7. No surface damage
8. Complex shapes possible
9. Localised heating – no thermal damage to sensitive features close to weld
10. Multiple layers can be welded simultaneously
11. Thin or flexible substrates can be welded

Disadvantages of LTW:

1. Expensive compared to other plastics welding equipment
2. Joint surfaces must be of good quality
3. Part clamping must be designed carefully to ensure contact at the whole of the joint area during welding
4. Laser absorbing material must be added to one of the plastics or at the joint surface. The transparent part must transmit the laser radiation efficiently. This can limit the thickness of the top substrate when welding plastics with low transmission (e.g. PEEK or some reinforced plastics)

1.1 Working principle of LTW

A focused laser beam is one of the highest power density sources available to the industry today [13]. LTW uses the ability of light to both penetrate through and be absorbed in a respectively compatible medium. If this process is to be applied to two compatible [14] thermoplastic parts, one of these parts should be transparent to laser wavelength and the other absorbent to the same wavelength. The two parts are clamped together and a laser beam is projected towards their interface (Figure 1.1). The laser beam is transmitted through the transparent part and is absorbed at the surface of the absorbent part, where

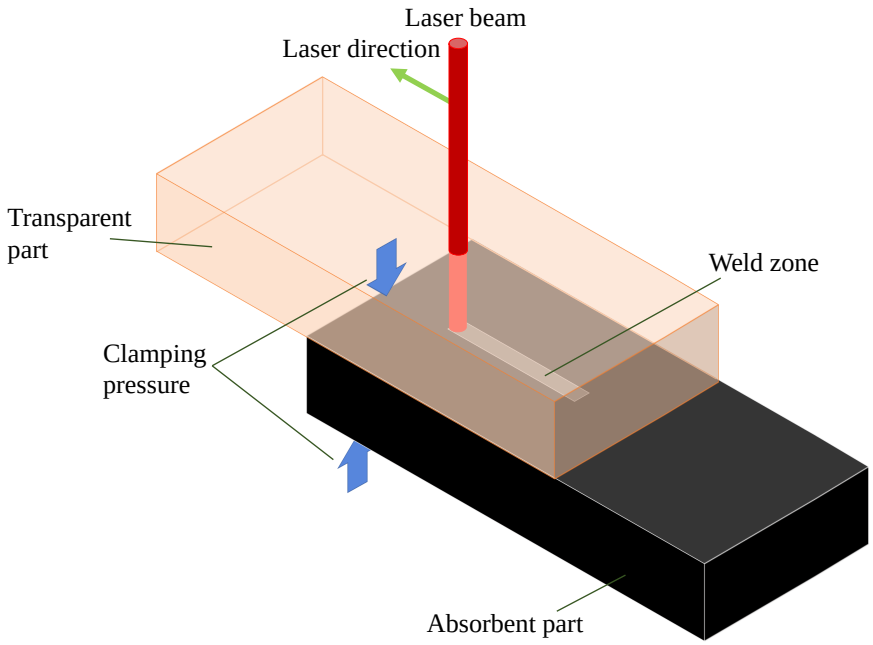

Figure 1.1: Schematic of laser transmission welding

the absorbent part melts locally. At this weld interface, the transparent part also melts locally due to heat conduction. A bond is formed upon solidification. Typically, the materials to be welded are fixed and clamped together, while the laser source moves. The procedure is commonly performed on pure thermoplastics with no reinforcements in the transparent part. This process cannot be performed with thermosets as they cannot be re-fused [15].

Figure 1.2 shows the various steps of LTW. There are four common stages seen during LTW process:

- Positioning of the thermoplastic parts that are to be welded. The two parts are placed in close contact such that the transparent part faces the laser source.
- Transmission of laser beam through the transparent medium and its absorption at the surface of the absorbent medium where the materials melt locally. The heating process may vary based on the part geometry and thermal properties.
- Promotion of interdiffusion of polymer chains in the melted zone and formation of

molecular entanglements.

- Cooling or solidification of the interface resulting in the freezing of the newly formed molecular entanglements and thus forming a weld.

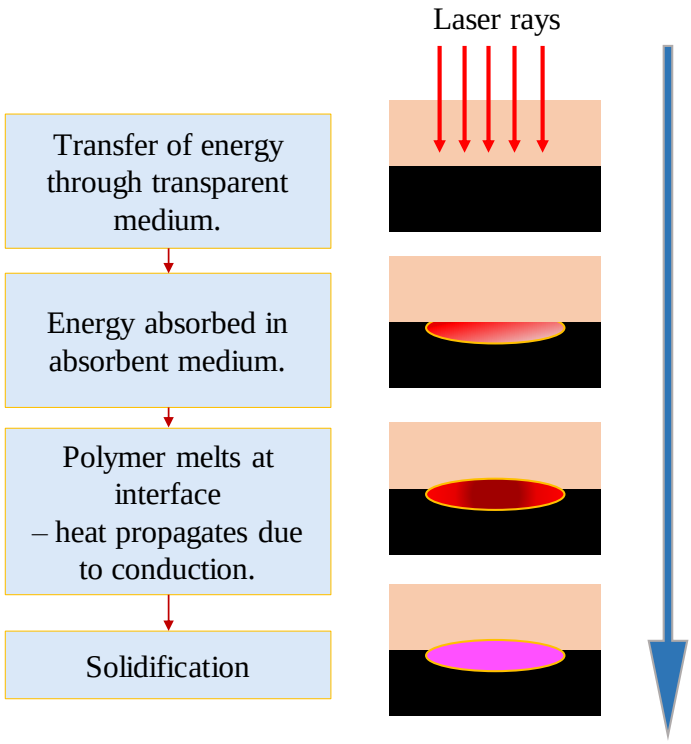

Figure 1.2: Stages of laser transmission welding

Compatible polymers for LTW

LTW can be performed only between compatible thermoplastics that have similar melting temperature profiles, good miscibility and similar melt viscosity. An advantage of LTW is that it is performed rapidly without melting large volume of the plastic part. Under such conditions, the flexibility to combine different polymers increases. In [12], the authors have systematically listed combinations of thermoplastics suited for LTW. In any case, one of the thermoplastics chosen for the LTW process should ensure laser transmission and the other, laser absorption[16].

Laser beam propagation through heterogeneous medium

When fibres are included in the transparent part, it becomes semi-transparent and diffusive. The quality of the weld depends on the interface weld temperature which is impacted by the optical and thermal properties of the composite parts and the welding parameters [17]. During its propagation in a heterogeneous medium, like fibre reinforced composites, the laser beam undergoes reflection and/or refraction at every fibre-matrix interface in their path. This leads to the scatter of laser rays before reaching the weld interface causing a reduction in laser intensity, and hence attenuation in energy reaching the interface [18]. It has been reported that the temperature distribution at the weld seam strongly depends on the local fibre orientation [19].

When the laser radiation reaches the surface of a material, its energy can partly be reflected, or be absorbed. In case of a semi-transparent material, the laser intensity can also be diffused by the constituents of the material and finally, a part of the initial radiation can pass through the volume of the material.

1.2 Parameters affecting laser transmission welding

A good weld has high strength and reliability. Additionally, the two thermoplastics that are to be welded should share properties such as chemical structure and melt temperature in order to achieve a good weld [11].

The strength of a weld line (σ) formed during laser transmission welding is a function of clamping pressure [20], welding temperature and process time [21, 22].

$$\sigma = f(P, T, t) \tag{1.1}$$

The temperature (T) in the weld area should be above glass transition temperature (for amorphous polymers) or melting temperature (for semi-crystalline polymers) of the involved materials to reduce local viscosity and allow inter-molecular inter-diffusion of polymer chains [22]. The materials conduct heat efficiently and diffuse polymer chains while being in an intimate contact with each other. This is achieved with clamping pressure (P) mechanism. Time (t) is evidently a very important parameter that affects the formation

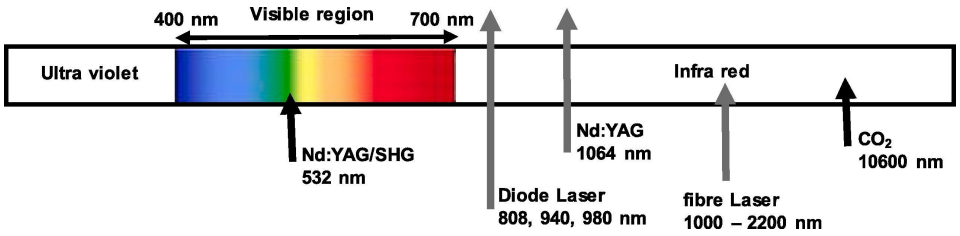

Figure 1.3: Lasers used in laser welding of thermoplastics [23]

of a good weld.

Overall, development of appropriate temperature at the weld interface is of highest interest in LTW. The temperature field at the weld interface is influenced by welding process parameters such as welding speed, laser power, laser beam characteristics, optical properties of the materials and lastly, thermal properties of the materials.

The laser beam interaction with the materials depends on factors such as:

- Type and contents of the material such as additives and coatings
- Laser beam characteristics
- Laser beam intensity, power, size, shape of laser spot, laser beam quality.
- Laser beam speed of movement during welding process (in case of moving laser welding machines).

1.2.1 Laser beam characteristics

Commonly used laser types for welding thermoplastics are Nd:YAG, Diode, Fibre and CO_2 [14]. Laser type influences the quality of the weld as the available lasers differ in wavelength, spot precision and efficiency. Figure 1.3 shows the laser emission wavelengths positioned in the electromagnetic spectrum.

CO_2 lasers

The first laser to be used in welding of thermoplastics was the CO_2 laser in 1970 [24]. The CO_2 laser radiation (wavelength of 10.6 μm) is promptly absorbed at the interface

of the thermoplastic materials enabling the joining process. In CO_2 lasers, the beam is commonly guided from the source to the workplace through mirrors.

Nd:YAG lasers

Nd:YAG lasers are solid state lasers with wavelength of 1064 nm. It is widely used in material processing industry. An optical fibre is usually used to transfer laser to the weld area. For high power requirements, it is feasible to combine multiple Nd:YAG laser beams. These lasers are well suited for high precision welding as the beam spot is relatively small.

Fibre lasers

Fibre lasers have a wavelength range of 1000-2100 nm. In the field of materials processing, much interest has focused on wavelengths around 1,100 nm to provide a replacement for Nd:YAG lasers, with equivalent beam quality, but greater efficiency. In the field of laser welding, the use of fibre lasers has been applied for precision welding of films, textiles and high thickness moulded parts.

Diode Lasers

Diode laser (semiconductor laser) has a wavelength range from 808 to 980 nm. Diode laser welding results in cleaner and stronger joints. The compact design, modular set-up and high efficiency of diode lasers make them more convenient for industrial applications [25]. Diode lasers operate in the Near-InfraRed (NIR) spectral region, where thermoplastics have low intrinsic absorption, implying that the use of this type of laser is highly dependent on the presence of absorbent additives in the thermoplastics. Without the presence of highly absorbing additives, the laser will penetrate the absorbent part without being absorbed.

In the case of diode lasers, the weld spot size is usually not as small as Nd:YAG or fibre lasers. Diode laser is usually sufficient for plastic welding as it is feasible to deliver the energy using a combination of optical fibres and lens system [11]. However, diode laser and its corresponding machinery is relatively affordable. Diode laser is suitable for overlap joints such as lap-joint [26].

1.2.2 Laser power

Laser power is one of the most critical parameters in the laser welding process [27]. Laser power contributes to 58% of the welding process [28]. By increasing the laser power, the heat input at the weld interface increases, and hence the amount of material melted would be more in quantity with an enhanced weld strength. With an increase in laser power, the depth of penetration and weld width increases [29]. However, laser power should be combined with optimal laser speed to form an optimal bond.

1.2.3 Laser speed

Laser speed refers to the movement of the laser beam during LTW. Sufficient time has to be given for melting and inter-diffusion of the two polymer surfaces. This can be controlled by welding speed. The temperature distribution is also crucial for achieving a good quality joint [30].

1.2.4 Focus position

Focus position (or stand-off distance) is the distance between the surface of the materials and the laser module. This parameter affects the weld seam width and temperature distribution in the weld zone.

1.3 Bio-composites

Bio-based polymers are the polymers made from biological sources. Some of these polymers are formed directly in the polymeric form within the producing organisms (ex. micro-organisms, algae, or plants), while others are manufactured ex-vivo from bio-based monomers. It is usually produced from fermentable sugar and vegetable oils. Since 1990, advances in chemical processes and biotechnology have paved way to an increase in the research conducted on bio-based polymers [31, 32].

Polylactic acid (PLA), polybutylene succinate (PBS), Polyhydroxyalkanoate (PHA), and Polyethylene Furanoate (PEF) are some of the bio-based polymers that have received much attention from many industrial players [31]. These new bio-based polymers

have the potential to replace petroleum-based polymers (PE, PP, PS, PTFE etc.) and help solve some of the most urgent problems caused by the overuse of petroleum-based polymers, such as water and soil pollution, deleterious influence to human health, and over-dependence on petroleum [33].

Green reinforcement materials/ natural fibres are derived from plant and animal based biomass. They are classified based on their origin and undergo separation and purification treatment based on their origin. Some of the most common reinforcements are wood, sisal, bamboo, abaca, and cotton. Agricultural biomass extracted from stems include, flax, hemp, jute, kenaf, etc. [33, 34, 35, 36] The main objective to use natural fibres as reinforcement in composites is to improve mechanical properties and produce lightweight materials [37].

Bio-based composites, made from bio-derived polymers and natural fibre reinforcements, are of growing interests in automotive industry. The European automotive industry has been embracing the use of bio composites as vehicle components, due to their low cost, low weight, ease in material availability, and most importantly mechanical characteristics [38]. Moreover, the biodegradability, renewability, non-toxicity, and abundance in nature make natural fibres an ideal reinforcing material for the composites for future utilization in automotive industry [39].

The semi-transparency of a composite depends on the concentration and nature of its constituents. Semi-transparent thermoplastic composites are composed of thousands of fibres embedded in a polymer matrix. Semi-transparency thus appears as the general behavior of matter.

1.4 Interaction between the laser beam and the composite material

Semi-transparent parts with opaque fibres such as flax fibres cause the occurrence of three important phenomena during laser transmission welding: reflection, diffusion and absorption, resulting in the attenuation of the laser irradiation as it passes the composite in a given direction. The deposit of adequate energy at the weld interface is challenging to

control due to the heterogeneity of the semi-transparent part. Local fiber volume fraction, composite architecture, refractive indices of the fibre and matrix, part thickness, are some of the important properties of the semi-transparent part that affect its optical properties [40].

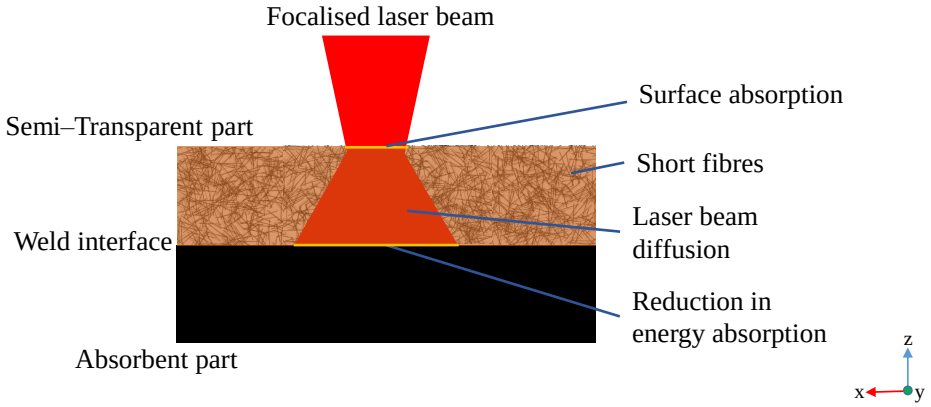

Figure 1.4: Diffusion and absorption of laser energy in semi-transparent part due to the presence of fibres.

Optical scattering in the semi-transparent composite corresponds to deviation of laser radiation from its original path of propagation caused by multiple reflections and refractions in the inhomogeneities of the material. These numerous deviations from the optical path of the medium produce an attenuation of the radiation along the incident direction [41]. M. Ilie et al. [42, 43] have quantified the energy exiting the transparent part using a Monte Carlo method, where the free path of photons are sampled according to a probability density function based on Mie theory.

The energy remaining after transmitting through the semi-transparent part, is absorbed in the absorbent part at a much higher rate due to the presence of laser absorbing fillers in the absorbent part. This causes heating of the local polymer because it absorbs the laser energy at the interface.

In the case of reinforced composites, the energy is partly absorbed in the semi-transparent part. The significance of this absorption depends on the ratio of refractive indices of the fibre and the matrix .

To manufacture an absorbent part for LTW process, the polymer is mixed with fillers

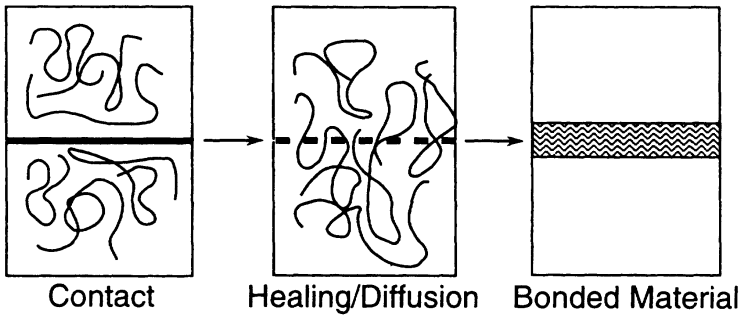

Figure 1.5: Fusion bonding of thermoplastic surfaces [48]

or additives that are absorbent to laser. Fillers such as carbon black, carbon fibres, carbon nanotube and MB black are very common in the industry [44, 45]. These nucleating agents modify the material's thermal, mechanical, and optical properties [46, 19].

Apart from energy loss due to absorption, reflective losses must also be addressed. The reflectivity (η_i) [47] at the interface of the two media having refractive indices n_1 and n_2 is written as

$$\eta_i = \left(\frac{n_2 - n_1}{n_2 + n_1}\right)^2 \tag{1.2}$$

1.5 Formation of a weld

The joining phenomenon of two polymers involves the interfacial reaction between the two surfaces. Figure 1.5 shows the steps involved in formation of interfacial bond by fusion of polymer chains.

Interfacial interdiffusion of polymer chains varies slightly between semi-crystalline and amorphous thermoplastics. Semi-crystalline thermoplastics consists of crystalline and amorphous regions [49, 50, 51]. They have a glass transition temperature (T_g) in the amorphous regions and crystalline melting temperature (T_m) in the crystalline regions. The crystalline melting point is higher than the T_g. These polymeric materials flow above T_m, where no crystalline regions are present [52]. Crystal thickness and topological constraints in the amorphous region define the melting of the crystalline component in semi-crystalline polymers [53]. The chain mobility of the polymer increases above T_m or T_g in the weld region. This allows the chains to diffuse across the joint interface and get

entangled along with the chains of another side of the interface, hence, forming a weld.

1.5.1 Stages of healing

When the temperature at the weld interface is above T_g or T_m, relaxation of the chain conformations occurs towards these chains because of Brownian motion. Gradually, the interface heals leading to the development of mechanical strength. Micro-Brownian motion is followed by the healing process of the polymer chains leading to an interfacial adhesion, thus restoring the original surface contours.

Healing at the interface occurs in five stages according to Wool and O'Connor [54, 55]:

(i) Surface rearrangement

(ii) Surface approach

(iii) Wetting

(iv) Diffusion

(v) Randomisation

During healing, the diffusion stage is considered an essential step controlling the development of mechanical properties. Healing stages are explained through functions such as healing function, wetting distribution function and intrinsic healing function. These functions relate weld strength and weld parameters to temperature, pressure, molecular weight, time and processing conditions. A complete loss of memory of the interface occurs during the randomisation stage. The inhomogeneity at the interface disappears at the end of the diffusion stage. During diffusion and randomisation stages, the polymer chains have more degrees of freedom of movement. Hence, the weld strength at the interface appears during these last two stages[56].

1.6 Modelling of laser transmission welding

Associating welding process parameters to the developed weld strength allows the optimisation of the process. Modeling and simulation combined with experimental research

helps to effectively shorten the process time and efficiently obtain the ideal process parameters [20]. Many methods are available in literature that have modelled LTW process to predict the developed weld strength in similar and dissimilar thermoplastics.

Bates et al. [57] performed finite element method (FEM) combined with a non-linear model-fitting method to study the thermal degradation of Polycarbonate (PC) and Polyamide 6 (PA6) containing carbon black during LTW. The influence of laser power on polymer degradation has been studied, which implied a decline in weld strength.

Mayboudi et al. [58] developed a two-dimensional FEM model to investigate the LTW of PA6. The depth of the heat affected zone and temperature distribution in the weld zone were predicted, The method was extended to a three-dimensional (3D) model to calculate the spatial state changes of materials during the welding process. A MATLAB code was developed to solve the 3D transient heat equation as a function of laser beam dimensions, laser beam power and absorption coefficient of the transparent and absorbent parts [59].

Geiger et al. [60] investigated the effect of absorption coefficient of Polypropylene (PP) on the temperature field distribution and volume of the heat affected zone using FEM. It was concluded that the geometry of molten pool was negligibly affected by the absorption coefficient change with the temperature field.

Labeas et al. [61] developed a 3D thermo-mechanical FE model for LTW process to analyze the influence of process parameters on the real-time welding process by combining multi-physics fields.

Aden et al. [62] modelled LTW process to simulate the temperature field at the weld interface. Interface temperature distribution sourced by Gaussian and M-shaped laser intensity distributions was compared on COMSOL Multiphysics.

Asseko et al. [63] developed an FEM thermal model in uni-directional glass fibre reinforced composites. The laser scattering and absorption phenomena were coupled to predict the temperature distribution at the heat affected zone. The model was developed to determine the ray path during propagation through heterogeneous medium and calculate the absorption coefficient [64].

More approaches to optimize the welding process are found in the literature, apart from FEM. Acherjee et al. [27] used response surface methodology (RSM) to predict the

welding strength and seam width in the LTW of acrylic sheets. The same method was applied to dissimilar plastics welding, Polycarbonate to ABS [65]. RSM has been used to develop empirical models to relate welding parameters to weld strength by performing many experiments with varied parameters. The researchers also studied the distribution of temperature along the depth of materials in the LTW of PA6 using thermal imaging and theoretical calculations [66].

Artificial neural network is a developing tool which has been applied to predict weld strength and weld seam width of laser welded acrylic sheets [67]. ANN is proved to provide a high precision in process optimisation [68]. However, RSM and ANN methods require a history and a database of weld procedure performed with all possible variations of process parameters and materials.

1.7 Determination of weld strength with mechanical tests

Strength development at a weld interface can be analysed with mechanical testing. Mechanical tests help to evaluate healing relations for polymer interfaces [21]. Generally, mode I and mode II fracture tests are performed.

The mechanical energy G required to separate two welded parts is a function of time t, temperature T, contact pressure P and molecular weight of the polymer chains M_W:

$$G = W(T, P, t, M_W) \tag{1.3}$$

where W is the welding function

Following the five healing stages of welding (section 1.5.1), the strength of the bond σ can be expressed as :

$$\frac{\sigma}{\sigma_{max}} = \sqrt{\frac{G}{G_{max}}} \tag{1.4}$$

where σ_{max} is the ultimate strength of the bond and G_{max} is the corresponding maximum energy release rate.

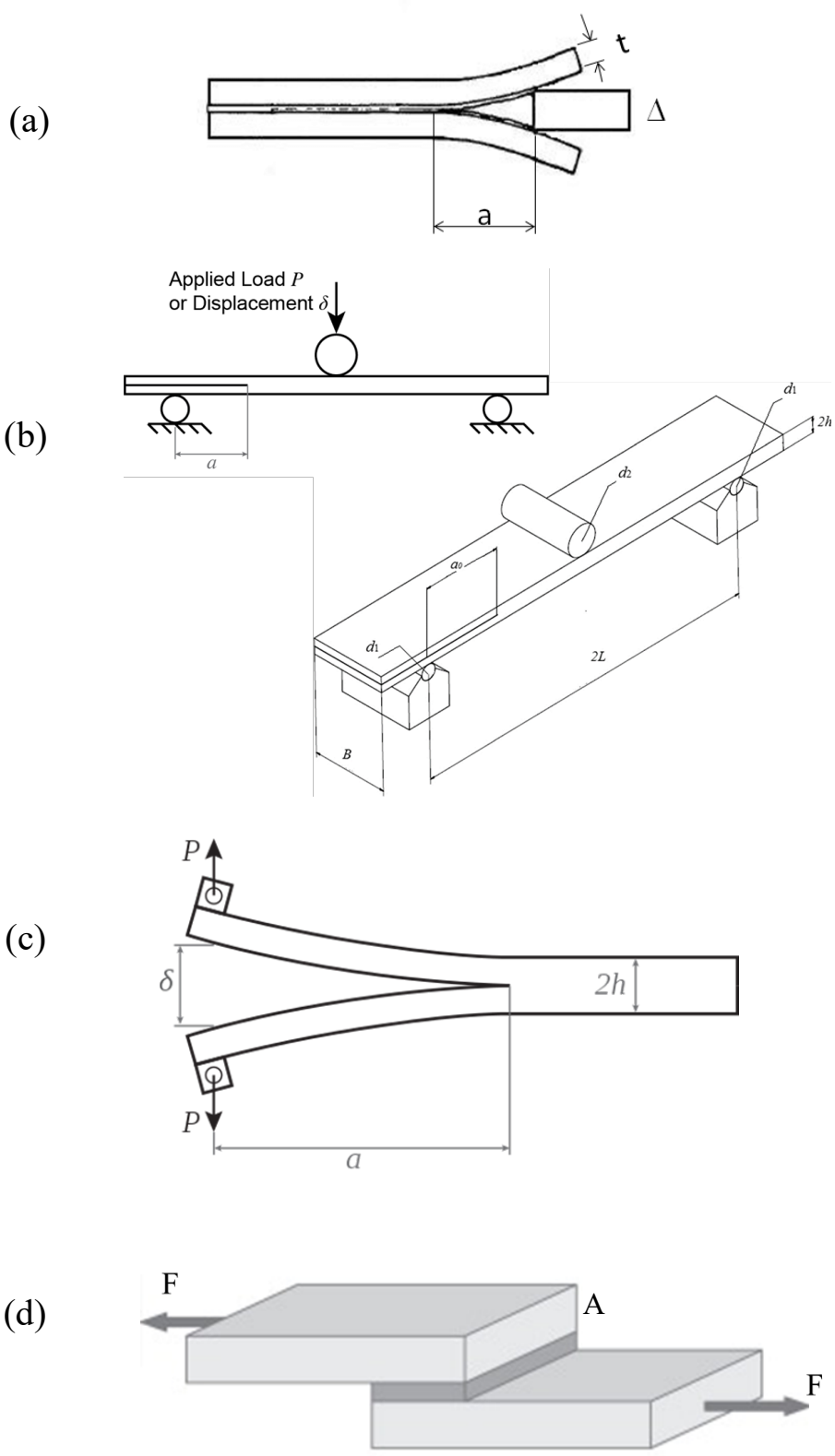

Figure 1.6: Various fracture tests to determine the interfacial bond strength [69, 70, 71, 72]

Mechanical tests, especially shear strength tests, are widely used to measure the mechanical performance of the weld joints. The two most used geometries in laser transmission welding samples are lap-joint and T-joint.

Yan et al. [69] applied wedge test (Figure 1.6 (a)) to characterize the bond strength. It is a mode I fracture test with fracture energy calculated as,

$$G_{IC} = \frac{3Et^3\Delta^2}{16a^4} \tag{1.5}$$

referring to Figure 1.6 (a) where E is the Young's modulus of the materials, t is the thickness of the plates, Δ is the length of the opening, and a is the crack length.

Another mode I fracture test is the double cantilever beam test [70]. This test requires additional support parts to apply load. Figure 1.6 (c) is a schematic of this test. The fracture energy is determined as

$$G_{IC} = \frac{3P\delta}{2B(a+\Delta)} \tag{1.6}$$

where, δ is the displacement of the specimen when a load P is applied, and B is the specimen width. Δ is the crack length parameter, calculated from linear regression of the cube root of the compliance, against the crack length a [70].

End notched flexure (ENF) test requires generation of a weld line at the weld interface along the length of the materials, leaving approximately one-third of the length without a weld. Referring to Figure 1.6 (b), the mode II critical strain release rate with direct beam theory [71] can be written as:

$$G_{IIC} = \frac{9a^2P\delta}{2B(2L^3+3a^3)} \tag{1.7}$$

where L is the half length of the specimen.

Lap shear test is considered one of the most common mode II fracture tests, especially for welded joints. Figure 1.6 (d) shows the schematic of the mechanical test. Here, the weld strength σ_w can be calculated directly as:

$$\sigma_w = \frac{F_{max}}{A} \tag{1.8}$$

where, A is the area of the bonded region and F_{max} is the maximum tensile load.

1.8 Objectives

Figure 1.7: Fusion marks on surface of semi-transparent part

Considering the increasing demand in using bio-composites, it is necessary to study the response of these materials to include them in the joining techniques. The biggest challenge is to acknowledge opaque flax fibres in the process of LTW and study the optical and thermal properties of the composite.

To optimize the LTW process for flax fibre composites, the LTW process must be modelled. For this the temperature field in the heat affected zone has to be analysed. As there is no direct access to measure temperature accurately at the weld interface, numerical simulations should be relied upon.

Studies have shown many models that predict the weld strength in pure or glass fibre reinforced thermoplastics as the diffusion and absorption of the laser energy in the transparent part is within a predicted range. The uncertainty caused by flax fibre composites requires more research to make the prediction. Fortunately, suitable numerical and analytical models are available to apply on Short Fibre Reinforced Thermoplastic (SFRT) composites.

To numerically perform the LTW process on opaque fibre reinforced thermoplastics, the semi-transparent and absorbent parts should also be generated numerically. As the semi-transparent part contains short fibres, a 3D geometry representing the composite should be generated. Ray propagation through the semi transparent part is required to be studied to understand the laser scattering and its effects on the weld formation. This can be done with ray tracing simulations, and a basis for this has already been developed by authors in [64]. Following this, the influence of fibre orientation on laser diffusion can be determined.

Due to the presence of absorbing fibre inclusions in the semi-transparent part, a high loss of energy is expected before the laser beam reaches the weld interface. The absorption is caused by the interaction of laser beam with the fibres. High absorbing semi-transparent part may lead to surface absorption of laser energy, resulting in surface fusion marks. This is shown in Figure 1.7. Hence, absorption in the semi-transparent part needs to be studied and the influence of weld parameters on laser absorption should be determined.

The models available in the literature regarding interdiffusion at the weld interface have to be applied for LTW of composites. The influence of fibres on the formation of weld line can help to predict weld strength in these cases.

Chapter 2

Laser transmission through fibre reinforced composites

During LTW of non-reinforced or glass fibre-reinforced thermoplastics, the absorption phenomenon of laser energy is usually applied only on the absorbent part [73, 74]. The microstructure of the composite induces light diffusion and the energy that reaches the interface is strongly affected in terms of spacial repartition and intensity. This implies that, once the laser beam enters the semi-transparent part, the optical properties of the composite material (refractive indices of the matrix and the fibres) play a vital role in directing the ray path [75]. Hence, the direction of propagation of laser rays is of interest.

Fibre orientation contributes to the mechanical properties of composite materials and hence has been studied in various works, to better define and predict the influence of orientation distribution of fibres on the behaviour of materials [76, 77]. Manufacturing process conditions and matrix flow patterns can be linked to fibre orientation distribution in short fibre-reinforced thermoplastic (SFRT) composites. It has been studied that the temperature distribution resulting in a weld seam has a strong dependency on local fibre orientation [19].

During LTW of thermoplastic composites reinforced with short fibres, a divergence of the laser beam is observed due to internal refraction of the beam at each matrix-fibre interface. This phenomenon leads to the scattering of the laser beam in this heterogeneous medium, resulting in the reduction and spreading of energy reaching the weld interface.

This work presents a numerical study of the effect of fibre orientation in fibre-reinforced composites during the laser transmission welding simulation.

The focus of this chapter is the light scattering that leads to the change in shape and intensity of the laser beam at the weld interface, which further influences the temperature field that forms a weld [78, 63].

A three-dimensional (3D) numerical structure is generated to take into account the microstructure of a composite material reinforced with short fibres. The information of fibre volume fraction, fibre length distribution and fibre orientation distribution are needed to generate the numerical microstructure. This information is extracted by numerically simulating the manufacturing process. In the current context, the manufacturing process used is injection moulding. The fibre orientation distribution function can then be calculated from fibre orientation tensor.

The mechanical properties of composite materials are a function of fibre orientation. Various works [76, 77] have shown the ability to predict the influence of the orientation distribution of fibres on the mechanical behaviour of materials. Manufacturing process conditions and matrix flow patterns can be linked to fibre orientation distribution in SFRT composites. The reflection and refraction of light transmitted through SFRT composites are studied to predict the influence of fibre orientation on laser transmission welding of SFRT.

An algorithm is implemented to trace rays propagating through the composite material. This algorithm uses the optical properties of the composite material to simulate laser beam reflection and refraction in a complex structure. The laser beam scattering at the weld interface is simulated in 3D geometries with various fibre orientation distributions. The effect of fibre orientation on the light scattering phenomenon of laser is compared for different cases of fibre orientation. The simulation results are validated experimentally.

During the injection moulding, flow conditions determine the orientation of short fibres [79]. A common feature of fibre orientation seen in injection moulded parts is the shell-core distribution. The orientation of fibres at the part shell is parallel to the flow, whereas it is perpendicular at the core. Highly aligned fibre orientation is also observed at the inlet and exit of a mould. The direction of fibres within the material strongly impacts the mechanical properties [80, 76, 81, 82]. The influence of the shell-core distribution on

the weld seam properties is studied.

Qualitative measurements of fibre orientation have been carried out by Micro-Computer Tomography (µCT) [83], Fraunhofer light scattering [84], confocal techniques [85], and image analysis [86] among other methodologies. All these approaches have commonly used fibre orientation tensors [87] to describe the fibre orientation distributions. The present work aims to investigate the deviation behaviour of the transmitted light depending on the fibre orientation.

In this chapter, the dependency of light diffusion patterns on fibre orientation is discussed. Firstly, three-dimensional numerical representative volume elements of composite materials are constructed by varying fibre orientations. The fibre orientations are represented using fibre orientation tensors. Ray tracing simulations are performed subsequently, to model the diffusion patterns of the light transmitting through these RVEs. Profiles of the scattered rays are generated at the weld interface and are compared for different fibre orientation states. The simulation results are validated by comparison with experimental results.

2.1 Construction of 3D numerical geometry

To model the diffusion of a laser beam considering the orientation of short fibres, 3D RVEs of a semi-transparent part should be constructed. 3D numerical geometries based on the observations of a real SFRT composite material are constructed by an algorithm developed on MATLAB. This algorithm takes into account fibre morphology such as fibre orientation distribution, fibre shape, fibre volume fraction and fibre aspect ratio [88].

The algorithm loop chooses a random coordinate as the centre of a fibre inclusion in a cube cell with a regular 3D grid. In the beginning, all points of this grid can be chosen as centres of inclusions. The first fibre inclusion is placed at this centre after allocating a fibre aspect ratio and orientation properties to it. The grid coordinates occupied by this fibre inclusion are no more considered for placement of future fibre inclusions. The next fibre inclusion is placed by temporarily eliminating all the grid points occupied by this fibre inclusion if it is to use the coordinates occupied by the past fibre inclusions as the centre. A final centre for this inclusion is chosen randomly from the remaining

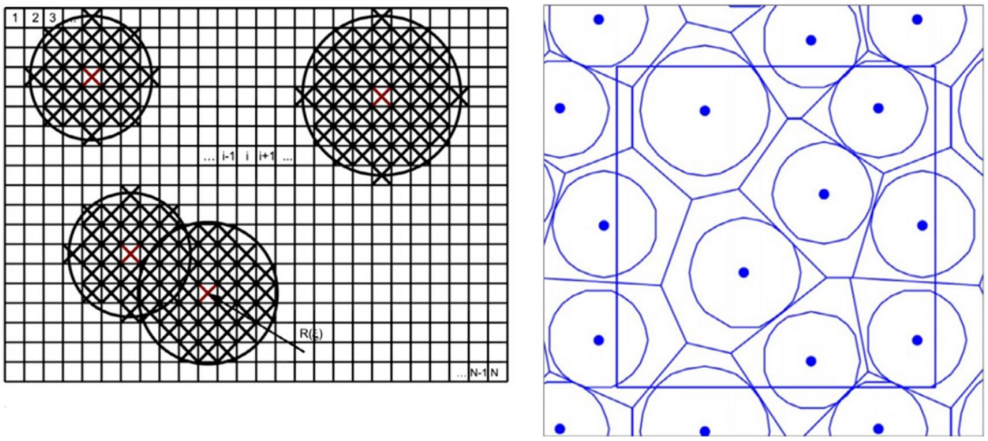

(a) (b)

Figure 2.1: Grid used in algorithm showing (a) inclusion interaction (b) inclusion centres and periodicity [88].

coordinates. The placement of the inclusions in the geometry is done with level sets. This approach (as seen in Figure 2.1(a)) avoids overlapping of the inclusions in the 3D grid as in Poisson's process. This cell is also generated with periodicity (Figure 2.1(b)).

Three-dimensional geometries are constructed according to the following criteria: Fibre shape, fibre length distribution, obstruction to laser transmission, fibre volume fraction and fibre orientation distribution.

2.1.1 Fibre shape

The model creates polyhedrons to represent the fibres in a 3D grid. The algorithm uses the parametrization of an ellipsoid to define the inclusions. Several geometric shapes can be included in the geometry, such as ellipsoids cylinders, cuboids or regular polyhedrons. As the algorithm allows regular polyhedrons to represent fibre inclusions in the numerical geometry, it permits the representation of complex shapes of natural fibres in the geometry with simple modifications. To simplify the simulations in this paper, the fibre shape is selected to be cylinders as are glass fibres[89].

2.1.2 Fibre length distribution

The information on the fibre length distribution in a reference was used in this work. Based on injection moulding simulations of short fibre composites on Autodesk MOLDFLOW, a fibre length and radius analysis was performed by Soete et al. [90]. The average length of the fibres was 500µm and the radius was 100µm. This data is used to define a probability distribution function to assign the length of the fibres in the grid.

2.1.3 Obstruction of the laser beam during transmission

During the numerical simulations, a laser beam is discretized into many rays to trace their paths. Every ray that travels through the numerical geometry should be obstructed at least once in its path to avoid a ray concentration effect. From the viewpoint of the laser source, the generated geometry can be visualised using image processing. In a monochrome image (Figure 2.2), two regions can be distinguished: the black area represents the fibres, and the white area represents the region where the laser beam can travel through the numerical geometry without any obstructions in its path. This criterion intends to construct the RVE while minimising the white areas, to obtain the direction of ray path deviation by imposing at least one interaction between fibres and laser. White lines shown in Figure 2.2 are the outlines of fibres which are represented for the sake of illustration.

2.1.4 Fibre volume fraction

The numerical geometry construction converges to about 99% obstruction (black region) and can not reach 100% without significantly increasing the fibre volume fraction. To reduce the computation cost, convergence is preferred over achieving a full obstruction to ray paths. This also risks allowing a few rays to travel uninterrupted to the weld interface and these rays generate a local heat concentration at the weld interface. This circumstance is also expected, however, during light diffusion with complete obstruction. The fibre volume fraction converges at 29% maintaining the convergence of the black region.

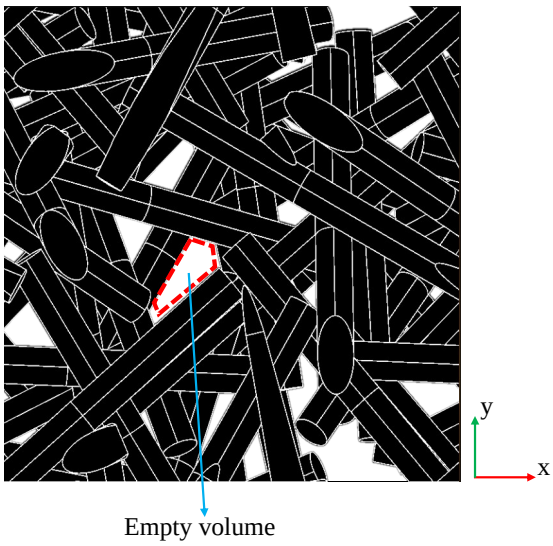

Figure 2.2: Imposition of obstruction to every ray path.

2.1.5 Fibre orientation distribution

The prediction of fibre orientation state using orientation distribution function which is a kind of a probability density function, by F. Folgar and C. Tucker [76] and its extension into use of Fibre Orientation Tensor (FOT) by S. Advani and C. Tucker [87] have been a common approach to investigate the influence of fibre orientation on thermal and mechanical properties of composite materials [91].

The orientation of the fibre inclusions in the numerical geometries is defined using rotation matrices with respect to axes 1 and 3. These angles of rotation are ϕ and θ, and are obtained from fibre orientation tensors. FOTs are simplified descriptions of orientation distribution functions defined by the orientation of a unit orientation vector $\boldsymbol{p}$ with respect to coordinate axes as shown in Figure 2.3. A second-order FOT is written as

$$a = \begin{bmatrix} \langle \boldsymbol{p_1 p_1} \rangle & \langle \boldsymbol{p_1 p_2} \rangle & \langle \boldsymbol{p_1 p_3} \rangle \\ \langle \boldsymbol{p_2 p_1} \rangle & \langle \boldsymbol{p_2 p_2} \rangle & \langle \boldsymbol{p_2 p_3} \rangle \\ \langle \boldsymbol{p_3 p_1} \rangle & \langle \boldsymbol{p_3 p_2} \rangle & \langle \boldsymbol{p_3 p_3} \rangle \end{bmatrix} \tag{2.1}$$

where, the angle brackets denote a configuration average, i.e., an average over the range of $\boldsymbol{p}$, weighted by the probability distribution function for orientation $\psi(p)$.

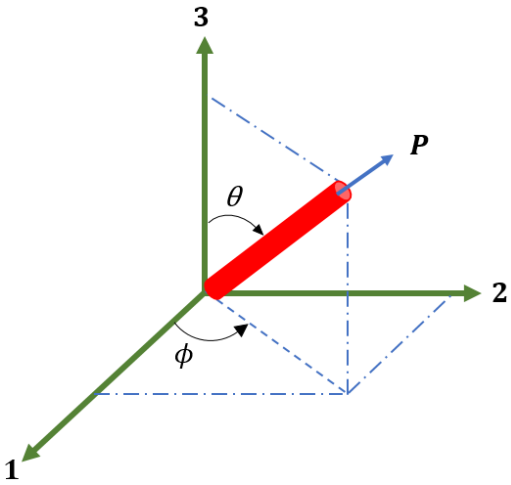

Figure 2.3: Definition of orientation of unit vector P with angles θ and ϕ.

The second and fourth-order tensors are given as,

$$a_{ij} = \oint p_i p_j \psi(\boldsymbol{p})\, d\boldsymbol{p} \tag{2.2}$$

$$a_{ijkl} = \oint p_i p_j p_k p_l \psi(\boldsymbol{p})\, d\boldsymbol{p} \tag{2.3}$$

The components of the orientation of $\boldsymbol{p}$ are written as

$$p_1 = \sin\theta \cos\phi \tag{2.4a}$$

$$p_2 = \sin\theta \sin\phi \tag{2.4b}$$

$$p_3 = \cos\theta \tag{2.4c}$$

The orientation angles can be constricted by applying a symmetry ($a_{ij} = a_{ji}$) to the probability distribution function $\theta \in [0, \pi], \phi \in [0, 2\pi]$, followed by normalisation ($a_{11} + a_{22} + a_{33} = 1$) [79]. Since every fibre must be oriented at some angle and have some length the integral of the function over all angles must be equal to unity.

$$\int_{\phi=0}^{2\pi} \int_{\theta=0}^{\pi} \psi(\theta, \phi)\, sin\theta\, d\theta d\phi = 1 \tag{2.5}$$

Hence, a second-order FOT consisting of 9 elements, has only five independent elements that contain most of the quantitative information about fibre orientation.

To concisely describe the orientation distribution function of the fibre inclusions, fibre orientation tensors are formed. Fibre orientation tensors are defined by forming dyadic products of vector $\boldsymbol{p}$ and integrating the product of these tensors with the distribution function over all possible directions.

The orientation vector $\boldsymbol{p}$ can be used to describe the orientation distribution function, ψ with deviatoric versions (b_{ij}, b_{ijkl}) and tensor basis functions (f_{ij}, f_{ijkl}).

$$\psi(\boldsymbol{p}) = \frac{1}{4\pi} + \frac{15}{8\pi} b_{ij} f_{ij}(\boldsymbol{p}) + \frac{315}{32\pi} b_{ijkl} f_{ijkl}(\boldsymbol{p}) + ... \tag{2.6}$$

Fibre orientation tensors hold information about the orientation which can then be described by the orientation distribution function (ODF). The set of all possible directions of $\boldsymbol{p}$ corresponds to a unit sphere. A second-order tensor is a set of nine elements out of which only six are unique due to symmetry[92].

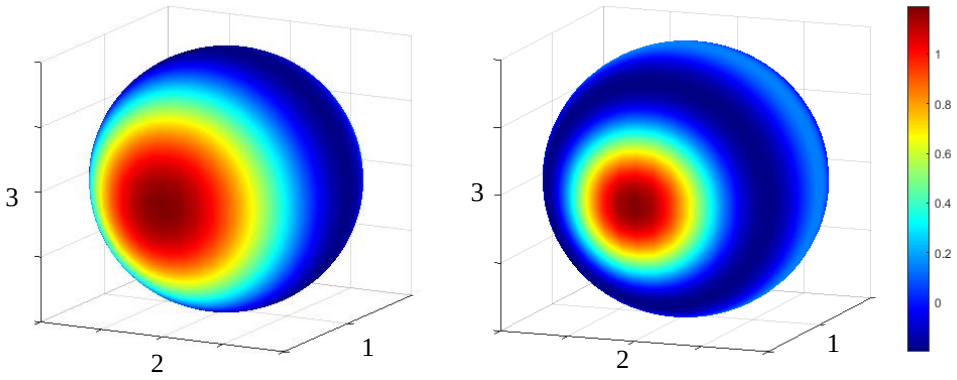

Figure 2.4: Orientation distribution of fibre shown in a unit spheres, generated from fibre orientation tensor with components $a_{11} = 1$ and $a_{22} = a_{33} = 0$. (a) second-order ODF (b) fourth order ODF.

Autodesk MOLDFLOW generates second-order orientation tensors in each numerical element of the injection moulded plate. A drawback of the second-order tensor is the low effectiveness of translating the tensor into an informative ODF. It should be noted that at higher the order of the tensor, the higher the accuracy of the fibre orientation [93].

Figure 2.4 shows that increasing the order of the FOT increases the accuracy. Hybrid closure approximation (a_{ijkl}^{HYB}) [94] is widely used to extend the second order orientation tensor to the fourth order in numerical simulations of injection moulding process [95, 82]. This closure approximation is a sum of two other closure approximations: linear (a_{ijkl}^{LIN}) and quadratic (a_{ijkl}^{QUA}).

$$a_{ijkl}^{\mathrm{LIN}} = \frac{1}{7}\left(a_{ij}\delta_{kl} + a_{ik}\delta_{jl} + a_{il}\delta_{jk} + a_{kl}\delta_{ij} + a_{jl}\delta_{ik} + a_{jk}\delta_{il}\right) - \frac{1}{35}\left(\delta_{ij}\delta_{kl} + \delta_{ik}\delta_{jl} + \delta_{il}\delta_{jk}\right) \tag{2.7}$$

$$a_{ijkl}^{\mathrm{QUA}} = a_{ij}a_{kl} \tag{2.8}$$

$$a_{ijkl}^{\mathrm{HYB}} = (1-f)a_{ijkl}^{\mathrm{LIN}} + f a_{ijkl}^{\mathrm{QUA}} \tag{2.9}$$

where, $f = 1 - 27\det(a_{ij})$.

It has been observed that when using hybrid closure approximation, around 1% of the orientation angles θ and ϕ are out of the expected range of orientation. These samples can be seen in Figure 2.4 (b) as a vertical orthodrome. These angles are not eliminated during geometry generation, in this work. Von Neumann rejection algorithm [96] is used to sample θ and ϕ from the fourth order ODF. A composite microstructure is generated from fibre orientation tensors using the algorithm implemented in MATLAB (See Figure 2.6).

The algorithm is verified by sampling many pairs of orientation angles and constructing a composite geometry by randomly selecting pairs from the samples. Subsequently, orientation angle information is collected from the fibre inclusions in the geometry and an FOT is regenerated from it (Figure 2.6). Comparing the resulting fibre orientation tensor with the initial input fibre orientation tensor, it can be confirmed that more than 99% accuracy is achieved and the method is verified.

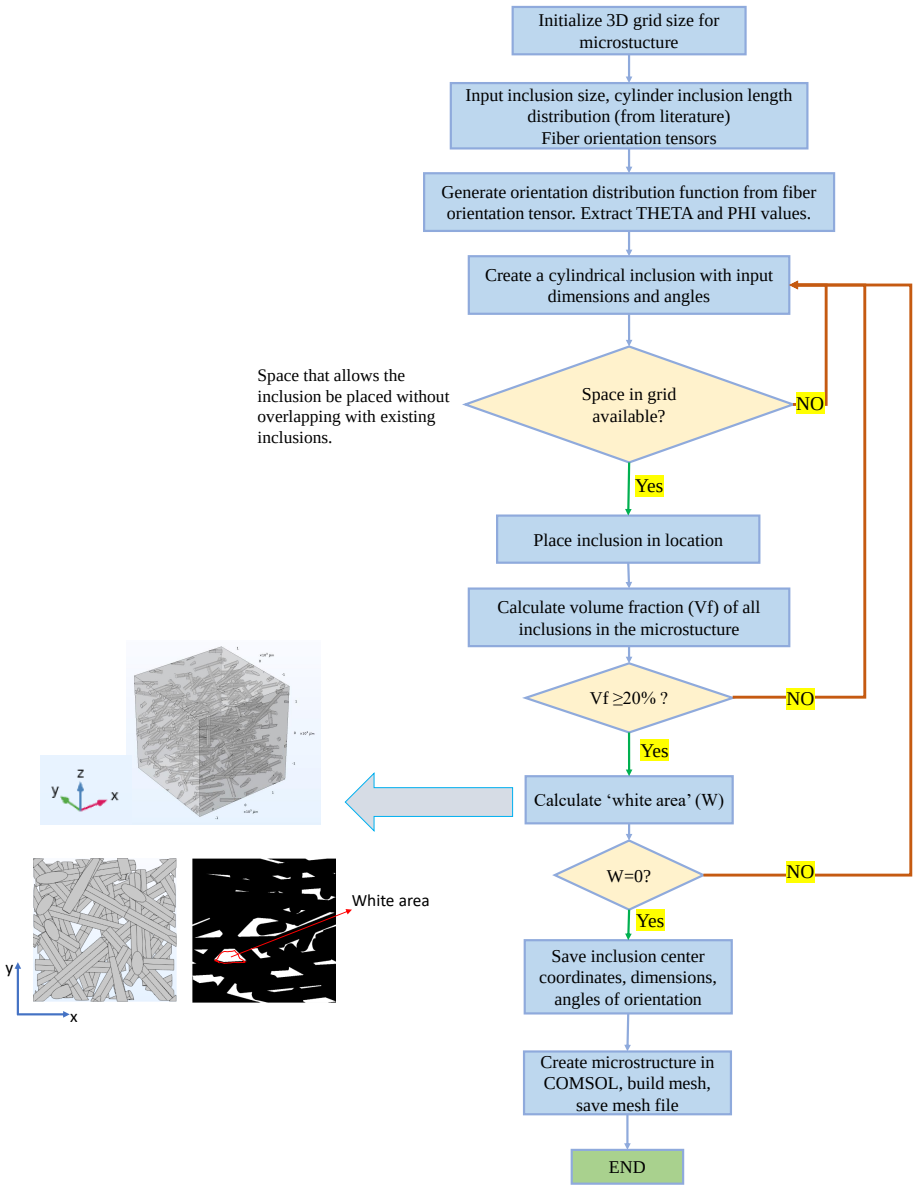

Figure 2.5: Algorithm to generate 3D numerical geometries to perform ray tracing simulation

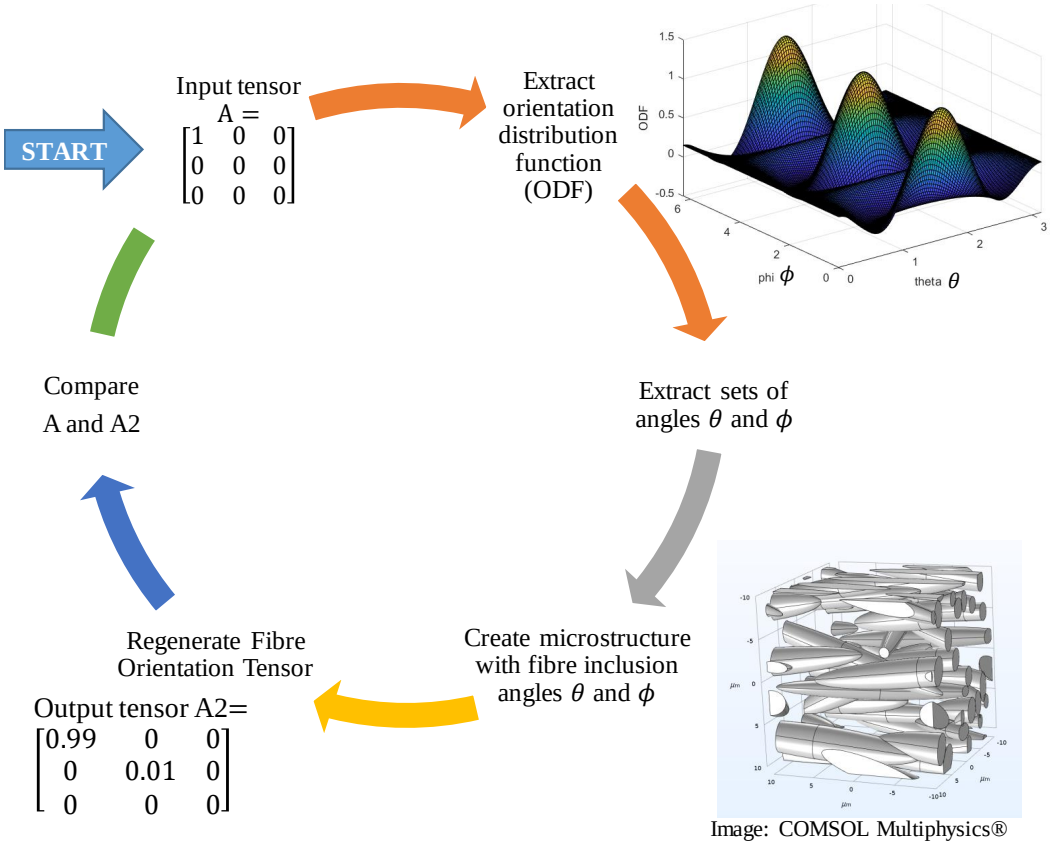

Figure 2.6: Method verification to use fibre orientation tensors to define orientation distribution function.

2.2 Ray tracing method

The Ray tracing method is widely used in the context of computer-generated imagery, which follows the path of a photon emitted from a source to locate the illuminated areas in its environment. The method is based on mathematical algorithms of the intersection of surfaces (illuminated objects) with straight lines in space (photon paths). Ray tracing was first applied in 1883 by Christiansen [97], in the context of radiative calculations. The ray tracing method consists of simulating the real path of the rays emitted by the laser beam and their interaction with the object studied while taking into account reflections and refractions.

The ray tracing method is based on geometrical optics. In a complex medium such as a composite structure, the propagation of laser rays can be simulated using the ray tracing method which is based on the Snell-Descartes law [78].

$$n_1 sin(\theta_1) = n_2 sin(\theta_2) \tag{2.10}$$

where, n_i and θ_i $(i = 1, 2)$ are the refractive indices of the medium i and the angle formed by the ray and normal at the interface (See Figure 2.7). The circular laser beam is discretized into rays which are distributed in a Gaussian or square form.

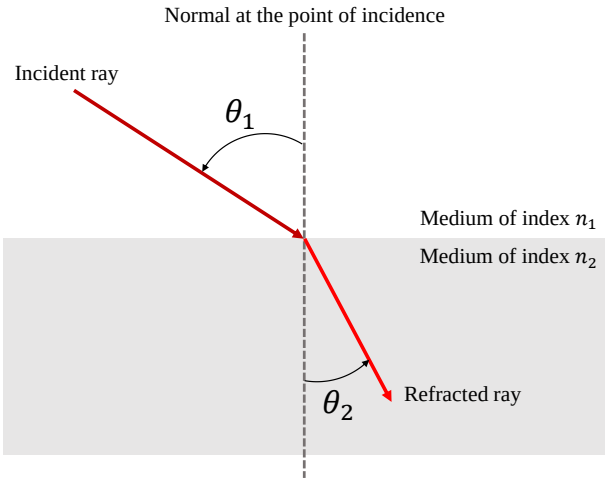

Figure 2.7: Transmission of a laser beam through two different media.

The previously constructed 3D geometry is then meshed with the finite element method. In this heterogeneous medium, the change in path and direction of all laser rays is calculated at each instance of change in the medium at a micro-scale. Each ray interacts with every element in its individual path and changes direction based on the change in the refractive index if the medium is alternated.

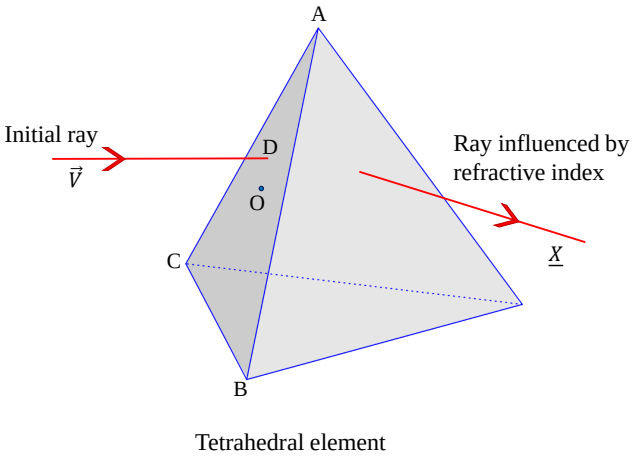

Figure 2.8: Ray tracing simulation at micro scale.

When there is a change in the medium, the tetrahedral element at the intersection plays a role to change the ray direction. The ray enters through one face and its exit face is calculated based on the ratio of the refractive index of the media involved. To find this exit face, the ray tracing simulation tests all the faces of the tetrahedron element into which the ray has entered. For the triangular face (ABC), in an orthonormal frame of reference with any centre O, and a ray entering from point D and direction vector $\overrightarrow{V}$, there is intersection when the following condition is reached (See Figure 2.8).

$$u \leq 1 \,\&\, u \geq 0 \,\&\, v \leq 1 \,\&\, v \geq 0 \,\&\, u+v \leq 1 \,\&\, u+v \geq 0 \,\&\, t > 0 \tag{2.11}$$

$$\underline{X} = \begin{bmatrix} u \\ v \\ t \end{bmatrix}$$

$$\underline{X} = [\overrightarrow{OB} - \overrightarrow{OA}, \overrightarrow{OC} - \overrightarrow{OA}, -\overrightarrow{V}] \setminus (\overrightarrow{OD} - \overrightarrow{OA}) \tag{2.12}$$

where u, v, t are the components of the vector $\underline{X}$ which are calculated by Equation 2.12. The new starting point D is calculated as $\overrightarrow{OD} \rightarrow \overrightarrow{OD} + t\overrightarrow{V}$. The approach is recalled and the direction vector $\overrightarrow{V}$ is recalculated whenever the ray crosses an element face which connects two elements of different refractive indices. In fact, the deviation of rays at the micro-scale is the laser diffusion at a macro-scale [64].

In previous studies [98, 6, 17], the ray tracing method was used to perform simulations of the ray propagation in the semi-transparent part. This method allows for calculating the energy that reaches the weld interface and its location. Even though it is possible to couple the ray tracing method with Beer-Lambert absorption law to determine laser energy lost during the propagation, the absorption in the semi-transparent part is considered to be negligent, in this section.

2.3 Numerical procedure to determine optical diffusion

Once a numerical composite geometry is constructed, it is discretized with an automated mesh generator on COMSOL Multiphysics. Then, numerical simulations are carried out to compute the deviation of the laser rays when transmitting through the semi-transparent medium. The aim is to compare the diffusion patterns of laser rays, for different fibre orientation states. Three numerical geometries with different fibre orientation states are constructed (Figure 2.9).

Out of the three numerical geometries, two (i.e. cases 2 and 3 in Figure 2.9) are constructed using fixed fibre orientation tensors aiming to produce unidirectional fibre orientation with $\begin{bmatrix} 1 & 0 & 0 \\ 0 & 0 & 0 \\ 0 & 0 & 0 \end{bmatrix}$, and randomly oriented fibres with $\begin{bmatrix} 1/3 & 0 & 0 \\ 0 & 1/3 & 0 \\ 0 & 0 & 1/3 \end{bmatrix}$.

Given the incomplete information about the fibre orientation tensor at a lower order, a new numerical geometry (case 1) is generated with perfectly unidirectional fibres. This implies that the tensor $\begin{bmatrix} 1 & 0 & 0 \\ 0 & 0 & 0 \\ 0 & 0 & 0 \end{bmatrix}$, which is expected to align the fibres parallel to axis 1,

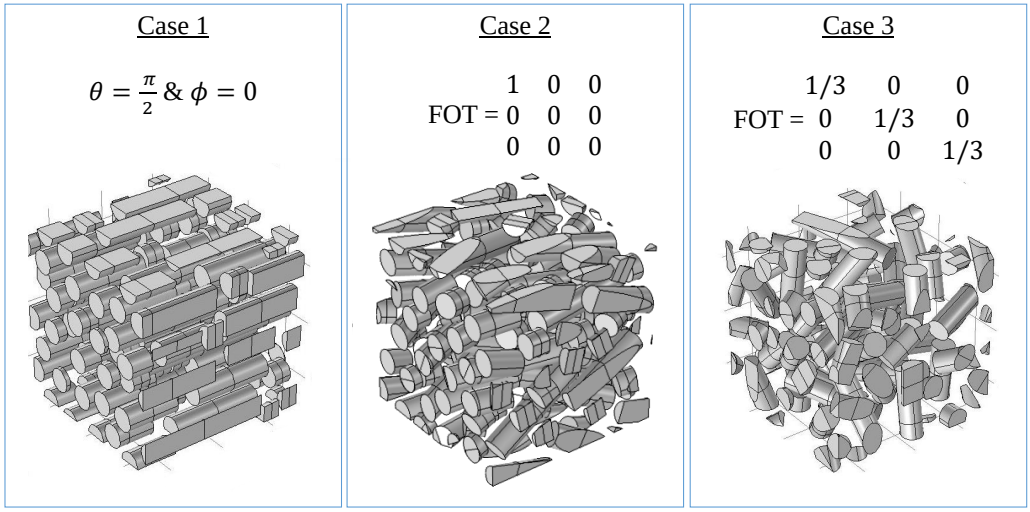

Figure 2.9: Three cases of geometries with varying fibre orientation.

approaches the representation of case 1 only with very high-order tensors. Referring to Figure 2.3, these fibre inclusions are perfectly parallel to axis 1 with orientation angles $\theta = \pi/2$ and $\phi = 0$. Figure 2.10 visualises the orientation of the fibre inclusions in each case of the numerical geometries.

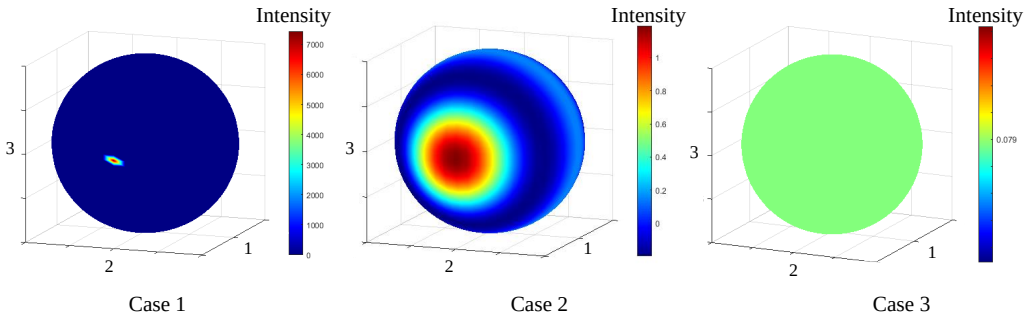

Figure 2.10: Orientation distribution of fibres in 3 cases of geometries.

The mean intensity of rays that reach the weld interface is obtained by gradually increasing the projected number of rays. Convergence is reached at 200000 rays (See Figure 2.11).

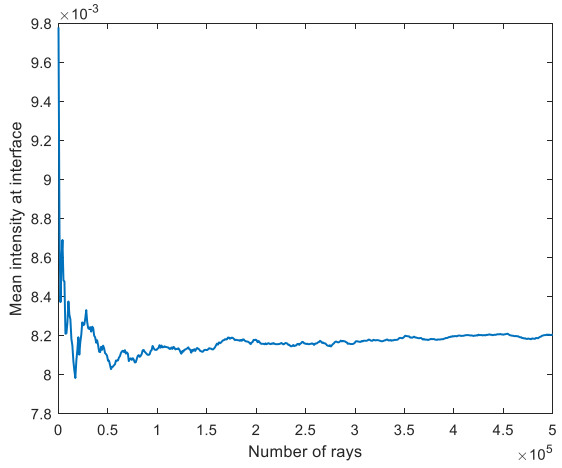

Figure 2.11: Convergence of the number of rays.

Table 2.1: Numerical RVE specifications

Fibre shape	Cylinder
Number of fibres (avg. in 3 cases)	79
Obstruction (avg. in 3 cases)	99 %
Fibre volume fraction (avg. in 3 cases)	28 %
Fibre aspect ratio (avg. in 3 cases)	7.1
RVE cube length	1500 µm
Grid size	50 µm

Table 2.2: Ray tracing simulation specifications

Laser beam diameter	1 mm
Number of rays	200000
Ratio of refractive index (n_{matrix}/n_{fibre})	1.44/1.55
Laser intensity distribution	Uniform distribution
Semi-transparent medium thickness	3 mm
Weld interface dimension	6mm x 6mm

The implemented ray tracing algorithm reduces the computation cost by using periodic geometries. The numerical geometries are repeated multiple times in all directions summing the thickness of the numerical geometry up to 3 mm and the interface surface to a 6 mm x 6 mm plane. The non-focused laser beam diameter is 1 mm and the intensity of the rays is square distributed. The ratio of refractive index of fibre and matrix is varied with 5% as proposed by Cosson et al. [64] as $n_m/n_f = 1.44/1.55$.

2.4 Experimental procedure

To experimentally validate the numerical modelling approaches, glass fibre-reinforced composite plates are used. Two plates with 3mm thickness similar to those numerically generated ones are chosen to project the laser beam through the materials and the shapes of the laser beam diffused on the other surface are captured.

A uni-directional fibre-reinforced composite plate is manufactured with glass fibres and polycarbonate (PC) by filament winding. Owing to the manufacturing process, the fibre orientation is uni-directional [17] and suitably represents the numerical geometry of Case 1 in Figure 2.9. The work also addresses the widening of the laser beam perpendicular to the fibre direction after being projected through the composite plate.

For the other cases, a short glass fibre-reinforced Polylactic acid (PLA) composite with a thickness of 3 mm is manufactured using injection moulding. A simulation with the exact manufacturing conditions is performed on Autodesk Moldflow to determine the fibre orientation distribution. The information about the fibre orientation tensors is extracted layer-wise along the thickness.

A location of 5 mm by 5 mm square on the simulated plate is found to exhibit an

isotropic orientation distribution along the thickness of 3mm (Figure 2.12 (a)). On this square area, each component of the fibre orientation tensor is averaged at each layer, i.e. at each thickness position. Figure 2.12 (b) represents average fibre orientation tensor components a_{11}, a_{22} and a_{33} values along the thickness of the plate in 13 layers.

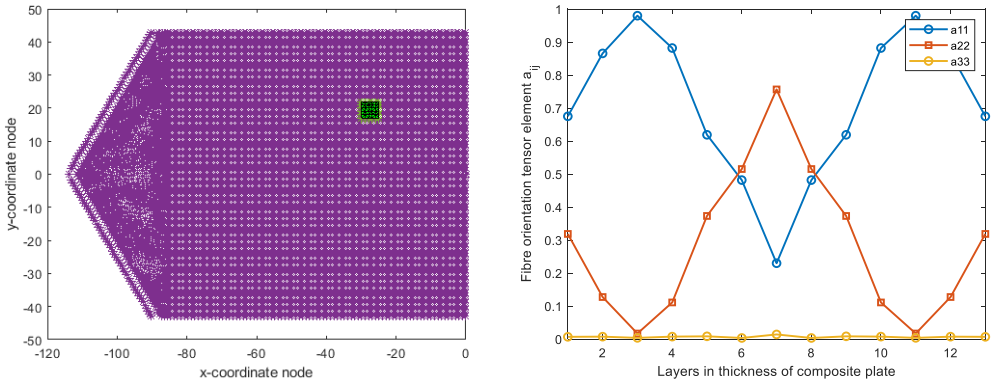

Figure 2.12: (a)Location on injection moulded short-glass fibre reinforced PLA composite for fibre orientation distribution information, (b)Variation of homogenised fibre orientation distribution in thickness of sample plate.

The optical properties of the thermoplastics in the two plates can be easily obtained because both PC and PLA are completely transparent and are commonly used as transparent parts during laser transmission welding [99, 100]. The difference in the refractive index of the fibre and matrix is close to 5% similar to the optical properties input in the numerical simulations. A laser module of 5mW power with a circular beam of 1mm diameter is considered for experimental observations.

2.5 Results and discussion

The result of the ray tracing simulation is the number intensity of the rays and their location after the rays have travelled through the numerical geometry and reached the weld interface. This was demonstrated by projecting 200000 rays of a laser beam of 1 mm diameter into two numerical geometries of 3mm thickness, one with no fibre inclusions

(indicating a pure material) and the other with the fibre orientation tensor $\begin{bmatrix} 1 & 0 & 0 \\ 0 & 0 & 0 \\ 0 & 0 & 0 \end{bmatrix}$. A map of the diffusion of laser rays which have propagated through the two geometries is generated (Figure 2.13).

When there are no fibres in the numerical geometry, the laser rays travel along straight paths showing no signs of scattering. On the contrary, when the rays travel in the composite, the ray paths are disturbed causing a deviation from their original paths. More importantly, it has been observed that the diffusion occurs in the direction perpendicular to the fibre inclusion orientation. Additionally, not all rays reach the target end, as they may have reflected back or refracted out from other faces of the numerical geometry. It is also possible that some of the rays circulated within the numerical geometry in an infinite loop.

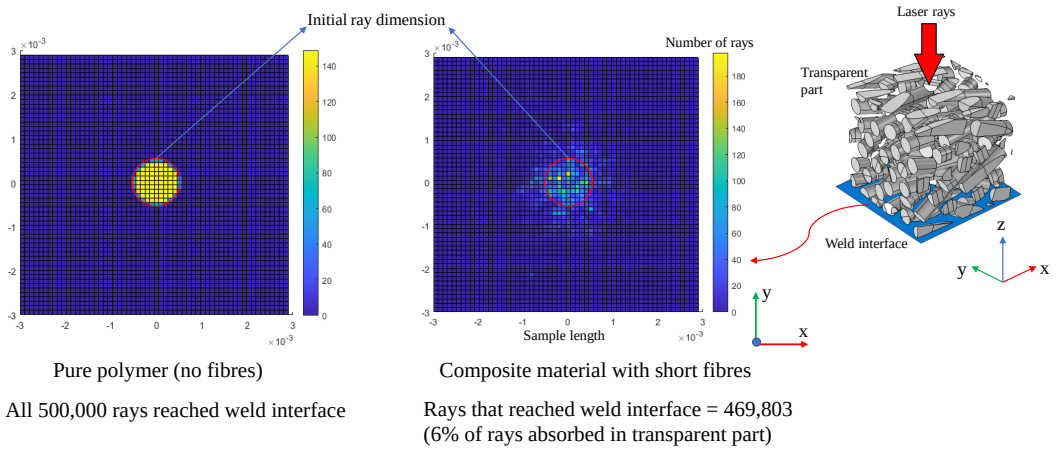

Figure 2.13: Laser intensity distribution at the weld interface.

Figure 2.14 compares the diffusion map of 200000 rays for different orientation states. On average, 160000 rays successfully reach the weld interface in all 3 cases. The other rays have either exited the numerical geometry through the other faces or have refracted inside the numerical geometry in an infinite loop (which implies that the energy of these rays is completely absorbed in the numerical geometry; this case is not considered in this work). Additionally, the influence of 99% obstruction of rays is seen in some parts of Figure 2.14 in red areas. There is a high concentration of laser rays in these areas which

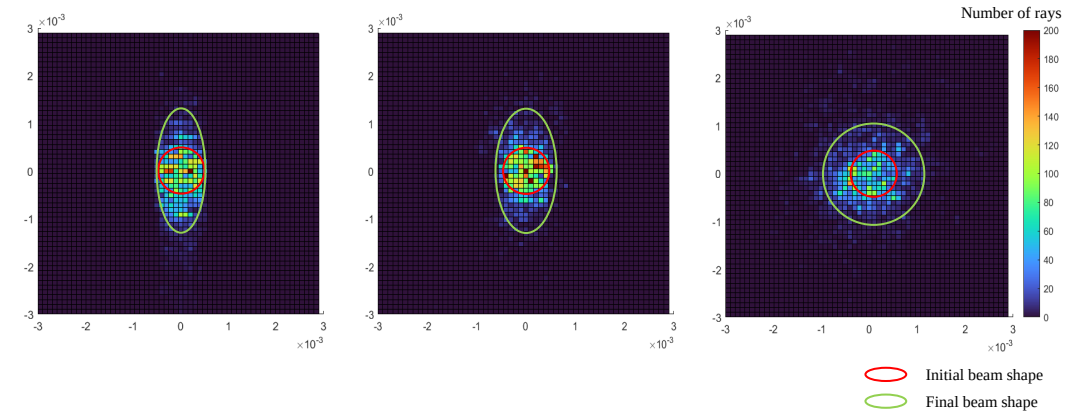

Figure 2.14: Comparison of the three results.

implies that 100% obstructed region is not achieved. The 100% obstruction region results in a high fibre volume fraction and corresponds to high computation costs. Analysing the distribution of rays that reach the exit face of the geometry, it is quite clear in Figure 2.15, that the laser rays have scattered significantly. Especially in Case 1 (perfectly unidirectional orientation, Figure 2.15 (a)), the rays diffuse perpendicular to the fibre orientation. At the location of the fibre interaction, the rays have only two paths for refraction: either the perpendicular or the longitudinal to the fibre direction.

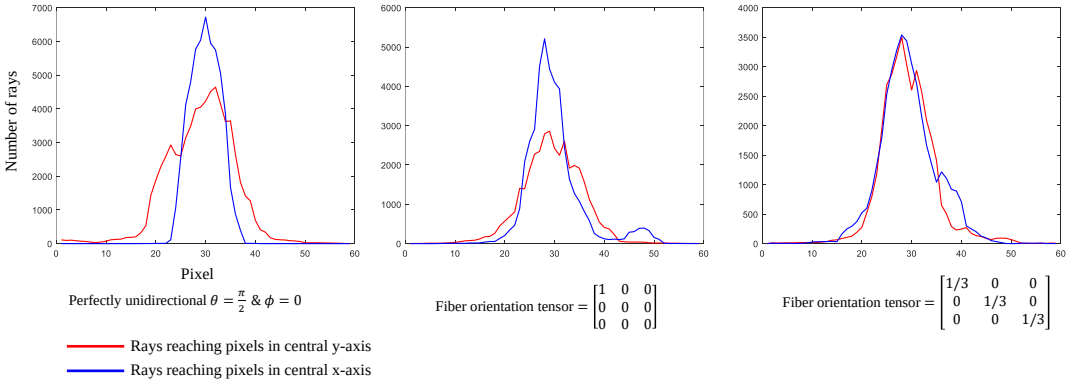

Figure 2.15: Rays at the central lines of the interface in x and y directions.

It is clear that the results for Case 1 and Case 2 should be very similar because the fibre orientation is similar for these two cases. It should be noted that the cylinder shape of the fibres has made the results explicit.

The influence of the low-order tensors is quite evident when comparing the diffusion for Cases 1 and 2. Even if the simulation results are expected to be similar for these two cases, there is a notable difference due to the incomplete fibre orientation information contained in the fourth-order tensor. The slight misalignment of the fibre inclusions has caused the diffusion in the direction of the fibre orientation. It is also possible that the laser rays reaching the ends of the inclusions are free to diffuse in various directions. One such encounter in a ray path could disturb the expected pattern of diffusion at the interface. To verify this, a numerical structure with longer fibre inclusions is constructed and the diffusion pattern is compared (Figure 2.16). The laser ray diffusion is more compacted in the centre with less scatter in the direction of the fibre inclusions. Hence, the length of the fibres influences the diffusion of rays.

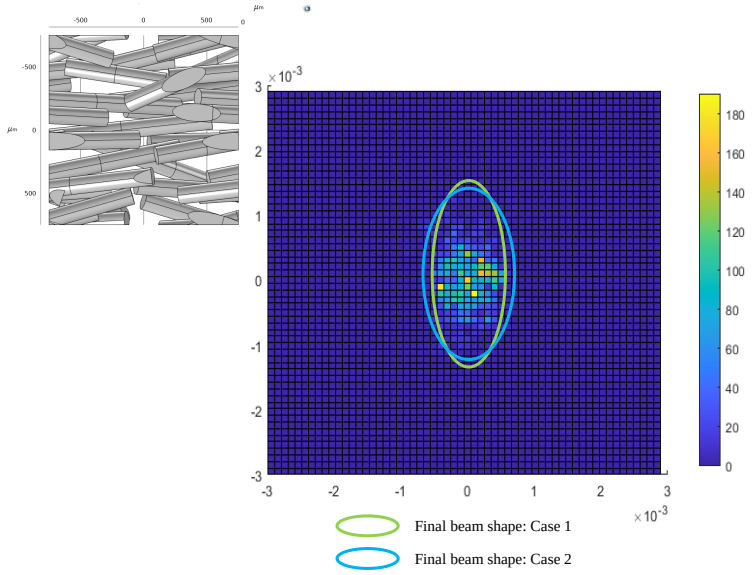

Figure 2.16: Influence of fibre length on laser beam scatter

More disruptions of the ray path lead to greater diffusion of rays. It may be concluded that the ray has propagated in the semi-transparent part by reflecting and refracting, resulting in a significant attenuation of energy before reaching the weld interface. This attenuation can be strongly dependent on the fibre volume fraction in the semi-transparent part. A high number of rays reaching a single location of the interface results in high absorption of energy locally which can lead to the degradation of the polymer. With a

controlled initial beam intensity, it is possible to associate the fibre morphology such as fibre volume fraction, fibre shape, fibre length and fibre orientation to the optimal weld parameters such as laser beam intensity, laser diameter and laser beam speed. An increase in fibre volume fraction decreases the possibility for a laser beam to propagate through the material without scattering [101].

The simulations for Cases 1 and 3 were validated experimentally by projecting a laser beam through composites with similar fibre orientation. Figure 2.17 shows these two cases with glass fibres. The initial shape of the beam was observed by projecting the laser through a thin paper and a picture was captured from the other end with a digital camera (Figure 2.17 (a)). Replacing the paper with unidirectional and randomly oriented glass fibre reinforced composite plates, the laser beam shapes as shown in Figure 2.17 (b) and (c) are observed respectively. Evidently, unidirectional fibre composite diffuses the laser beam in the direction perpendicular to the fibre direction, which corresponds to the ray tracing simulations result. It is also seen that the random fibre orientation of fibres diffuses the laser in all directions which are also similar to the simulation result.

It should also be noted that the ratio of refractive index greatly influences the quantity of diffusion. The dimensions of the diffused laser spot can be altered by changing the optical properties of the fibres. Replacing the glass fibres with more opaque fibres such as flax, the diffusion can be expected to be greater [64]. The energy absorption at the weld interface can be expected to be lower, even if the energy absorption in the semi-transparent part is neglected.

2.6 Conclusion

The influence of the fibre orientation on the laser beam diffusion was numerically modelled. The distribution of the laser energy that reaches the weld interface can be used for FEM simulations to compute the temperature field at the weld interface, which is helpful for the optimisation of laser transmission welding of composites. A numerical model to generate microstructures representing composite materials considering fibre volume fraction, fibre shape, fibre length and fibre orientation was developed. Considering the influence of fibre orientation on both the mechanical properties and the laser welding quality, it is

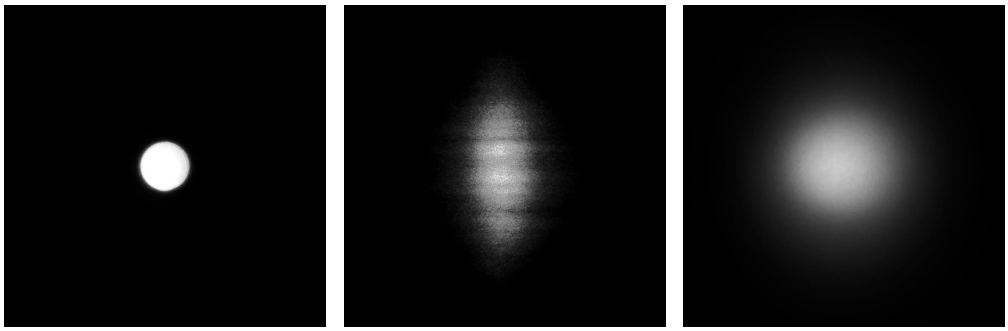

(a) (b) (c)

Figure 2.17: Laser beam shape after propagating through (a) thin paper, (b) unidirectional glass fibre reinforced composite, and (c) randomly oriented glass fibre reinforced composite.

significant to take into account the real fibre orientation in the simulation of the laser welding process.

Chapter 3

Heat transfer analysis

3.1 Introduction

During laser transmission welding, the extent of melted polymer volume at the weld interface depends on the quantity of energy delivered between the materials to be joined. Insufficient energy will not melt the material at the interface, whereas, a high amount of energy may break cohesion between fibres and matrix or cause deformations [41]. As seen in the previous chapter, the transmittance of the laser energy is influenced by the obstructions in the laser path. The problem is therefore not confined only to welding process parameters such as the laser wavelength and the laser power. Optimization of the process parameters, depending on the optical and thermal properties of the involved materials is required to avoid poor weld quality [61]. This can be done by linking the weld interface temperature field to the welding process parameters and relevant material properties.

A 3D transient thermal model of LTW is considered to obtain the temperature field between the assembly of substrates by solving the energy balance equation:

$$\rho C_p \frac{\partial T}{\partial t} = -\nabla.(-k\overrightarrow{\nabla}T) + Q \tag{3.1}$$

where ρ is the material density, C_p is the specific heat, T is the temperature, t is the time, k is the thermal conductivity, Q is the heat source and ∇ is the gradient operator.

To model the heating phase, firstly, a comparison between the intensity of the initial

laser beam and that of the rays that have reached the weld interface must be carried out. This allows a better understanding of how specific materials behave during laser transmission welding. For semi-transparent composite materials, a substantial portion of the light transmitted through the material may be deflected from the incident beam direction, reducing the energy density at the interface. Furthermore, the effective laser beam path length is now greater than the actual part thickness, thereby increasing the part absorbance and decreasing laser transmission. It is therefore critical to assess the strength of the reinforcements in the composite material [102].

Generally, laser energy absorption is considered only at the weld interface and in the absorbent part [42, 43, 63]. These analytical approaches take into account the Beer-Lambert law to calculate the intensity profile during laser propagation through the semi-transparent part.

$$I = I_0 e^{-Kd} \tag{3.2}$$

where I_0 is the initial intensity of the laser beam, K_h is the absorption coefficient of the material, d is the distance travelled by the laser beam in the material and I is the laser the final laser intensity at the weld interface. This relationship indicates that the laser beam scattering attenuates laser intensity exponentially [44]. This mathematical function is not applied to intensity magnitude but to the total laser power and the parameter of the exponential term is the absorption coefficient.

Beer-Lambert law has been commonly applied to the absorbent part only, while the absorption in the assumed transparent part is neglected [73]. This is considered an ideal situation during laser transmission welding [40]. The heat source in these cases of welding is described with the following equation:

$$Q(x,y,z) = \begin{cases} 0 & \text{for } z < d_t \\ I(x,y) \times K \times e^{-K \times d_t} & \text{for } z > d_t \end{cases} \tag{3.3}$$

where d_t is the thickness of the (semi-) transparent part and z is the coordinate axis parallel to the direction of the laser beam. The absorption coefficient is hence considered infinite for the absorbent part. Generally, the intensity distribution at the weld interface is assumed to retain the initial shape of the laser source beam. This assumption can no

longer be applied in this work due to the heterogeneity of the semi-transparent composite material.

By considering the calculations of distances travelled by the rays in the semi-transparent part, and then applying a volumetric heat generation expression according to Beer-Lambert law, one can determine the source term in the heat equation, Eq 3.1. The model takes into account both maximum attenuation and the standard deviation of the expansion of the energy distribution into the semi-transparent part. This method requires homogenized coefficients of composites which have to be determined beforehand.

The thickness of the semi-transparent composite materials is one of the factors that affect the absorption of energy in the part. As the thickness of the semi-transparent part increases, the attenuation of initial intensity caused by the diffusion of the laser rays also increases [103]. Though absorption is a function of laser wavelength [38], the laser module is not changed in this work.

3.2 Absorption of energy in semi-transparent part

Glass fibres in semi-transparent parts only induce a scatter of the laser rays and reflection, but do not absorb the laser radiation. Replacement of glass fibres with any other fibres results in an additional phenomenon of absorption [104]. Due to the high opacity of flax fibres, high laser diffusion is seen in the semi-transparent part, leading to energy absorption within the semi-transparent part. Apart from the reflection and refraction of the laser rays, energy absorption now hinders the transmittance of total laser radiation to the weld interface. This results in a non-homogeneous weld line due to non-uniform energy distribution on the weld line. Hence, the opacity of flax fibres in the semi-transparent part alters its optical properties necessary for a good weld line quality.

Additionally, a high amount of energy may be absorbed at the surface of the semi-transparent part. Figure 3.1 shows one such case, where burn marks on the surface of a short flax fibre reinforced PLA composite are seen. This burn mark is caused due to absorption of laser energy that is enough to reach melt temperature. In other words, this energy could have contributed to the formation of a better weld line at the weld interface if it was not captured at the surface. The radiation that was absorbed neither at the

surface nor within the semi-transparent part may not be sufficient to melt the polymer at the weld interface causing a bad weld or no weld at all.

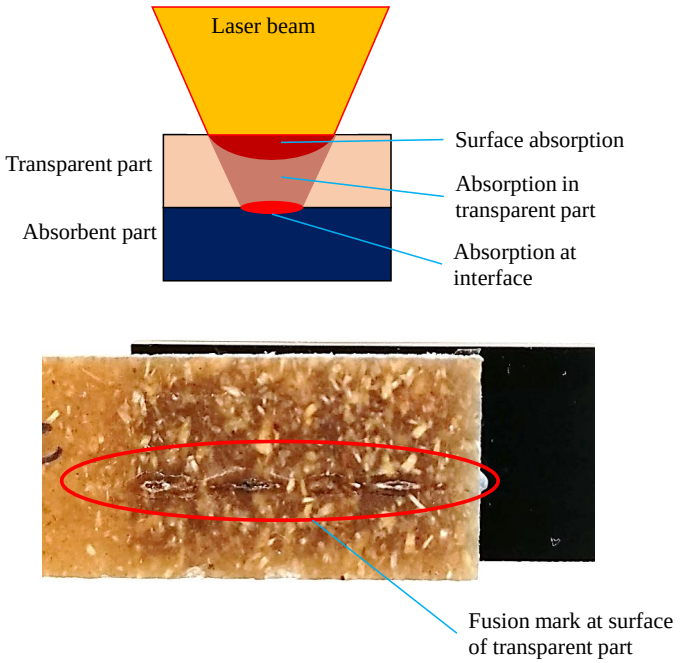

Figure 3.1: Volume and surface absorption in semi-transparent part

Hence it is crucial to understand the aspects that cause the surface fusion marks and the weld parameters that can reduce the surface absorption. Firstly, to apply the Beer-Lambert law, the total length of the ray path much be taken instead of the part thickness [64]. The term K_h is the homogenised absorption coefficient of the semi-transparent part. The ray tracing simulation is carried out with the same physics as seen in the previous chapter, but with a few modifications. In addition to following the path of each laser ray, the simulation records the total distance travelled by the rays at a micro-scale.

3.3 Experimental procedure

As explained earlier, one of the parameters of a laser transmission welding machine is the focus position. Multiple experimental tests are performed to determine the effect of focus position on the formation of burn marks. This study aims to investigate the effect

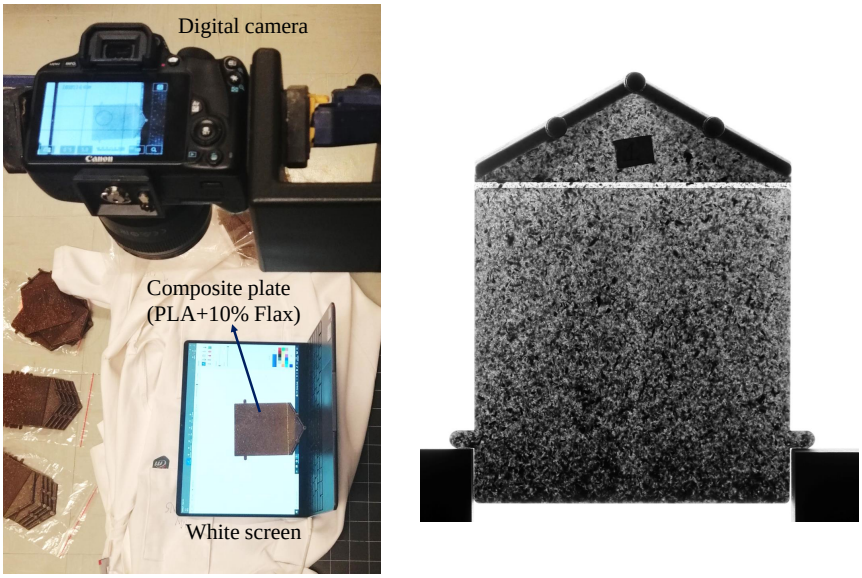

Figure 3.2: Image capturing of fibre distribution in a semi-transparent plate.

of focus position on the absorption of laser radiation and find an optimal focus position to maximise absorption at the weld interface instead.

3.3.1 Materials

To manufacture the composite plates, flax fibres with polylactic acid (PLA) are chosen to emphasize on bio-sourced materials. For the experiments, a composite plate with PLA and short flax fibres is taken as the semi-transparent part and a pure PLA plate with 1% MB Black is taken as the absorbent part. Both the plates are 3 mm thick with dimensions of 80 mm x 80 mm. The plates are cut into multiple samples for welding, with dimensions 18 mm x 80 mm.

The fibre volume fraction (v_f) of the semi-transparent part is 10%. The plates are manufactured by injection moulding. The overall fibre orientation across the plate thickness can be considered isotropic [105]. However, the fibre distribution in the plate is heavily influenced by the flow conditions of the materials during injection moulding. Due to this, weld line properties are predicted to differ in different regions of the plate.

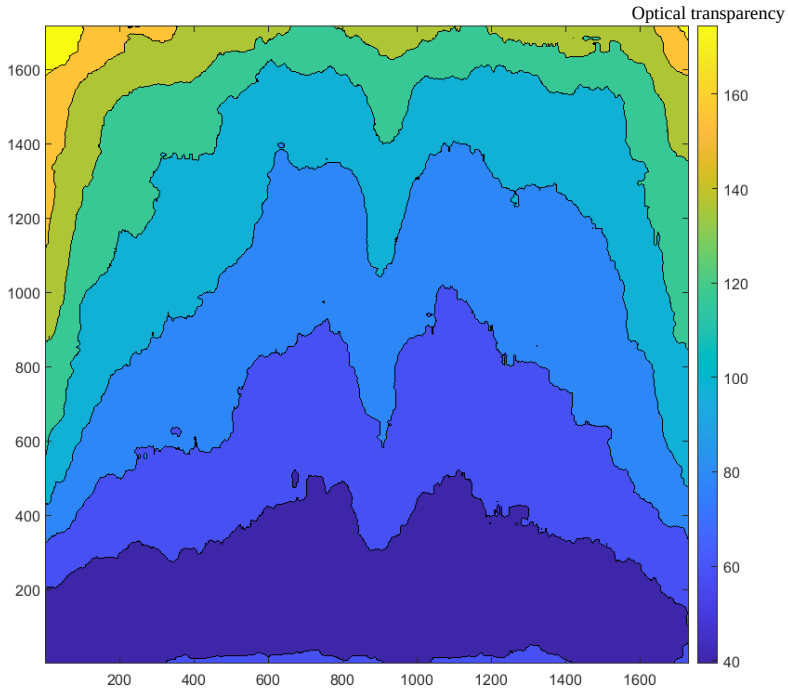

Figure 3.3: Fibre volume fraction distribution in the semi-transparent composite plate

3.3.2 Fibre distribution in the semi-transparent part

The composite plate with short fibres has a non-uniform distribution of fibres. This restricts the regions that can be welded for comparative studies. An experimental procedure is carried out to map the fibre distribution in the composite plates and choose areas on the plate with similar fibre volume fractions.

30 composite plates with a thickness of 2mm and 10% fibre volume fraction are photographed with a digital camera. A white screen with uniform distribution of brightness is placed behind the plate (Figure 3.2). The experimental setup is arranged in darkness to eliminate the influence of external light on the image. The parameters of the digital camera such as exposure time aperture, white balance, ISO and focus are kept constant [106]. The images are captured in grey scale and image processing is carried out on MATLAB.

Figure 3.3 shows the distribution of fibres averaged in 30 composite plates. It can be noted that there is a very low fraction of fibres close to the inlet of the injection mould and there is an accumulation of fibres at the other end. These two regions may not be suitable for welding due to a drastic difference in fibre volume fraction when compared to

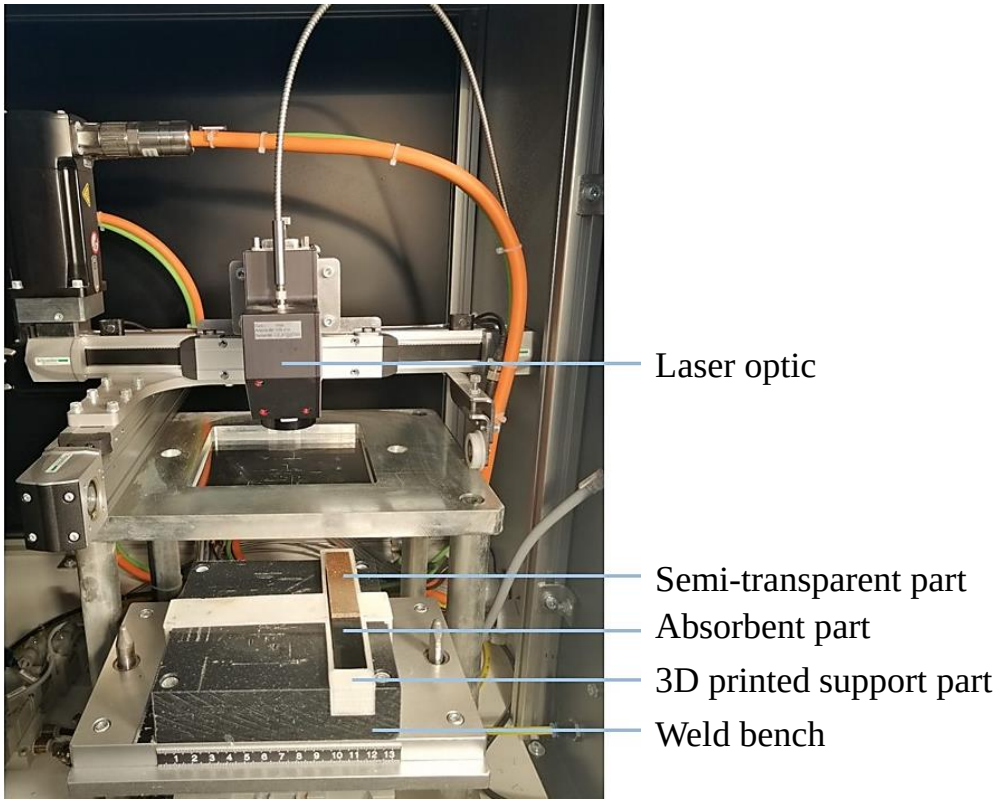

Figure 3.4: Laser welding setup at IMT Nord Europe

the central region on the plate.

3.3.3 Laser transmission welding procedure

The laser welding machine at IMT Nord Europe is equipped with LEISTER NOVOLAS™laser module. The laser optic is equipped with diode laser transported by an optic fibre. The laser wavelength is 940nm. The laser optic is capable of moving in two directions. It is also possible to manually modify the focus of the laser beam.

Clamping system

A simple variant of a fixed clamping system [107] is seen in the welding machine at IMTNE. The materials are placed between a transparent cover and a work bench which is displaced by a pneumatic actuator (Figure 3.5). For welding of high temperature polymers, quartz

glass is used as the transparent cover. Apart from being able to handle load from the clamping pressure, the transparency of the transparent cover is also influential. Figure 3.6 shows that about 95% of laser energy is transmitted through the quartz glass cover between the wavelength range of 300nm and 2000nm. The diode laser used in the current machine is well within this wavelength range.

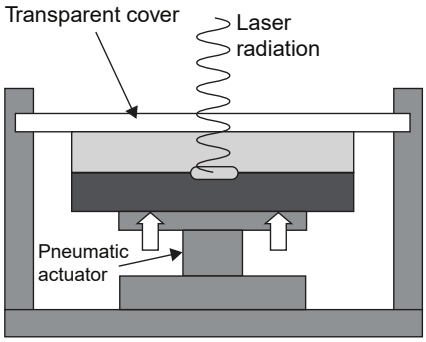

Figure 3.5: Fixed clamping mechanism during LTW process [108, 107]

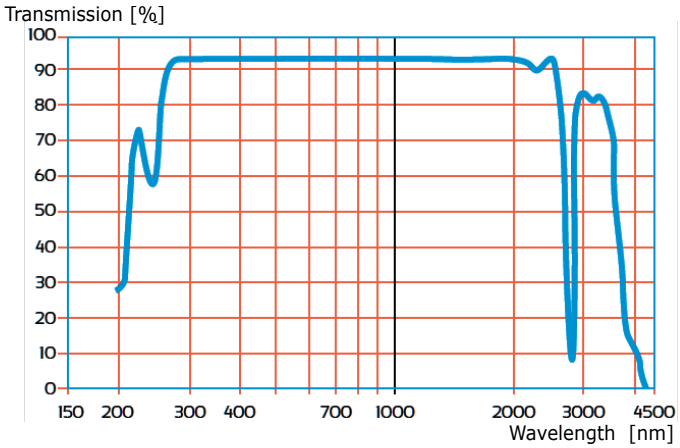

Figure 3.6: Transmission of laser beam through quartz glass with respect to laser wavelength [109].

Support part

During welding process, the weld bench with the specimens moves towards the welding area under the transparent cover. During this displacement, the specimens are at risk of dislocation. A 3D printed support part is designed and manufactured to fit on the weld bench with dimensions based on the specimen size.

Welding procedure

The semi-transparent part is placed above the absorbent part on the weld bench and fixed in a location with the support part. The process parameters are input on a screen of the welding machine. Figure 3.7 shows the options available to insert welding parameters.

Firstly, the screen shows "Laser welding" slide where four icons can be seen. "Coordinates" icon allows to input 2D coordinates of the start and end points of the expected weld line. These values can be found using rulers attached to the weld bench. Additionally, the laser movement speed is input here.

"Parameters" icon leads to options where the laser power is chosen between 0 and 46 W. Other options include laser preheating time, holding time after welding and number of passes of the welding.

The "motor" icon calibrates the position of the laser module before starting the welding process with the icon "start cycle".

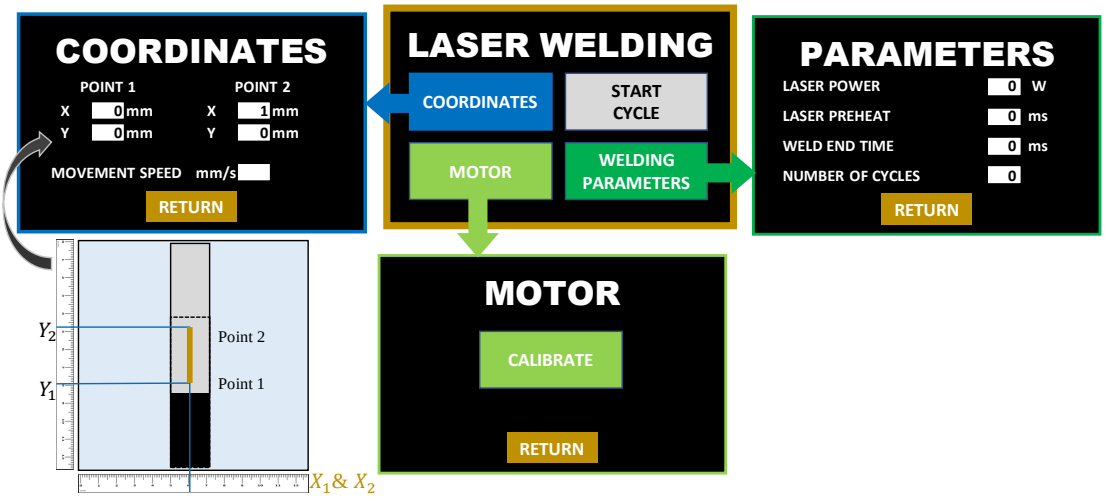

Figure 3.7: Operation of laser welding machine at IMT Nord Europe

3.3.4 Formation of fusion mark

During the welding of a semi-transparent part with a 10% fibre volume fraction, a fusion mark was observed in many cases. The surface fusion mark is caused by the absorption of laser energy at the surface of the semi-transparent part. Weld parameters such as laser speed, power and focus position were iterated to determine the influence of each of these parameters on the formation of the fusion mark. It was concluded that focus position plays a major role in forming the burn mark.

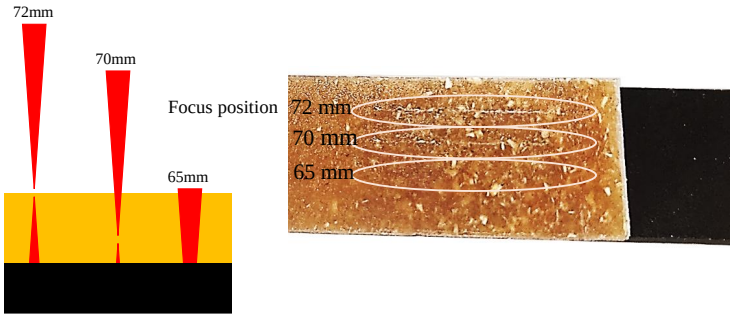

Figure 3.8: Experimental observations of fusion mark occurrence

The focus position is the distance from the laser beam module to the surface of the transparent part. It ranges from 72 mm to 52 mm in the welding machine at IMT Nord Europe. The focal angle is calculated experimentally by measuring the radius of the projected laser beam at every focus position and outlining the triangular structure (2D) formed by all of these projections. The focal angle θ is 8.1712°.

The next step is to find the focus position at which the burn mark is formed and another position at which there is no burning mark. Three focus positions are chosen to weld and the results are seen in Figure 3.8. It is seen that with the farthest focus position, a burn mark is formed at the surface of the semi-transparent part. As a slightly lower length at 70 mm, the burn mark appears to be slightly diminishing non-uniformly along the length of the fusion mark. Finally, when the laser module is at a distance of 65 mm from the material surface, there appears to be no surface fusion mark.

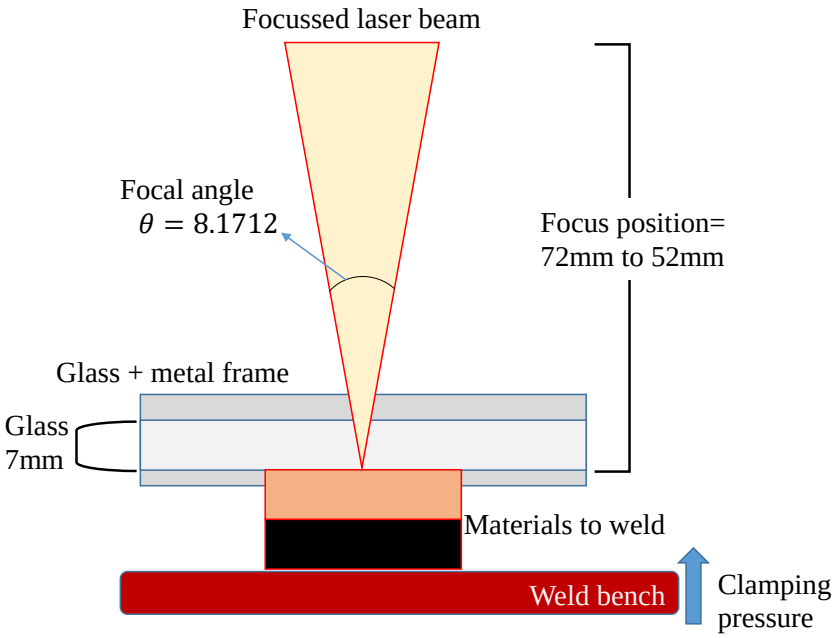

Figure 3.9: Schematic of laser welding machine

3.4 Numerical method

The numerical simulation of energy exiting the semi-transparent part is quantified with the Monte Carlo method which is the basis of the ray tracing method. The two media in the path of the laser rays differ extremely in optical and thermal properties, resulting in scattering and absorption. The intensity distribution of the laser beam within the joining plane is expanded and the laser power usable for the welding process gets reduced [110].

The effect of focus position on the surface absorption of laser radiation is investigated. A 3D numerical geometry is generated that represents the optical and thermal properties of the semi-transparent part. A heat transfer simulation is carried out to determine the temperature distribution in both the semi-transparent and absorbent parts.

3.4.1 3D geometry generation

To model the surface fusion mark, a 3D numerical geometry is constructed in a method similar to the geometry in the previous chapter.

The geometry generation in the case of this simulation is considered with a few constraints. Firstly, the shape of the inclusion is taken as spheres. This is to eliminate the effect of fibre orientation on diffusion, which clearly is influential as seen in the previous chapter. Also, the volume fraction is limited to 10% without any consideration of complete obstruction in the beam path. The only changing variable in the current study is the focus position.

The geometry is repeated multiple times in each direction with the aim to achieve a part thickness of 3mm and a plate size larger than the cross-section area of the laser beam.

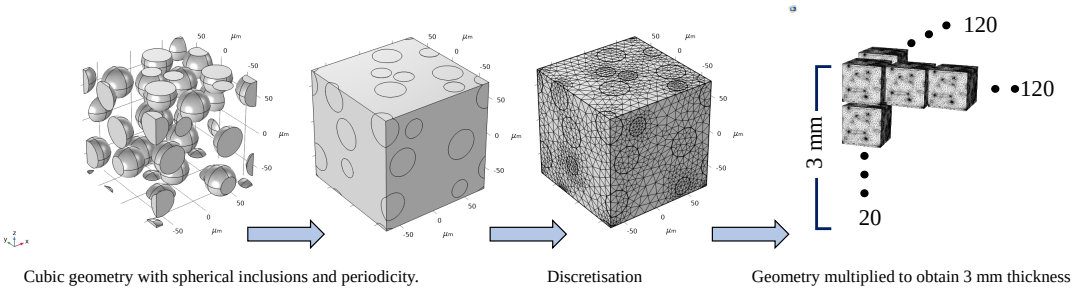

Figure 3.10: Microstructure generation for heat transfer simulations

3.4.2 Homogenisation of semi-transparent part properties

Temperature response in a material involved in high heat fluxes is determined by the thermal properties, namely, thermal conductivity, specific heat and density, which are dependent on temperature. Therefore, the temperature-dependent physical properties of the PLA and flax fibres are used in the present finite element model.

As the heat equation is solved in a transient state, the thermal properties such as material density, thermal conductivity and heat capacity act on the temperature field during welding. The thermal properties of PLA and flax at ambient temperature are provided in the table.

Table 3.1: Thermal properties of PLA and flax fibres at ambient temperature

Thermal properties	PLA	Flax fibers
Melt temperature [°C]	155-170 [111]	-
Thermal conductivity [W/m.K]	0.8 [112]	0.1187
Density [Kg/m^3]	1200 [112]	1540 [113]
Heat capacity [J/Kg.K]	1800 [112]	1000

Heat capacity and density

The specific heat capacity (C_p) at constant pressure describes the amount of heat energy required to produce a unit temperature change in a unit mass. The temperature dependence of the specific heat capacity of PLA is taken into account. The specific heat of flax is assumed to remain constant at all temperatures.

In this work, the heat capacity of the composite material is calculated with the exact rule of mixtures.

$$C_{p,c}(T) = v_f C_{p,f} + v_m C_{p,m}(T) \tag{3.4}$$

where, $C_{p,c}$, $C_{p,f}$ and $C_{p,m}$ are the specific heat capacities of composite, fibres and matrix respectively.

The same procedure is followed for the density of the composite:

$$\rho_c = v_f \rho_f + v_m \rho_m \tag{3.5}$$

where, ρ_c, ρ_f and ρ_m are density of composite, fibres and matrix respectively.

The specific heat capacity of pure PLA as a function of temperature ($C_{p,m}(T)$) is obtained from the material library of an injection moulding simulation software, CADMOULD V14 by SIMCON [114]. $C_{p,c}$ is hence calculated as a function of temperature.

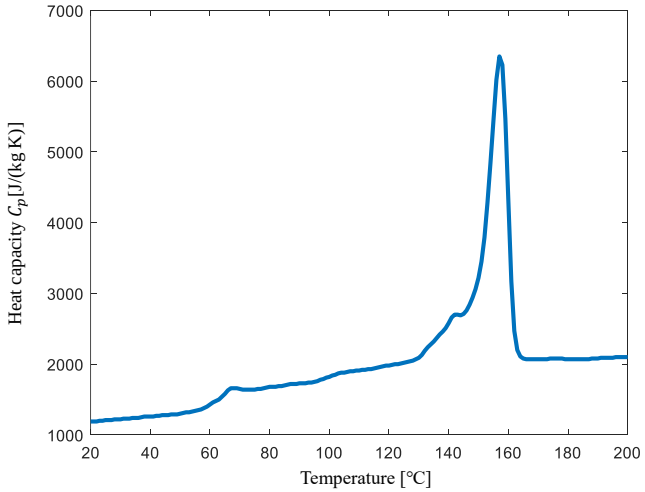

Figure 3.11: Heat capacity of PLA as a function of temperature

Thermal conductivity

For most polymers, the primary mechanism of heat conduction is through phonons [115] The two basic models representing the upper bound and the lower bound for thermal conductivity of composites (k_c) are the rule of mixture (parallel model) and the series model, respectively [116]. In the parallel model, each phase is assumed to contribute independently to the overall conductivity, proportionally to its volume fraction:

$$k_c = v_f k_f + v_m k_m \tag{3.6}$$

On the other hand, the series model assumes no contact between particles and thus the contribution of fibres is confined to the region of the matrix embedding the particle. The conductivity of fibre composites according to the series model is predicted as

$$k_c = \frac{1}{(v_m/k_m) + (v_f/k_f)} \tag{3.7}$$

The thermal conductivity (k) describes the relationship between the heat flux vector (q) and the temperature gradient (∇T) with Fourier's law of heat conduction.

$$q = -k\nabla T \tag{3.8}$$

Thermal conductivity is influenced by fibre distribution (clusters, dispersed individual inclusions), anisotropy (for non-spherical fibre inclusions), properties of fibre–matrix interfaces, and effects of manufacturing process history [117].

The thermal conductivity of natural fibre composites is greatly influenced by their morphological structure and chemical composition [118]. The arrangement of these fibres affects the thermal conductivity of the composite material.

Equation 3.8 is used to calculate the effective thermal conductivity of the composite material in use. A numerical simulation [88] is conducted on COMSOL Multiphysics, starting by generating a temperature gradient by imposing periodic Dirichlet boundary conditions on the numerical composite geometry.

The determination of a fixed component k_i implies the application of temperature on the faces of the numerical geometry, to create a constant periodic thermal gradient ∇T_i value and direction i. The k_i value is then calculated with Equation 3.9 that illustrates the case of the calculation of k_x for $i = x$:

$$k_x = \frac{\iiint_V q_x dv}{\iiint_V \nabla T_x dv} \tag{3.9}$$

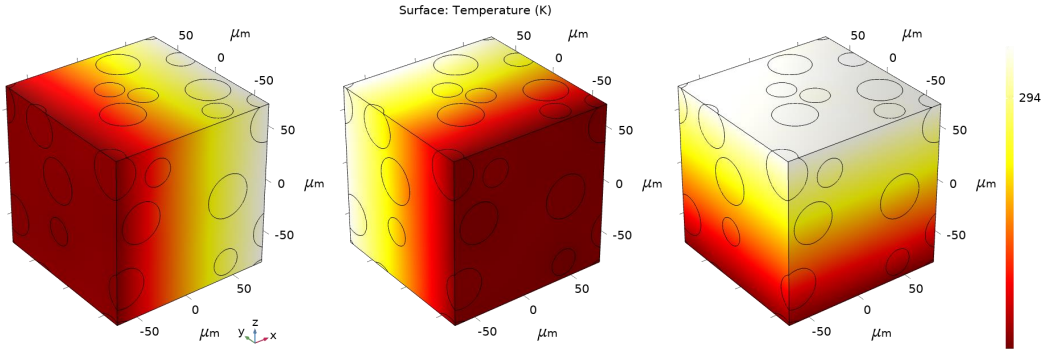

Figure 3.12: Homogenisation of thermal conductivity compostie materials with numerical simualtions.

However, in the current geometry, the spherical shape of the fibre inclusions has influenced the geometry equally in all directions. The effective thermal conductivity (k_{eff}) in the directions x, y and z is calculated to be 0.18 W/m.K.

Absorption coefficient

The homogenised absorption coefficient (K_h) of the semi-transparent part is calculated with the distance travelled by each ray individually in the two media (fibre and matrix) and the absorption coefficients of each medium.

$$K_h = \frac{l_m}{l_m + l_f} K_m + \frac{l_f}{l_m + l_f} K_f \tag{3.10}$$

Hence the distance travelled by a ray in the matrix volume (l_m) and fibre volume (l_f) should be calculated at a micro-scale during ray-tracing simulations (Eq. 3.10).

For the high number of rays projected into the heterogeneous geometry with numerous fibre-matrix interactions, the calculations of distance travelled by all the rays consume high computation costs. Cosson et al. [64] observed that the ratio of the average distance travelled by a laser ray in the fibre to the total average distance can be equated to the fibre volume fraction. Hence, $\frac{l_f}{l_f + l_m} = v_f$. Similarly, this can be applied to the distance travelled in the matrix. This facilitates Eq. 3.10 to be

$$K_h = v_m K_m + v_f K_f \tag{3.11}$$

In the case of this work, the fibre volume fraction is 10%. The absorption coefficient of PLA and flax fibre is 80 1/m and 100 1/m respectively. Hence the calculated absorption coefficient is 84 1/m.

3.4.3 Temperature measurement at the interface

The thermal history of the welding process at the interface is monitored using a thermocouple [119]. The temperature is measured with a custom-made programmable thermocouple with a Raspberry Pi miniature computer. The initial temperature is calibrated with an infrared thermometer.

The temperature sensor is placed at the weld interface at the expected centre of the weld line. A python-based algorithm is used to record the temperature during welding. Two cases of welding are done, one with pure PLA plate as transparent part and the second with PLA plate containing 10% short flax fibres. The plates have a thickness of

3 mm. The laser speed is set to 1 mm/s and the focus position is set to 70mm. The welding is carried out in two cycles with a delay of 2 seconds between the cycles. Figure 3.13 shows the temperature profile at the centre point of the weld line for the two cases. In the case of pure PLA, the maximum recorded temperature is approximately 200°C, whereas for the semi-transparent composite it is 170°C. These tests are further performed in the next chapter.

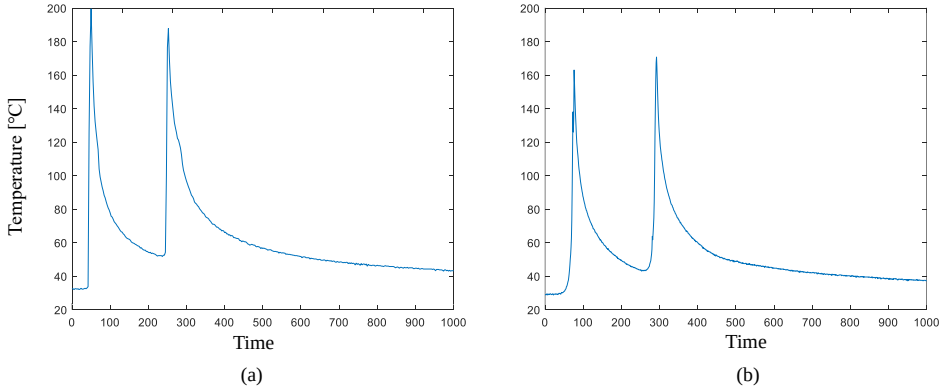

Figure 3.13: Weld interface temperature for (a) Pure PLA and (b) PLA with 10% short flax fibres.

3.4.4 Modified Ray tracing simulation

Now, the numerical geometry is ready for ray tracing simulation. The ray tracing simulations are carried with a focused beam having a focal angle as seen in the welding machine. The beam is discretized into 200000 rays. Figure 3.14 shows an example of the ray direction at focus positions 72 mm and 70 mm when there is no obstruction in the path. All the remaining parameters are the same as seen in the previous chapter.

To calculate the absorption coefficient in the semi-transparent part, modifications are made to the ray tracing algorithm. Figure 3.15 is a schematic of the path of a ray that is travelling through the thickness of the semi-transparent part. The distance travelled by each ray in every macro-element is calculated during ray tracing simulation (d in Equation 3.2). For each macro-element, the Beer-Lambert theory is applied to calculate the attenuation of the laser intensity of every ray when it propagates through each macro-

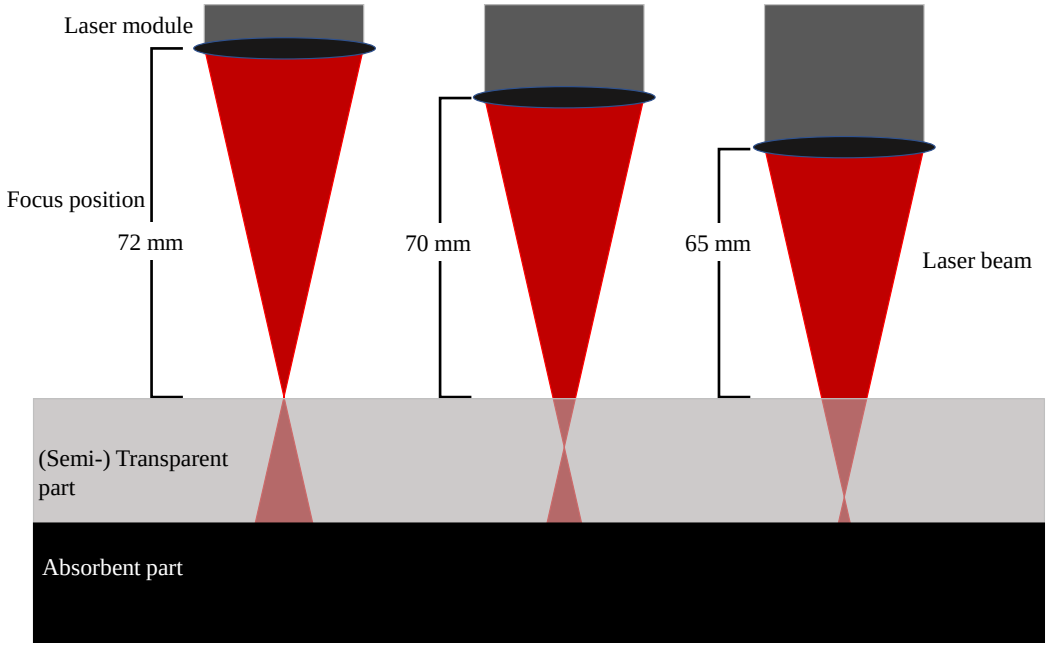

Figure 3.14: Position of laser beam at various focus positions.

element.

As a ray is followed in the heterogeneous media which is the semi-transparent part, multiple reflections and refractions are seen at a microscopic scale as pertained by Snell-Descartes law. This phenomenon alludes to light scattering or diffusion at the macroscale. Coupling Snell-Descartes law and Beer-lambert law to compute the source term in ray tracing simulation.

When Beer-Lambert equation is applied to a macro-element n, the intensity of a ray after travelling through the macro-element can be written as,

$$I_n = I_{n-1} e^{-K_h d_n} \tag{3.12}$$

The difference in intensity in every macro-element is given by

$$I_{a,n} = I_{n-1} - I_n \tag{3.13}$$

This is the energy absorbed in the macro-element, n.

Two profiles are created with the ray tracing simulation. A 2D plot of the weld

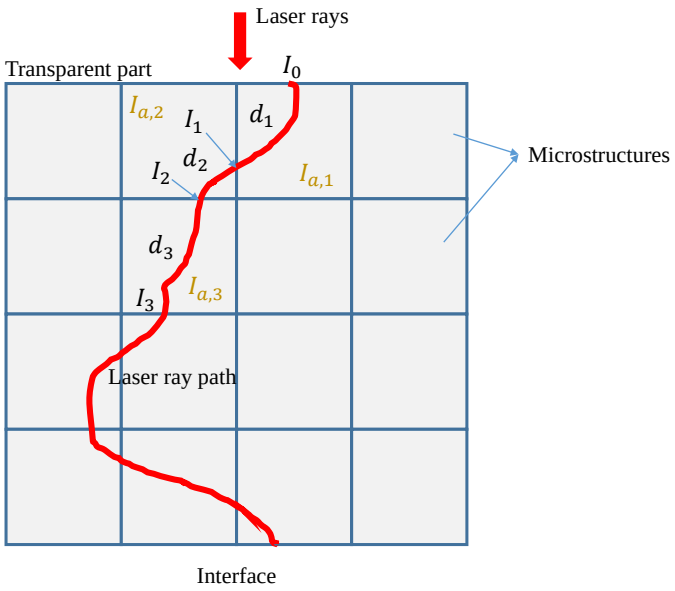

Figure 3.15: Absorption of laser energy in semi-transparent part

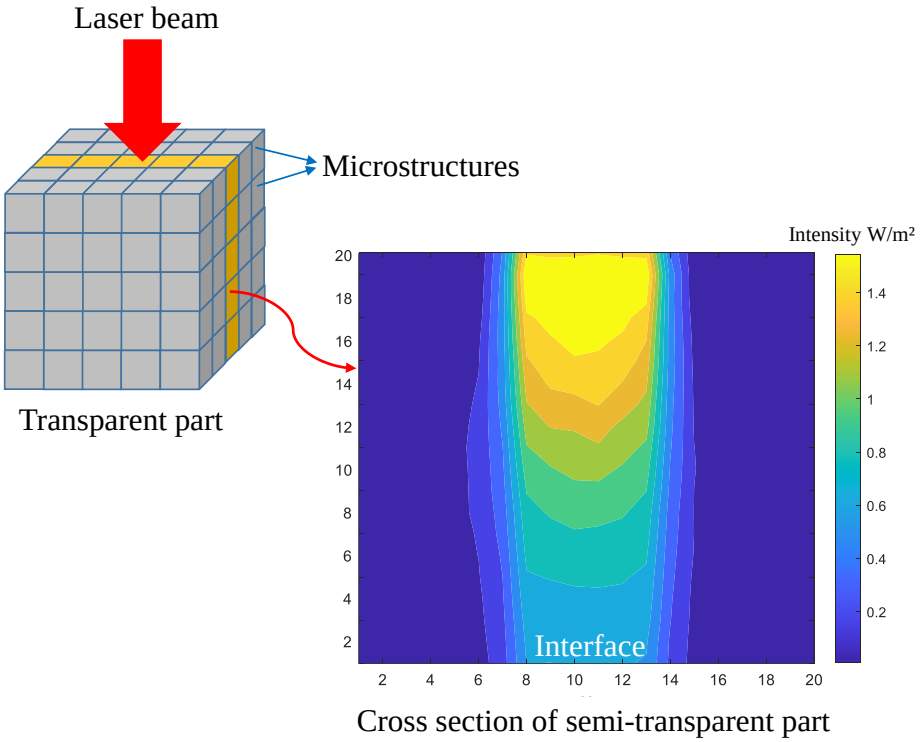

Figure 3.16: Contour plot of the laser intensity in all microstructures at the cross-section.

interface with a map of intensity and a 3D profile (Figure 3.16) of the energy absorbed in the semi-transparent part. These two profiles are the input parameters for performing heat transfer simulations.

3.4.5 Heat transfer simulations on COMSOL Multiphysics

COMSOL Multiphysics is a finite element solver for multiphysics simulations. This software is used to model heat transfer during laser transmission welding in this work. The heat transfer in the interface of the solid in COMSOL is used to model heat transfer in solids by conduction, convection, and radiation. The interface solves the heat equation with a time-dependent study [120]. In this work, laser transmission welding is modelled by solving the heat equation and determining the temperature evolution in the weld zone at the interface.

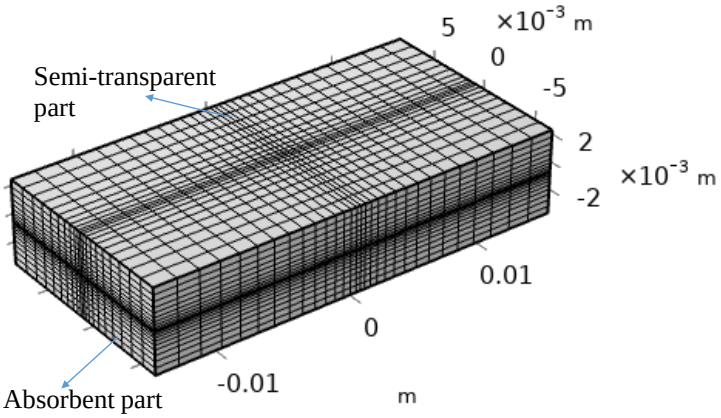

Figure 3.17: FEM mesh used in COMSOL for thermal simulation.

A component geometry representing the semi-transparent part and the absorbent part is constructed on COMSOL. The thickness of the two parts is 3 mm. The parts are 30 mm long and 15 mm wide. A hexahedral mesh (Figure 3.17) is generated with additional fineness in the weld zone. The material properties are user-defined, hence, the homogenised values of C_p, ρ and k_{eff} are input for semi-transparent material properties. The thermal

properties of the absorbent part are that of pure PLA, as seen in Table 3.1.

The initial value for temperature is taken as the default room temperature, 20°C. Thermal insulation is applied on all the faces of the components except the interface. The heat source input for the semi-transparent component is the intensity profiles generated using ray tracing simulations. The intensity distribution data is applied as a function depending on the volume of the semi-transparent part and the area of the weld interface. This is done using Matlab live link linked to COMSOL. The simulation is carried out with a moving heat source across the length of the geometry components at an input speed. Thus, a time-dependent study is computed.

3.5 Results

Surface fusion marks as observed in the experimental study were simulated. Figure 3.18 shows the temperature distribution at the cross-section of the two components. Temperature above the melt temperature of PLA is seen at the surface of the semi-transparent part in the first two cases. At a focus position of 72 mm, there seems to be a high probability of material degradation. This was also observed in some experiments.

Though at lower lengths the burn mark can be completely omitted, it is to be noted that the width of the weld line at the material interface is deeply affected by the focus position. Figure 3.19 compares weld lines formed at high and low focus positions. With a high focus position, a high portion of the laser energy is absorbed at the surface, resulting in a surface burn mark and the meaning energy contributed to the interface weld line. However, at low lengths, the laser energy has not been absorbed at the surface of the semi-transparent part but is widely distributed at the weld interface. The line is wider and there seem to be only a few regions where the polymer melted to cause interface interdiffusion. The temperature distribution seems to be non-uniform in both cases.

3.6 Conclusion

Absorption of laser energy in a semi-transparent part was modelled in this chapter. During welding of flax fibre reinforced PLA composites of 3mm thickness, a surface burn mark

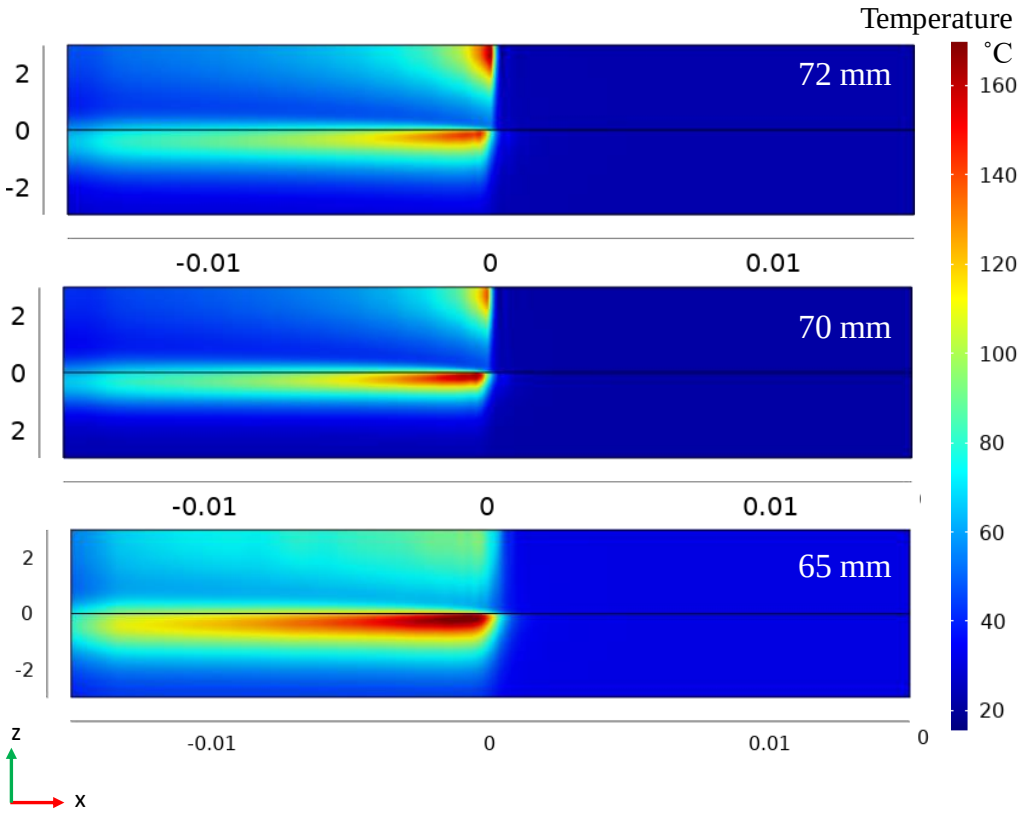

Figure 3.18: Comparison of temperature field in three cases of focus position.

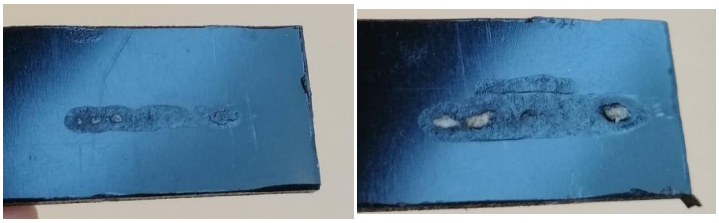

Comparative focal length:	High	Low
Burn mark on transparent part surface:	Yes	No

Figure 3.19: Effect of focus position on weld line at weld interface

was observed. The temperature field at melted regions at both interface and surface of semi-transparent part was simulated numerically.

Among all the weld parameters, focus position seemed to have high impact on formation of the burn mark. Hence this chapter focused on optimising the focus position suitable for maximum energy transmission to the weld interface. A thermal model was followed to simulate the absorption phenomenon by solving the 3D transient heat equation. As the semi-transparent part is heterogeneous, thermal and optical properties were homogenised numerically. Temperature field in the assembly was determined with experimental methods.

Chapter 4

Study of molecular interdiffusion in a polymer-polymer weld line: Optimisation of laser welding process

Conductive heat transfer between the thermoplastic parts plays a vital role in defining the assembly quality during laser transmission welding. During this step, within the heat affected zone (HAZ), entanglement of polymer chains can be noticed leading to the formation of interfacial bond aka weld. The weld strength can be expressed a function of developed temperature field (T), clamping pressure (p) and processing time (t) (see Figure 4.1).

$$\sigma = f(T, p, t) \tag{4.1}$$

The formation of a weld between the two parts involves two stages:

- The development of intimate contact between the semi-transparent part and the absorbent part.
- Interdiffusion of molecular chains across the interface.

Interdiffusion can only occur after the intimate contact has been established. The optimum quality of the weld line obtained at the interface of the two parts can be justified by

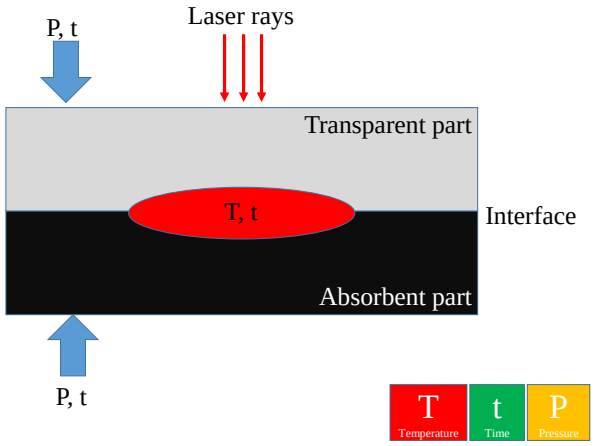

Figure 4.1: Inflience of physical parameters on weld line formation during laser transmission welding

developed mechanical strength, which is a function of the thermal history at the interface of the two parts [121].

The objective of this chapter is to investigate the interfacial interactions between the polymer chains at macromolecular level and linking them to the evolution of temperature in HAZ. Firstly, existing models based on isothermal and non-isothermal molecular interdiffusion are presented and their advantages are discussed. A quasi non-isothermal model is presented to predict the weld strength formation based on weld parameters. The model is approached with temperature field information calculated through numerical heat transfer simulations and measured through experimental procedures. The predicted weld strength is validated with mechanical tests.

4.1 Degree of bonding

The quality of the bond formed by a weld line is determined by the degree of bonding (D_b), which is calculated by considering two stages of the welding process and can be expressed as:

$$D_b = D_{ic} \times D_{au} \tag{4.2}$$

where, D_{ic} is the degree of intimate contact and D_{au} is the degree of autohesion (also known as degree of healing D_h). Bonding is assumed to be perfect when D_b becomes unity [21] and occurs only in the areas of weld interface that are in intimate contact [122]. The development of intimate contact is a function of the applied clamping pressure and time, where as healing is a function of temperature history and time. Though the time required to attain an intimate contact is much shorter than the time of autohesion, it impacts greatly on the degree of bonding [123].

4.2 Intimate contact model

At the beginning of the LTW process, the surfaces of the two parts at the interface are not perfectly smooth due to surface roughness. Hence, flattening of these surface asperities is necessary to allow a good interdiffusion at the molten weld interface. The time required to achieve an intimate contact at the weld interface is proportional to the irregularity on the interface surfaces [124].

The degree of intimate contact (D_{ic}) is a function of the physical parameters such as time and applied pressure. The time needed to achieve an intimate contact between the two materials is calculated by applying clamping pressure on the materials until D_{ic} reaches 1 [125] .

The intimate contact model was initially proposed to describe the contact between plies, however, the model can be interpolated to LTW process [119]. Surface roughness can be represented as a plane consisting of a series of rectangles which are uniformly or randomly distributed. Dara and Loos [126] represented these rectangles with statistical distribution having different heights and widths. However, Lee and Springer [122] simplified the approach with identical rectangles. The applied pressure on the rectangular irregularities spreads them along the interface causing an intimate contact (figure 4.2). The model was incorporated into a healing model by Butler et al. [48]. Yang and Pitchumani [127] developed a model in which surface roughness can be described in more detail using a cantor set fractal ensemble, where each geometric parameter can be obtained from a surface profile measurement. In general, these models show that the time required to reach full intimate contact, t_{ic} is proportional to the viscosity of the fibre-matrix mixture,

μ_{mf} and inversely proportional to the applied pressure P_{app} [128]:

$$t_{ic} \propto \frac{\mu_{mf}}{P_{app}} \tag{4.3}$$

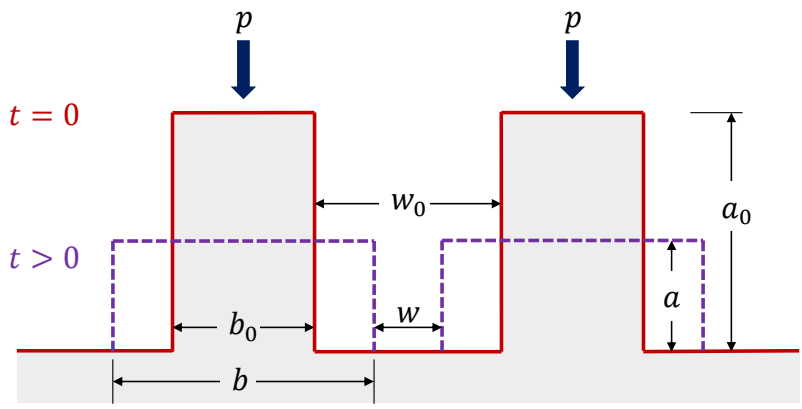

Figure 4.2: Rectangular elements representing surface roughness before and after applying clamping pressure.

The initial identical rectangles (at time $t = 0$) that represent the surface roughness have a height of a_0, width b_0 and are separated with a distance of w_0. The approach uses volume conservation equation (equation 4.4) to express the evolution of the rectangles in order to achieve an intimate contact upon applying clamping pressure [124].

$$V_0 = a_0 b_0 = ab \tag{4.4}$$

The final dimensions of the rectangles is aimed to be of height a and width b so as to eliminate the variable w_0 . The degree of intimate contact is defined using the dimensions in Figure 4.2 as

$$D_{ic} = \frac{b}{w_0 + b_0} \tag{4.5}$$

Equations 4.4 and 4.5are combined to define degree of intimate contact by eliminating the distance between the rectangles, w_0.

$$D_{ic} = \frac{\frac{a_0}{a}}{1 + \frac{w_0}{b_0}} \tag{4.6}$$

Further, the mass flow is considered laminar taking into account the viscosity of the fibre-matrix mixture, followed by applying mass conservation law to control the volume and as a function of the applied pressure [129].

In case of an isothermal and constant application of clamping pressure during the process, D_{ic} can be written as

$$\frac{\partial D_{ic}}{\partial t} = 2^{\frac{n+1}{n}} \frac{n(n+2)^{\frac{1}{n}}}{2n+1} \left[\frac{A}{(b_0+w_0)^2}\right]^{\frac{n+1}{n}} \left[\frac{P_{app}}{\mu_{mf}}\right]^{\frac{1}{n}} D_{ic}^{\frac{-n-3}{n}} \tag{4.7}$$

$$D_{ic}(t) = \left[D_{ic}^{\frac{2n+3}{n}}(0) + C\left[\frac{P_{app}}{\mu_{mf}}\right]^{\frac{1}{n}} t\right]^{\frac{n}{2n+3}}, C = 2^{\frac{2n+1}{n}} \frac{(2n+3)(n+2)^{\frac{1}{n}}}{2n+1} \left[\frac{A}{(b_0+w_0)^2}\right]^{\frac{n+1}{n}}$$

where, n is the power law index.

The approach can only be simplified by assuming the material to be Newtonian, resulting $n = 1$. The degree of intimate contact is now,

$$D_{ic} = \frac{1}{1+\frac{w_0}{b_0}} \left[1 + \frac{5P_{app}}{\mu_{mf}} \left(1+\frac{w_0}{b_0}\right) \left(\frac{a_0}{b_0}\right)^2 t\right]^{\frac{1}{5}} \tag{4.8}$$

A complete contact at the weld interface is achieved when the two materials are clamped together with pressure P_{app} for a time t to achieve $D_{ic} = 1$. The time required to reach a full contact is,

$$t_{ic} = \frac{\mu_{mf}}{5P_{app}} \frac{1}{1+\frac{w_0}{b_0}} \left(\frac{b_0}{a_0}\right)^2 \left[\left(1+\frac{w_0}{b_0}\right)^5 - 1\right] \tag{4.9}$$

4.3 Interdiffusion at the weld interface

Once an intimate contact is observed at the weld interface, the setup is eligible to underego the bonding process namely, autohesion or healing. Figure 4.3 (c) shows that the region c experiences healing with the migration of molecular chains at time t_{ic}. Hence, the degree of healing can be expressed as

$$D_h = \frac{c}{b} \tag{4.10}$$

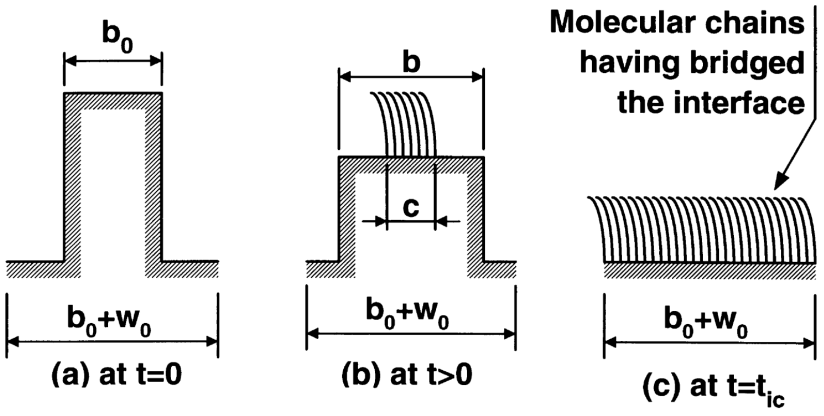

Figure 4.3: Representation of molecular chain diffusion in region c after compression of unit cell b to achieve an intimate contact [130]

where c is the width of the area where molecular chain movement can be observed and b is the width of the unit cell.

Interdiffusion process at the interface is influenced by the part geometry, material thermal properties and welding process parameters [131]. When the laser beam energy melts the two thermoplastic composites locally, allowing polymer chains to diffuse from their original positions. Hence, the chains have an opportunity to interdiffuse within the molten region for a time (t_m) However, the interdiffusion across the melt fronts is not immediate. The polymer chains diffuse gradually beyond the interface, following a series of disentanglements and entanglements. If the chain entanglement is the same as before the melting, the original material strength is attained [132].

Initially, the diffusion mechanism between small molecules was well understood by the Fickian law and the diffusion of the small molecules in the polymer network was explained by a modified Fick's law that included additional stresses due to the penetration of the involved solvents. In cases of highly entangled chains, which is commonly seen in polymers [133], the diffusion mechanism becomes more complicated.

The examination of highly entangled and thermally influenced interactions of polymer chains is based on the chain dynamical theory known as reptation theory and is hypothesized by deGennes [134]. An advanced reptation theory described by Wool et al. [21] is generally accepted to describe the diffusion process of polymer chains. The premise of reptation theory is that the polymer chain is confined to an imaginary tube (reptation

tube) which represents the surrounding entanglements of the other polymer chains. Entanglements resist polymer chains from each others movement. The model assumes that the polymer chains can move freely within the tube but can leave the tube along the curvilinear axis of the tube only. However, the reptation model does not consider realistic welding processes where the temperature at the weld line drastically rises in time. Since the model studies in detail the behaviour of the polymer chains, a steady, low healing temperature at the interface has to be assumed [135]. Figure 4.4 summarises the procedure of interdiffusion with respect to time.

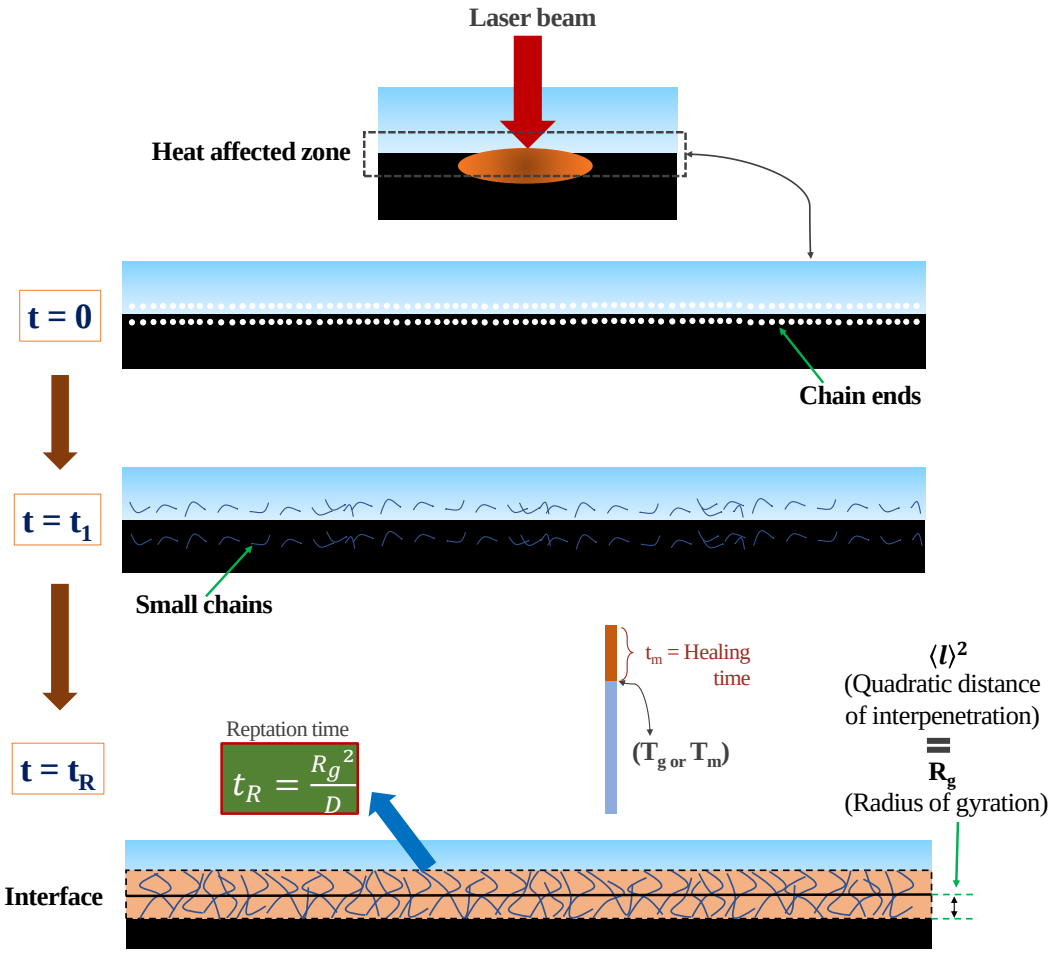

Figure 4.4: Stages of interdiffusion of polymer chains during laser transmission welding

Figure 4.5 shows the timeline of polymer chain exiting the reptation tube where the

polymer chains require reptation time (t_R) to completely displace from the original tube. Reptation time is expressed as

$$t_R = \frac{R_g^2}{D} \tag{4.11}$$

where, R_g is the radius of gyration and D is the interdiffusion coefficient.

According to the reptation theory, several characteristic time regimes can be delimited considering the general motion behavior of the polymer chains. At short times known as the Rouse relaxation time between entanglements ($t < t_e$), a small motion takes place on statistical segment without being subjected to topological constraints. Later, for $t_e < t < t_r$, which is the Rouse relaxation time for the whole chain, the chain is influenced by the topological constraints of the tube and the motion is observed. For time $t_r < t < t_R$, which is the reptation relaxation time, the defects are equilibrated along the total length of the tube and the polymer chain diffuses as whole along the fixed tube. Lastly, for $t > t_R$, the chain motion is governed by reptational dynamics that allow the chain to renew the tube by escaping completely from the first tube without memory of its initial conformation.

Reptation of the polymer chains also takes place across the weld lines and hence contributes to the healing of weld lines [136]. Improper interdiffusion of molecular chains across the interface leads to decrease of weld strength formation [137]. The effectiveness of interdiffusion of polymer chains is determined be the average interpenetration distance of the chains across the interface. At reptation time t_R, the polymer chains interpenetrate to mean square end-to-end distance of the polymer chain. The squared radius of gyration is expressed in place of the mean square end-to-end distance of the polymer chain as it facilitates to be measured experimentally. Hence, the chains should travel an average distance equal to the radius of gyration [119]. The square radius of gyration (R_g^2) is the average squared distance of any point in the polymer chain from it's center of mass, also known as the moment of inertia.

Since the healing time can only be determined experimentally, the reptation time can be used to obtain a prediction of the interfacial mechanical strength. The welding time and the reptation time strongly depend on the temperature field in the weld zone: higher temperatures give greater mobility of the polymer chain and therefore promote healing

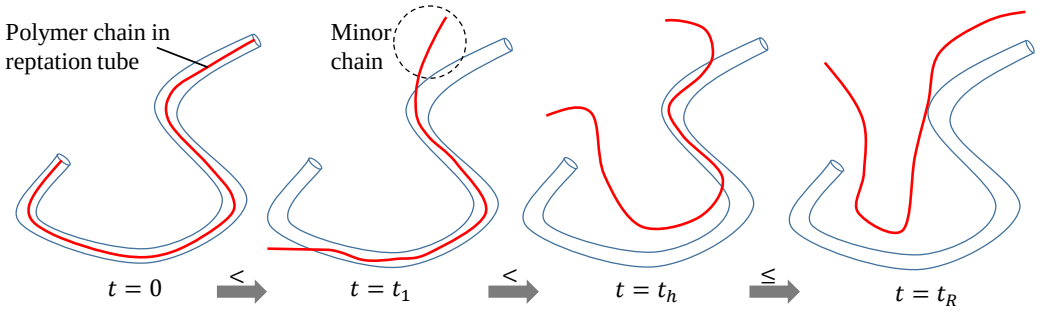

Figure 4.5: Diffusion of molecular chains according to Reptation theory.

at the interface. Under isothermal conditions, the bond strength is given by degree of healing as the ratio of strength of the weld line (σ_w) to the ultimate strength of the material (σ_{max}) [132]:

$$D_h = \frac{\sigma_w}{\sigma_{max}} \tag{4.12}$$

Studies [54, 137] have shown that the degree of healing is proportional to the fourth root of time available for weld line to heal in the molten region. Hence,

$$\frac{\sigma_w}{\sigma_{max}} \propto t^{\frac{1}{4}} \tag{4.13}$$

This allows to relate weld line strength to reptation time as follows,

$$\frac{\sigma_w}{\sigma_{max}} = \left(\frac{t}{t_R}\right)^{\frac{1}{4}} \tag{4.14}$$

At time t_R, the polymer chains reorganise to erase the interface and weld strength is equal to that of a pure material [135]. Reptation theory hence shows that the weld strength development depends on keeping the weld interface equal to or above the melt temperature (T_m) for a time equal to or above t_R.

According to Wool et. al [21], equation 4.12 is valid only for low molecular weights M within the range defined using the critical entanglement molecular weight M_c: $M_c < M < 8M_c$. At high molecular weights, the distance of interpenetration does not have to reach radius of gyration R_g. Maximum bond strength can be achieved at a time t_h (healing time) instead of t_R. Healing time (t_h) is see in Figure 4.5 (c) where, $t_h \leq t_R$.

Typically, engineering thermoplastics have higher molecular weights [22]. Hence, a

maximum bond strength can be achieved at a healing time.

4.4 Interdiffusion under non-isothermal conditions

Based on reptation dynamics, the temperature dependence of movement of polymer chains and the temperature history of the weld interface, the degree of healing can be evaluated as

$$D_h = \left[\int_0^t \frac{1}{t_h(T(t))} dt\right]^{\frac{1}{4}} \tag{4.15}$$

The determination of the degree of healing requires the history of the temperatures at the interface and the healing time of the polymer as a function of temperature. Note that the healing time can be considered equal to the relaxation time [138], which can be deduced from measurements of viscosity as a function of the shear rate. The reciprocal of the transition point from the Newtonian plateau to the shear thinning region is the relaxation time which is then used as the healing time for that specific temperature. After determining the healing time for different temperatures, an Arrhenius law can be used to describe the temperature dependence [130].

$$t_R = B_R \exp\left(\frac{A_R}{T}\right) \tag{4.16}$$

where, A_R and B_R are parameters to be determined experimentally.

Kim and Suh [137] defined an approach to calculate weld line strength based on molecular interdiffusion. Here, the weld line factor is represented as a function of the the total interface area in the weld line A_0 and the area where interdiffusion has not yet taken place A.

$$\frac{\sigma_w}{\sigma_{max}} = 1 - \frac{A}{A_0} \tag{4.17}$$

The change in area (A) where interdiffusion has not taken place is determined by the diffusion coefficient. According to Doi et al. [139], the coefficient of diffusion D is a function of plateau modulus G_N^0 [140], polymer density, ideal gas constant, temperature T, mean square end-to-end distance R_g^2, mean molecular weight M_W, critical entanglement molecular weight M_c, and zero viscosity. This model determines the coefficient of diffusion

as a function of density, temperature, and zero viscosity.

$$D = \frac{G_N^0}{135}\left(\frac{\rho RT}{G_N^0}\right)^2\left(\frac{R_g^2}{M_W}\right)^2\frac{M_c(T)}{M_W^2\mu_{0,M(T)}} \tag{4.18}$$

Diffusion being temperature dependent, as healing temperature increases, the time required to achieve ultimate weld strength decreases.

An equivalent diffusion coefficient ($\bar{D}$) along a weld line is written by a time averaged diffusion coefficient for the welding process.

$$\bar{D} = \frac{1}{t_{m,max}}\int_0^{t_{m,max}} D(t_m, T)\, dt_m \tag{4.19}$$

Ezekoye et al. [135] noted that if the developed weld strength is plotted along side interpenetration distance (l), the average diffusion distance in all the cases would collapse to the same line and the ultimate strength would be achieved when l is equal to R_g. While reptation theory considers that polymer chains to describe weld strength formation, it is suitable to correlate welding parameters such as laser power and speed to bond strength formation.

$\bar{D}$ is used to calculate equivalent reptation time with equation 4.11. The degree of healing at a time $t_{m,max}$ is written as,

$$D_h = \left(\frac{t_{m,max}}{\bar{t_R}}\right)^{\frac{1}{4}} = \left(\frac{t_{m,max}\bar{D}}{R_g^2}\right)^{\frac{1}{4}} = \frac{\sqrt{l}}{1.1892\sqrt{R_g}} \tag{4.20}$$

The degree of healing may also be defined by the length of the minor polymer chain (l_m) and the full length of the chain (L) (refer Figure 4.5).

$$D_h = \frac{\sigma_w}{\sigma_{max}} = \left(\frac{l_m}{L}\right)^{1/2} \tag{4.21}$$

This equation is obtained by assuming that the factor of proportionality of the strength with the square root of the minor chain length, l_m, is the same for σ and σ_{max}. Note that Equation 4.21 applies to isothermal and nonisothermal conditions alike. However, the growth of the minor chain length with time depends on the temperature history.

The temperature dependent reptation time t_R can be calculated using the entangle-

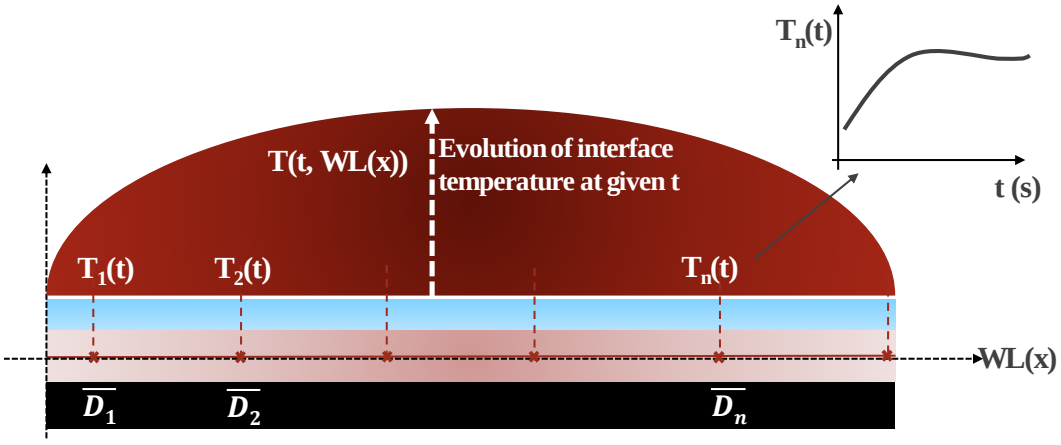

Figure 4.6: Coefficient of interdiffusion at the weld interface as a function of temperature.

ment molar mass M_W, the density ρ, the zero viscosity μ_0, the ideal gas constant R, and the temperature of the polymer Using the reptation model, temperature dependent t_R can be determined as

$$t_R(T) = \frac{20M_c}{\pi^2 RT\rho}\mu_0 \tag{4.22}$$

Observations of reptation theory

1. Reptation theory describes the formation of weld strength by examining the quadratic distance of inter-diffusion ($\langle l \rangle$) of polymer chains across the weld interface.

2. During reptation, $\langle l \rangle^2 = R_g$ [141] and weld strength (σ) = strength of pure material (σ_m).

3. The development of weld strength depends on maintaining the interface temperature above melt temperature (T_m) for a time $t \geq t_R$.

4. Maintaining melt temperature at interface for a time (t) longer than t_R is unnecessary as this will not result in additional strength formation.

It should be noted that the models mentioned earlier in this chapter were developed for amorphous polymers. It has been identified by Akkerman et al. [142] that, in literature, there appears to be no consensus on how to model the healing process of semi-crystalline

polymers. The non-isothermal healing model developed by Yang and Pitchumani [127] only applies for amorphous polymers and is, therefore, only applicable for semi-crystalline polymers in a melted state and can continue until the polymer starts to crystallize. Nevertheless, in some studies the healing model for amorphous polymers was directly applied for semi-crystalline polymers without considering the effect of the crystalline structure above the glass transition temperature [130, 143]. It is safe to assume that healing of semi-crystalline polymers can occur only above the melting temperature [122, 22].

4.5 Proposed model to predict the weld strength

To calculate the weld strength in non-isothermal conditions, Equation 4.15 must be validated. For this, values of $t_h(T)$ is needed. Measurement of healing time with accuracy is not possible, especially considering the weld interface is not accessible without interrupting the intimate contact between the two materials. Hence, separate experiments are conducted to measure interface temperature and degree of healing with respect to welding speed.

As laser translation speed impacts the weld temperature, many samples are welded at different weld speeds. To measure the degree of healing, Equation 4.21 is evaluated with tensile tests performed on lap jointed specimens. Laser transmission welding of pure PLA plates, one transparent and the other absorbent to laser is performed at constant weld power. Mechanical test is performed on these samples to determine the shear stress at the weld line. The ultimate strength of the material σ_{max} is assumed to be the maximum weld strength result obtained in the tensile tests [22].

Secondly, more pure PLA plates are welded at the laser speeds input in the previous case. This time, the temperature at the heat affected zone is measured using thermocouple. The approach to this experiment is mentioned in the precious chapter.

These tests are gathered to correlate laser welding speed, temperature evolution at HAZ and weld strength developed at these conditions. D_h exhibits a linear relationship with $t^{\frac{1}{4}}$ according equation 4.20 which is in isothermal reptation conditions. This is taken to the advantage to measure D_h with respect to t_m. For each case of welding speed, the degree of healing is plotted against the time that the polymer stayed in a melted form,

in this case, $t_m^{1/4}$. At time $t = 0$, $D_h = 0$ which is at the start of the process. A straight solid line passing through the origin and the formerly plotted point can be drawn because it denotes a best linear regression fit of the data [22]. The healing time is obtained from the slope of the linear variations, which equals $t_h^{-1/4}$, from the intercept of the solid line with $D_h = 1$, which equals $t_h^{1/4}$. Yang et. al validated this approach by fitting the data to an Arrhenius relationship with respect to temperature. The healing time determined in each case can be plotted against temperature. An interpolation of this data should be sufficient to determine the required healing time as a function of temperature.

The optimisation of the welding process in the present work concerns short flax fibre reinforced thermoplastic composites. Due to impacting factors such as absorption and diffusion in the semi-transparent part, the current model cannot directly relate the degree of healing to welding speed. Therefore, a knowledge of temperature (T_s) at the weld interface influenced by the semi-transparent part, is needed.

In the previous chapters of this thesis, effects of fibres in the semi-transparent part were addressed and temperature at the weld interface was predicted. This data also exhibits t_m. To remind, the temperature measurements were verified experimentally. From the previously gathered data of pure PLA, the value of T_s can be interpolated to find the relevant healing time ($t_{h,s}$) required.

This model is verified in the following sections. Firstly, temperature and heal time information of pure PLA with respect to welding speed is gathered experimentally. Then, temperature development at HAZ is determined with two approaches: experimental and numerical. The weld line is discredited sparsely. In the experimental approach, temperature is measured at each section of the weld with a thermocouple. On the other hand, the LTW process is numerically simulated and temperature at the same locations are noted. The explained model is then approached. These results will be compared with mechanical tests.

4.5.1 Experimental approach to predict reptation time of pure polymer

The application of the proposed model firstly requires a summary of temperature data as a function of welding speed. For this, it is required to determine suitable weld parameters that form a bond. This work continues to use pure PLA and short flax fibre reinforced PLA composite as transparent and semi-transparent parts, and PLA with 1% MB black colorant as the absorbent part. Laser transmission welding simulations of non-reinforced PLA plates is numerically performed on COMSOL Multiphysics. The laser beam is circular with Gaussian distribution of intensity. Weld parameters such as speed and power are varied while keeping the focus position constant. Thermal properties of PLA are allocated to both the components, where as coefficient of absorption is input only to the absorbent part. Adiabatic boundary conditions are applied. Maximum temperature reached at the center of the HAZ is recorded. This allows to relate the weld parameters to developed temperature with a contour plot as shown in Figure 4.7. Now, the plot can be narrowed down further with the melt temperature range of 155-170°C for PLA (Ingeo™ Biopolymer 4032D) [43].

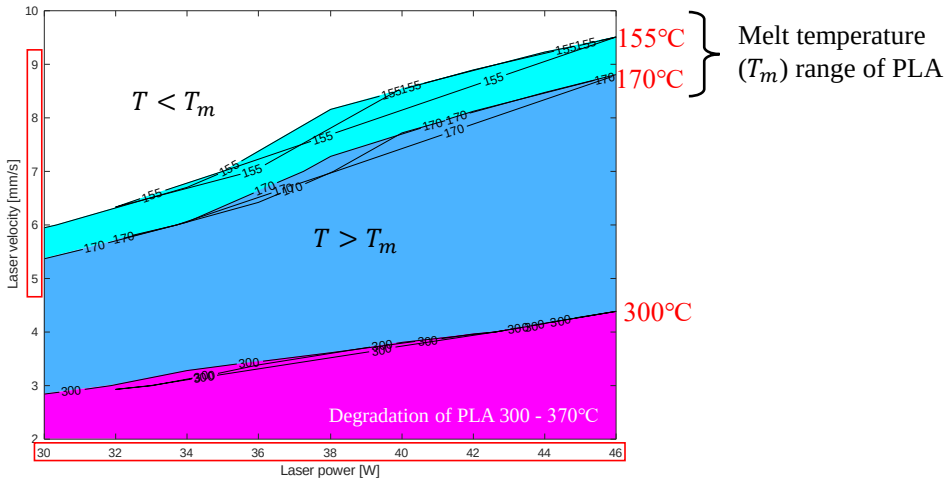

Figure 4.7: Contour plot of temperature with respect to laser speed and power

4.5.2 Fabrication of lap-shear specimens

Lap shear specimens were prepared with an overlap of 30mm between the two plates. The two plates were welded at constant laser power of 46W and focus position of 68 mm. Multiple specimens were welded with weld speed ranging from 7 mm/s to 11 mm/s over a weld line length of 15 mm (Figure 4.8). Following this, lap shear tests were carried out determine weld strength developed in each specimen. To calculate the value of D_h with Equation 4.21, σ_{max} is determined by the maximum weld strength calculated during the tensile tests. The details are listed in table 4.2.

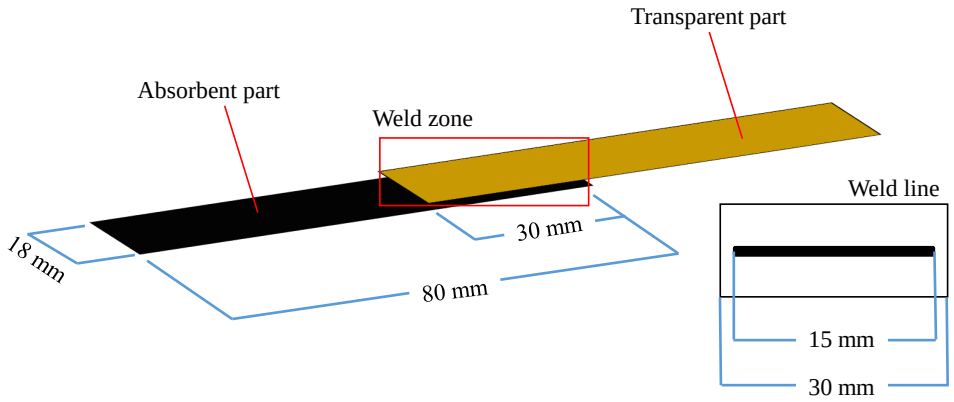

Figure 4.8: Lap-joint setup for laser transmission welding

4.5.3 Calculation healing time

To determine the temperature at the HAZ and melt time t_m, experiments were conducted to recreate the previous specimens and temperature was measured with respect to time with a thermocouple. The maximum recorded temperature for each case is listed in table 4.2.

Upon plotting the melt time against degree of healing, the healing time for each case is calculated at $D_h = 1$. Figure 4.10 shows the degree of healing plotted against time $t_m^{0.25}$ for all cases of weld speeds.

Temperature at the HAZ is evidently a function of Welding speed. In the case of opaque fibre reinforced semi-transparent parts, welding occurs at lower laser speed, as seen

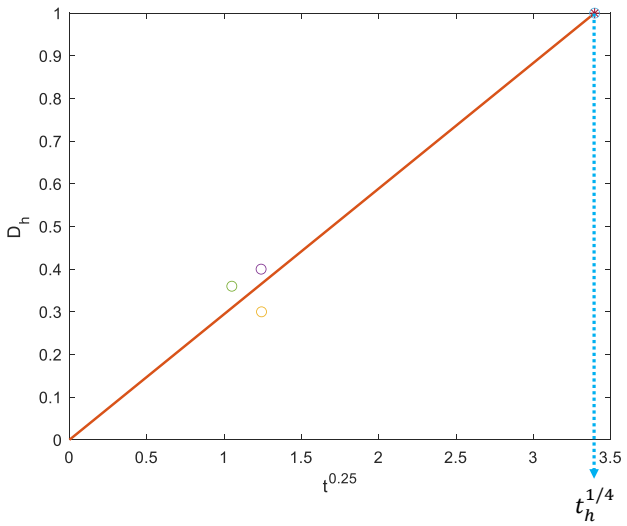

Figure 4.9: Degree of healing vs. melt time for weld speed of 7mm/s

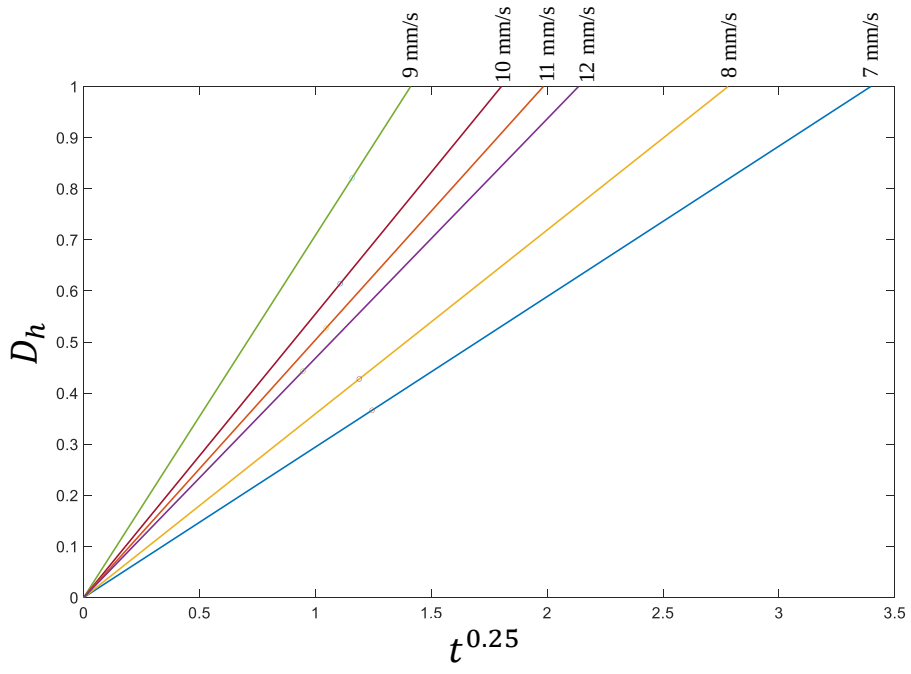

Figure 4.10: Degree of healing with respect to melt time for all cases of laser movement speed.

Table 4.1: Welding process parameters for lap shear specimens and HAZ temperature measurements

Laser power [W]	46
Laser speed range [mm/s]	7-12
Weld line length [mm]	15
Weld line width (approx.) [mm]	1.5

in the previous chapter. Hence, a comparison of transparent part and semi-transparent part cannot be made with respect to welding process speed. The reptation time calculated with each specimen must be associated with the temperature developed at the heat affected zone caused by the welding speed. Figure 4.10 plots maximum temperature against reptation time for all the specimens.

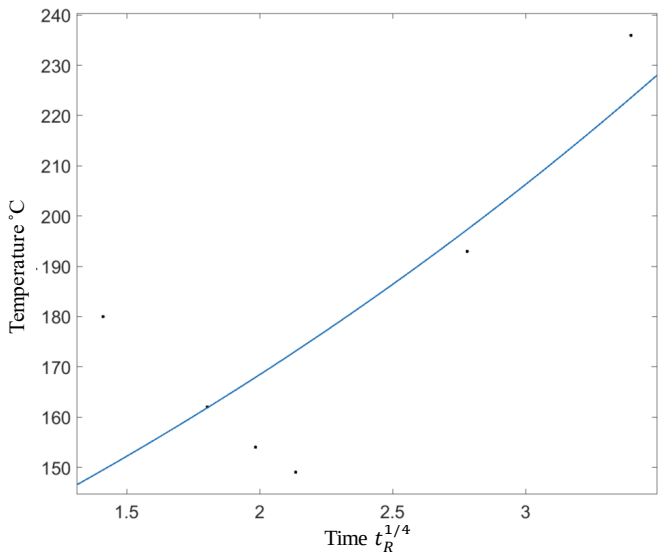

Figure 4.11: Exponential plot of the calculated reptation time as a function of maximum temperature.

To verify the model with a semi-transparent part, flax fibre reinforced PLA composite, temperature data at the weld line is collected. Due to the heterogeneity of the fibre distribution in the semi-transparent part, a non-uniform temperature distribution is expected along the weld line. To record these temperatures, the length of the weld line is discretized

Table 4.2: Experimental data to calculate reptation time of PLA at various temperatures at interface

Laser speed [mmps]	Temperature [°C]	Melt time t_m [sec]	Weld strength σ_w (Avg.) [MPa]	Dh
7	236	2.4	10.99	0.36
8	193	2	12.83	0.42
9	180	1.8	24.63	0.82
10	162	1.4	18.42	0.61
11	154	1.2	15.28	0.52
12	149	0.8	13.43	0.44

into five sections (see Figure 4.12) and temperature is measured with five thermocouples. The laser power is set to 46W. The focus position is set at 68mm while welding speed to 2mm/s. From the previously conducted experiments, it is evident that the low welding speed will not degrade the polymer at the weld interface due to diffusion and absorption properties in the semi-transparent part. A welding speed as low as 2mm/s may, in fact, cause a non-uniform weld line. The recorded temperature curves are seen in Figure 4.13.

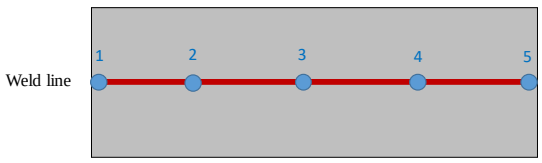

Figure 4.12: Weld line discretized in five parts.

Further calculations are made using MATLAB 2021b. The temperature at each location is interpolated in the previously processed data (Figure 4.11) and the corresponding healing time is determined. For location 1, the temperature $T_1 = 184$°C correlates with healing time $t_{h,1}^{1/4} = 1.83\text{s}.t_{h,1}^{1/4}$ can be plotted against degree of healing at $D_{h,1} = 1$. The

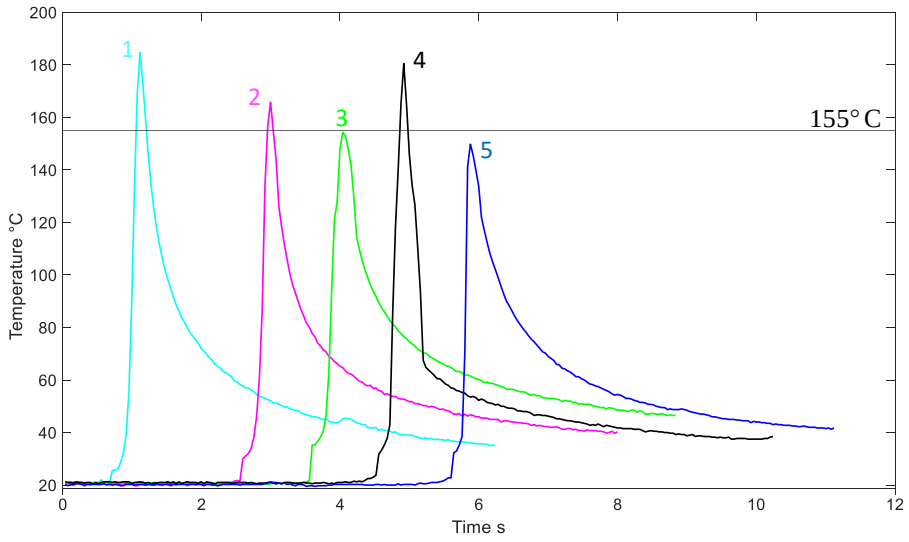

Figure 4.13: Temperature profile measured at five locations of weld line at interface of flax fibre reinforced PLA composite and pure PLA plates.

melt time at this location ($t_{m,1}$) is recorded as 0.75 seconds. Hence the degree of healing is calculated to be 0.5079.

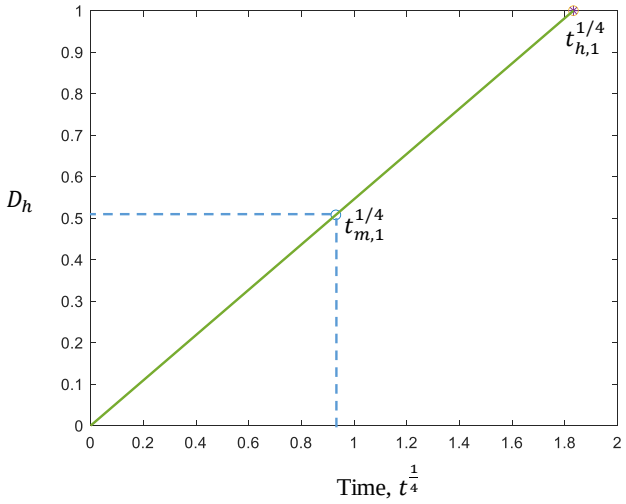

Figure 4.14: Degree of healing determined by interpolating melt time $t_{m,1}^{0.25}$ with heal time $t_{h,1}^{0.25}$ at location 1 on weld line.

The degree of healing is calculated for the remaining sections of the weld line. The summation of all sections is the eventual average strength of the weld line.

$$\sigma_n = D_{h,n} \times \sigma_{max} \tag{4.23}$$

$$\sigma_{weldline} = \frac{\sum_{x=1}^{n} \sigma_x}{n} \tag{4.24}$$

where n is the number of sections in the weld line, $n = 1$ to 5

4.6 Heat transfer simulations to determine interface temperature

Numerical simulations are carried as described in the previous chapters. 3D geometry as seen in chapter 2, is constructed with 13 layers of 13 fibre orientation tensors. It was

already gathered that the fibre orientation distribution is isotropic.

Heat transfer simulations are performed in COMSOL Multiphysics with weld parameters similar to experimental approach. The simulations are carried out as seen in chapter 3. Here, the weld line is also divided into five sections as seen in the experimental approach and Figure 4.12. The obtained temperature field is seen in Figure 4.15 The experimental

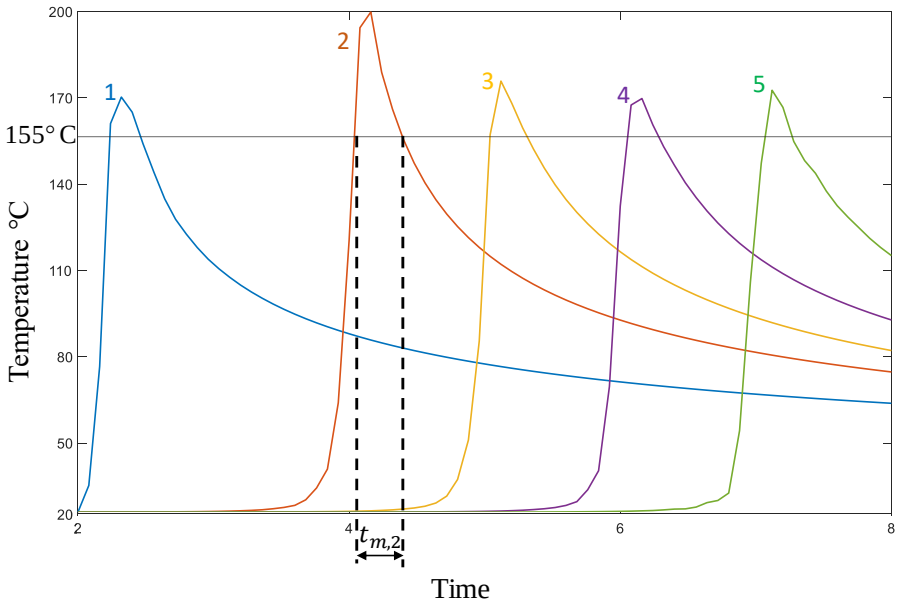

Figure 4.15: Simulated temperature development at five locations on weld line.

method is numerically replicated. Degree of healing is calculated as seen in the previous section. The referred data to determine healing time with respect to developed temperature is the same experimental data. The temperature developed at five locations along the weld line length is recorded with five data sets.

4.7 Results and discussion

To validate the experimental and simulated results, lap shear tests were performed. Lap joint specimens were made with short flax fibre reinforced PLA composite with 3mm thickness. A weld line of 15 mm is fabricated at 2mm/s speed, and 46 W laser power.

Figure 4.16: Lap shear test performed on Instron 1185 UTM.

Tensile tests were performed on Instron 1185 Universal Testing Machine at cross-head speed of 1mm/min. The tensile strength is obtained using Equation 1.8. Area of HAZ is measured after the mechanical tests. An example is seen in Figure 4.17. The average weld strength determined in all approaches is shown in Table 4.3.

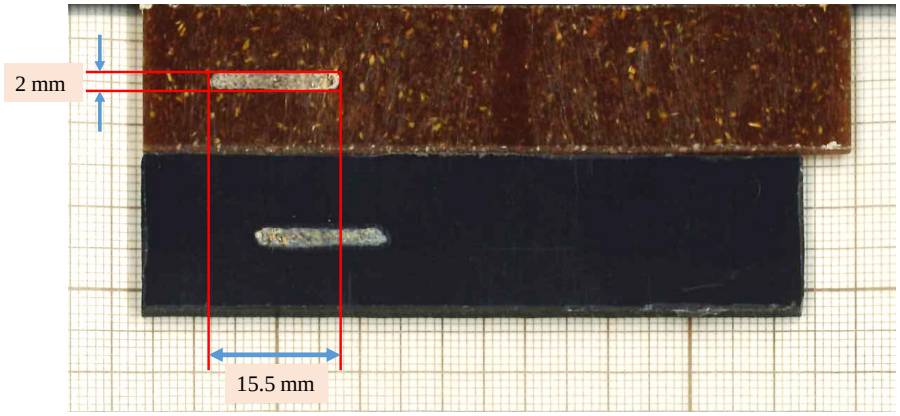

Figure 4.17: Dimensions of weld line at weld interface. Weld line produced at laser speed of 2mm/s.

The curves are fitted with a smoothing spline and a smoothing parameter of 0.96. The following observations were made:

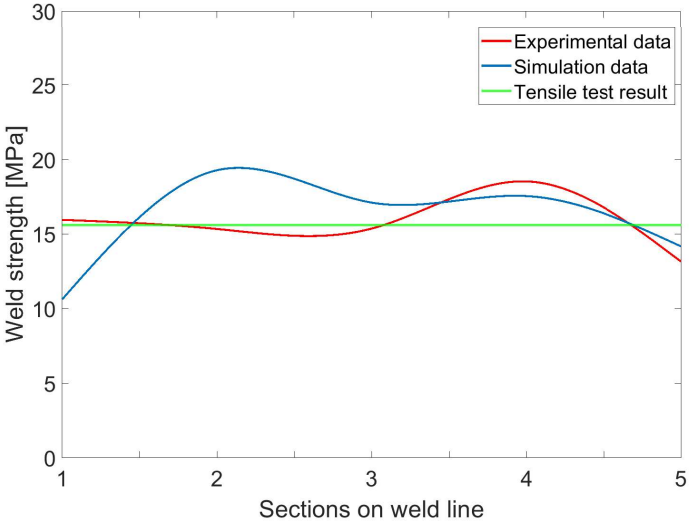

Figure 4.18: Weld strength along the weld line

Table 4.3: Comparison of weld strength predicted experimentally and numerically

	Experimentally predicted	Numerically predicted	Mechanical test result
Weld strength [MPa]	15.6706	15.7467	15.49319

1. Degree of intimate contact D_{ic} is considered to have approached unity. In the laser welding machine at IMT Nord europe, the clamping pressure is controlled automatically. Because the plates were manufactured by injection molding, the surface roughness may be comparatively low, but, it cannot be completely eliminated. The weld strength calculated with simulated inputs could be impacted as complete contact is observed at the weld interface. On the other hand, the experimental input results may be impacted, especially while measuring HAZ temperature. The thermocouple hinders the occurrence of an intimate contact.

2. The current calculations are made with one cycle of laser welding. A higher weld strength can be achieved with multiple cycles as it increases melt time.

3. Power or focus position can replace welding speed in the model. This allows a more complex and accurate prediction of weld strength as reference data increases for interpolation.

4. The approach to the model is both isothermal and non-isothermal at different steps. In the above calculations, the temperature T is the maximum recorded temperature, but the melt time t_m is not obtained at T. A more accurate result can be obtained by discretizing the temperature peak above T_m and calculating D_h at every element with isothermal approach. A summation of weld strength of all elements will be the total weld strength at a perticular location.

5. The proposed model is validated with experimental and simulation inputs. Another disadvantage of experimental inputs is the temperature measurements cannot be made at many locations on the weld line. Temperature measurements from heat transfer simulations can provide better information on temperature development, especially considering the absorption and scatter phenomena.

4.8 Conclusion

The formation of a weld was discussed following the impact of physical parameters on the weld strength. Welding parameters and molecular interdiffusion are linked to temperature

developed at the heat affected zone. The degree of bonding was calculated by considering intimate contact model and the autohesion.

Models to calculate the degree of healing at the weld interface were analysed at isothermal and non-isothermal conditions. The time required to form a good weld at various laser welding speed was calculated by keeping the laser power constant. A model was proposed based on existing healing models to predict the weld strength along the weld line length.

Weld line strength was predicted by verifying the proposed model with interface temperature data produced experimentally and numerically. The degree of healing at multiple sections of the weld line was calculated in each case and averaged. Lap-joint specimens were manufactured with semi-transparent plate of flax fibre reinforced PLA composite and absorbent part made of PLA and 1% MB black colorant. Tensile test results of the lap-joint specimens were used to validate the predicted strength of the weld line.

Chapter 5

Conclusions and perspectives

Conclusions

The process of laser transmission welding of natural fibre reinforced thermoplastic composites was presented in this dissertation. Firstly, the importance of implementation of assembly in bio-composites was studied. The challenges of short fibre inclusions in the semi-transparent part was investigated. The possibilities of numerically modelling the welding process were also studied.

Following this, the influence of fibre orientation on laser beam diffusion was determined numerically and experimentally. A method to generate 3D numerical geometries was developed by considering physical fibre morphology in an injection moulded composite material. A ray tracing simulation was implemented to analyse the diffusion of laser rays in a heterogeneous medium with respect to fibre orientation. It was concluded that fibre orientation has a large influence on lase beam diffusion and it will impact the laser intensity distribution at the weld interface.

The study of impact of fibre orientation on light diffusion allowed to generate complex numerical geometries with multi-layer orientation distribution extracted from fibre orientation tensors.

Absorption in the semi-transparent part was studied by modelling the fusion mark caused due to surface energy absorption. A method to numerically calculate absorption coefficient of the semi-transparent part was presented. The influence of fibre morphology

on absorption was studied. It was concluded that the fusion mark was caused due to one of the main welding parameters, focus position. The temperature distribution at the weld interface as a function of weld parameters was studied. Optimal welding parameters to such as welding speed and power required to heat the weld interface to a melt temperature were determined with heat transfer simulations.

The thermal properties such as density, heat capacity and thermal conductivity were homogenised numerically for the short flax fibre reinforced PLA composites which is primarily used in the investigations of this dissertation.

Also, an experimental procedure to measure interface weld temperature using thermocouple was demonstrated. The measurements were made for weld zones for pure PLA plates and PLA flax composites. The affect of welding process parameters, especially laser movement speed was studied.

A model has been proposed to determine the degree of healing based on existing isothermal and non-isothermal adhesion approaches. The process of LTW was optimised by linking weld parameters to molecular interdiffusion at the weld zone. Reptation time was calculated using mechanical tests and as a function of laser welding speed. A prediction of weld strength was made based on the interface temperature that was measured experimentally and numerically. The results were successfully validated with mechanical tests.

Perspectives

Generating 3D numerical structures was one of the most challenging tasks of this project. Moreover, the accuracy of the numerical simulations can only be reached with construction of the semi-transparent part without periodicity. Optimising the algorithm to generate 3D microstructures with computational cost effective methods would be interesting. Fibre orientation distribution of the numerical geometries were generated from fourth order orientation tensors. More accuracy in the orientation can be found with sixth-order tensors.

Apart from this, as the algorithm is capable of generating polyhedrons to represent fibre inclusions, it would be interesting to modify the inclusion shapes to represent com-

plex bundles of short natural fibres. The influence of fibre shape on laser diffusion and temperature distribution can be further studied.

The calculation of absorption coefficient in the microstructure is done at a macro scale. For more accuracy, it can be calculated at a micro scale for each micro element in the semi-transparent part. This could be computationally expensive but the periodicity of the the microstructures might be an advantage.

Lap shear tests to calculate weld strength has a disadvantage of peel effect on the weld line. To determine purely the shear strength of the weld line, other mechanical testing methods must be attempted. It is important to notice that the length and number of weld line plays a crucial role in strength formation.

In chapter 4, the degree of healing is calculated for specimens with a change in welding speed. The temperature in this case is a function of weld speed. The model could be further developed to calculate degree of healing as a function of laser power.

To make the welding of composites accessible to the manufacturing industry, applications can be created with the proposed model of weld strength calculation while taking into account the welding parameters and material proprieties. It is possible to include the manufacturing process to predict the fibre orientation in all regions of the part and analyse the laser diffusion in the weld area.

Bibliography

[1] A Hambali et al. "Material selection of polymeric composite automotive bumper beam using analytical hierarchy process". In: *Journal of Central South University of Technology* 17.2 (2010), pp. 244–256.

[2] Katsuyuki Wakabayashi et al. "Flax fiber-polyamide 6 composites via solid-state shear pulverization: Expanding the portfolio of natural fiber-reinforced thermoplastics". In: *Annual Technical Conference-ANTEC, Conference Proceedings*. Vol. 2017. 2017, pp. 616–620.

[3] AK Bledzki and Jochen Gassan. "Composites reinforced with cellulose based fibres". In: *Progress in polymer science* 24.2 (1999), pp. 221–274.

[4] James Holbery and Dan Houston. "Natural-fiber-reinforced polymer composites in automotive applications". In: *Jom* 58.11 (2006), pp. 80–86.

[5] Rainier Zah et al. "Curauá fibers in the automobile industry–a sustainability assessment". In: *Journal of cleaner production* 15.11-12 (2007), pp. 1032–1040.

[6] Benoit Cosson. "Modelling of laser welding process on thermoplastic composites". In: *Key Engineering Materials*. Vol. 651. Trans Tech Publ. 2015, pp. 1513–1518.

[7] Vijay K Stokes. "Experiments on the hot-tool welding of three dissimilar thermoplastics". In: *Polymer* 39.12 (1998), pp. 2469–2477.

[8] N Mendes et al. "Morphology and strength of acrylonitrile butadiene styrene welds performed by robotic friction stir welding". In: *Materials & Design* 64 (2014), pp. 81–90.

[9] K Panneerselvam, S Aravindan, and A Noorul Haq. "Study on resistance welding of glass fiber reinforced thermoplastic composites". In: *Materials & Design* 41 (2012), pp. 453–459.

[10] Negin Amanat, Natalie L James, and David R McKenzie. "Welding methods for joining thermoplastic polymers for the hermetic enclosure of medical devices". In: *Medical engineering & physics* 32.7 (2010), pp. 690–699.

[11] Rolf Klein. *Laser welding of plastics: materials, processes and industrial applications*. John Wiley & Sons, 2012.

[12] Ian Jones. "Laser welding of plastics". In: *Handbook of Laser Welding Technologies*. Elsevier, 2013, 280–301e.

[13] William M Steen and Jyotirmoy Mazumder. *Laser material processing*. springer science & business media, 2010.

[14] Michael J Troughton. *Handbook of plastics joining: a practical guide*. William Andrew, 2008.

[15] Verena Wippo et al. "Laser transmission welding of semi-interpenetrating polymer networks-composites". In: *Journal of Laser Applications* 29.2 (2017), p. 022407.

[16] Val Kagan, Robert Bray, and Al Chambers. "Forward to better understanding of optical characterization and development of colored polyamides for the infra-red/laser welding: part I-efficiency of polyamides for infra-red welding". In: *Journal of reinforced plastics and composites* 22.6 (2003), pp. 533–547.

[17] André Chateau Akué Asséko et al. "Laser transmission welding of composites-Part A: Thermo-physical and optical characterization of materials". In: *Infrared Physics & Technology* 72 (2015), pp. 293–299.

[18] André Chateau Akué Asséko et al. "Analytical and numerical modeling of light scattering in composite transmission laser welding process". In: *International Journal of Material Forming* 8.1 (2015), pp. 127–135.

[19] Peter Jaeschke et al. "Laser transmission welding of high-performance polymers and reinforced composites-a fundamental study". In: *Journal of Reinforced Plastics and Composites* 29.20 (2010), pp. 3083–3094.

[20] James D Van de Ven and Arthur G Erdman. "Laser transmission welding of thermoplastics—Part I: Temperature and pressure modeling". In: (2007).

[21] Richard P Wool, B-L Yuan, and OJ McGarel. "Welding of polymer interfaces". In: *Polymer Engineering & Science* 29.19 (1989), pp. 1340–1367.

[22] F Yang and R Pitchumani. "Healing of thermoplastic polymers at an interface under nonisothermal conditions". In: *Macromolecules* 35.8 (2002), pp. 3213–3224.

[23] Luis FFF Gonçalves et al. "Laser welding of thermoplastics: An overview on lasers, materials, processes and quality". In: *Infrared Physics & Technology* 119 (2021), p. 103931.

[24] HJ Silvers Jr and S Wachtell. "Perforating, welding and cutting plastic films with a continuous CO2 laser'. PA State University, Eng". In: *Proc.* 1970, pp. 88–97.

[25] Elhem Ghorbel, Giuseppe Casalino, and Stéphane Abed. "Laser diode transmission welding of polypropylene: Geometrical and microstructure characterisation of weld". In: *Materials & Design* 30.7 (2009), pp. 2745–2751.

[26] Foram Dave et al. "Laser transmission welding of semi-crystalline polymers and their composites: A critical review". In: *Polymers* 13.5 (2021), p. 675.

[27] Bappa Acherjee et al. "Empirical modeling and multi-response optimization of laser transmission welding of polycarbonate to ABS". In: *Lasers in Manufacturing and Materials Processing* 2.3 (2015), pp. 103–123.

[28] B Acherjee et al. "Selection of process parameters for optimizing the weld strength in laser transmission welding of acrylics". In: *Proceedings of the Institution of Mechanical Engineers, Part B: Journal of Engineering Manufacture* 224.10 (2010), pp. 1529–1536.

[29] Hyun Myung Shin and Hae Woon Choi. "Design of energy optimization for laser polymer joining process". In: *The International Journal of Advanced Manufacturing Technology* 75.9 (2014), pp. 1569–1576.

[30] Julian Brodhun, David Blass, and Klaus Dilger. "Laser transmission welding of thermoplastic fasteners: Influence of temperature distribution in a scanning based process". In: *Procedia CIRP* 74 (2018), pp. 533–537.

[31] Antonio Meraldo. "Introduction to bio-based polymers". In: *Multilayer Flexible Packaging*. Elsevier, 2016, pp. 47–52.

[32] Maximilian Brosda et al. "Laserwelding of biopolymers". In: *Procedia Cirp* 74 (2018), pp. 548–552.

[33] Malladi Nagalakshmaiah et al. "Biocomposites: Present trends and challenges for the future". In: *Green composites for automotive applications* (2019), pp. 197–215.

[34] Eshetie Kassegn, Frederik Desplentere, and Temesgen Berhanu. "Mechanical Properties of Short Sisal Fiber Reinforced Poly Lactic Acid (PLA) Processed by Injection Molding". In: *Branna Journal of Engineering and Technology* (2019), pp. 20–36.

[35] Pierre Ouagne et al. "Fibre extraction from oleaginous flax for technical textile applications: influence of pre-processing parameters on fibre extraction yield, size distribution and mechanical properties". In: *Procedia Engineering* 200 (2017), pp. 213–220.

[36] Marko Hyvärinen, Rowshni Jabeen, and Timo Kärki. "The modelling of extrusion processes for polymers—A review". In: *Polymers* 12.6 (2020), p. 1306.

[37] Narendra Reddy and Yiqi Yang. "Non-traditional lightweight polypropylene composites reinforced with milkweed floss". In: *Polymer International* 59.7 (2010), pp. 884–890.

[38] SM Sapuan et al. "Effects of Reinforcing Elements on the Performance of Laser Transmission Welding Process in Polymer Composites: A Systematic Review." In: *International Journal of Performability Engineering* 12.6 (2016).

[39] Maya Jacob John and Sabu Thomas. "Biofibres and biocomposites". In: *Carbohydrate polymers* 71.3 (2008), pp. 343–364.

[40] Andre Chateau Akue Asseko et al. "Effect of the developed temperature field on the molecular interdiffusion at the interface in infrared welding of polycarbonate composites". In: *Composites Part B: Engineering* 97 (2016), pp. 53–61.

[41] Myriam Dauphin and Benoit Cosson. "Modeling of thermoplastic composites laser welding-a ray tracing method associated to thermal simulation". In: *AIP Conference Proceedings*. Vol. 1769. 1. AIP Publishing LLC. 2016, p. 020010.

[42] Mariana Ilie et al. "Laser beam scattering effects in non-absorbent inhomogenous polymers". In: *Optics and Lasers in Engineering* 45.3 (2007), pp. 405–412.

[43] Mariana Ilie et al. "Through-transmission laser welding of polymers–temperature field modeling and infrared investigation". In: *Infrared Physics & Technology* 51.1 (2007), pp. 73–79.

[44] Mingliang Chen, Gene Zak, and Philip J Bates. "Effect of carbon black on light transmission in laser welding of thermoplastics". In: *Journal of Materials Processing Technology* 211.1 (2011), pp. 43–47.

[45] V Wippo et al. "Advanced laser transmission welding strategies for fibre reinforced thermoplastics". In: *Physics Procedia* 56 (2014), pp. 1191–1197.

[46] D Bagheriasl et al. "Effect of cellulose nanocrystals (CNCs) on crystallinity, mechanical and rheological properties of polypropylene/CNCs nanocomposites". In: *AIP Conference Proceedings*. Vol. 1664. 1. AIP Publishing LLC. 2015, p. 070010.

[47] John R Howell et al. *Thermal radiation heat transfer*. CRC press, 2020.

[48] Christine A Butler et al. "An analysis of mechanisms governing fusion bonding of thermoplastic composites". In: *Journal of Thermoplastic Composite Materials* 11.4 (1998), pp. 338–363.

[49] Georges Ayoub et al. "Modelling large deformation behaviour under loading–unloading of semicrystalline polymers: application to a high density polyethylene". In: *International Journal of Plasticity* 26.3 (2010), pp. 329–347.

[50] Andrzej Pawlak, Andrzej Galeski, and Artur Rozanski. "Cavitation during deformation of semicrystalline polymers". In: *Progress in polymer science* 39.5 (2014), pp. 921–958.

[51] Z Bartczak and A Galeski. "Plasticity of semicrystalline polymers". In: *Macromolecular symposia*. Vol. 294. 1. Wiley Online Library. 2010, pp. 67–90.

[52] K Schmidt-Rohr and HW Spiess. "Chain diffusion between crystalline and amorphous regions in polyethylene detected by 2D exchange carbon-13 NMR". In: *Macromolecules* 24.19 (1991), pp. 5288–5293.

[53] Anurag Pandey, Akihiko Toda, and Sanjay Rastogi. "Influence of amorphous component on melting of semicrystalline polymers". In: *Macromolecules* 44.20 (2011), pp. 8042–8055.

[54] Young Hwa Kim and Richard P Wool. "A theory of healing at a polymer-polymer interface". In: *Macromolecules* 16.7 (1983), pp. 1115–1120.

[55] RPa Wool and KM O'connor. "A theory crack healing in polymers". In: *Journal of applied physics* 52.10 (1981), pp. 5953–5963.

[56] RP Wool and KM O'Connor. "Time dependence of crack healing". In: *Journal of polymer science: Polymer letters edition* 20.1 (1982), pp. 7–16.

[57] PJ Bates, TB Okoro, and M Chen. "Thermal degradation of PC and PA6 during laser transmission welding". In: *Welding in the World* 59.3 (2015), pp. 381–390.

[58] LS Mayboudi et al. "A two-dimensional thermal finite element model of laser transmission welding for T joint". In: *Journal of Laser Applications* 18.3 (2006), pp. 192–198.

[59] LS Mayboudi et al. "A 3-D thermal model for spot laser transmission welding of thermoplastics". In: *Welding in the World* 51.1 (2007), pp. 74–78.

[60] Manfred Geiger, T Frick, and Michael Schmidt. "Optical properties of plastics and their role for the modelling of the laser transmission welding process". In: *Production Engineering* 3.1 (2009), pp. 49–55.

[61] GN Labeas, GA Moraitis, and Ch V Katsiropoulos. "Optimization of laser transmission welding process for thermoplastic composite parts using thermo-mechanical simulation". In: *Journal of composite materials* 44.1 (2010), pp. 113–130.

[62] Mirko Aden. "Influence of the laser-beam distribution on the seam dimensions for laser-transmission welding: a simulative approach". In: *Lasers in Manufacturing and Materials Processing* 3.2 (2016), pp. 100–110.

[63] Andre Chateau Akue Asseko et al. "Thermal modeling in composite transmission laser welding process: light scattering and absorption phenomena coupling". In: *ESAFORM 2014-17th Conference of the European Scientific Association on Material forming*. Vol. 611. 2014, p–1560.

[64] Benoit Cosson et al. "3D modeling of thermoplastic composites laser welding process–A ray tracing method coupled with finite element method". In: *Optics & Laser Technology* 119 (2019), p. 105585.

[65] Bappa Acherjee et al. "Optimal process design for laser transmission welding of acrylics using desirability function analysis and overlay contour plots". In: *International Journal of Manufacturing Research* 6.1 (2011), pp. 49–61.

[66] LS Mayboudi et al. "Infrared observations and finite element modeling of a laser transmission welding process". In: *Journal of Laser Applications* 21.3 (2009), pp. 111–118.

[67] Bappa Acherjee et al. "Application of artificial neural network for predicting weld quality in laser transmission welding of thermoplastics". In: *Applied soft computing* 11.2 (2011), pp. 2548–2555.

[68] MR Nakhaei, NB Mostafa Arab, and F Kordestani. "Modeling of weld lap-shear strength for laser transmission welding of thermoplastic using artificial neural network". In: *Advanced materials research*. Vol. 445. Trans Tech Publ. 2012, pp. 454–459.

[69] L Yan et al. "Characterizing Temporary Bonding Adhesives Using a Wedge Test". In: *12th International Conference on Fracture 2009, ICF-12*. 2009, pp. 6347–6355.

[70] J Renart et al. "Mode I fatigue behaviour and fracture of adhesively-bonded fibre-reinforced polymer (FRP) composite joints for structural repairs". In: *Fatigue and fracture of adhesively-bonded composite joints*. Elsevier, 2015, pp. 121–147.

[71] Jakub Rzeczkowski. "An experimental analysis of the end-notched flexure composite laminates beams with elastic couplings". In: *Continuum Mechanics and Thermodynamics* 33.6 (2021), pp. 2331–2343.

[72] Jörgen Bergström. "Experimental characterization techniques". In: *Mechanics of Solid Polymers* (2015), pp. 19–114.

[73] France Chabert et al. "Transmission Laser Welding of Polyamides: Effect of Process Parameter and Material Properties on the Weld Strength". In: *Procedia Manufacturing* 47 (2020), pp. 962–968.

[74] Mariana Ilie et al. "Diode laser welding of ABS: Experiments and process modeling". In: *Optics & Laser Technology* 41.5 (2009), pp. 608–614.

[75] André Chateau Akué Asséko et al. "Laser transmission welding of composites–Part B: Experimental validation of numerical model". In: *Infrared Physics & Technology* 73 (2015), pp. 304–311.

[76] Fransisco Folgar and III Charles L. Tucker. "Orientation Behavior of Fibers in Concentrated Suspensions". In: *Journal of Reinforced Plastics and Composites* 3.2 (1984), pp. 98–119.

[77] M Cengiz Altan et al. "Numerical prediction of three-dimensional fiber orientation in Hele-Shaw flows". In: *Polymer Engineering & Science* 30.14 (1990), pp. 848–859.

[78] Benoit Cosson, Mylène Deléglise, and Wolfgang Knapp. "Numerical analysis of thermoplastic composites laser welding using ray tracing method". In: *Composites Part B: Engineering* 68 (2015), pp. 85–91.

[79] J Nabialek. "Modeling of fiber orientation during injection molding process of polymer composites". In: *Kompozyty* 11.4 (2011), pp. 347–351.

[80] MJ Folkes and DAM Russell. "Orientation effects during the flow of short-fibre reinforced thermoplastics". In: *Polymer* 21.11 (1980), pp. 1252–1258.

[81] Michel Vincent et al. "Description and modeling of fiber orientation in injection molding of fiber reinforced thermoplastics". In: *Polymer* 46.17 (2005), pp. 6719–6725.

[82] Brent E VerWeyst et al. "Fiber orientation in 3-D injection molded features". In: *International Polymer Processing* 14.4 (1999), pp. 409–420.

[83] Radmir Karamov et al. "Micro-CT based structure tensor analysis of fibre orientation in random fibre composites versus high-fidelity fibre identification methods". In: *Composite Structures* 235 (2020), p. 111818.

[84] PA O'Connell and RA Duckett. "Measurements of fibre orientation in short-fibre-reinforced thermoplastics". In: *Composites science and technology* 42.4 (1991), pp. 329–347.

[85] Colin Eberhardt and Ashley Clarke. "Fibre-orientation measurements in short-glass-fibre composites. Part I: automated, high-angular-resolution measurement by confocal microscopy". In: *Composites Science and Technology* 61.10 (2001), pp. 1389–1400.

[86] B Mlekusch. "Fibre orientation in short-fibre-reinforced thermoplastics II. Quantitative measurements by image analysis". In: *Composites Science and Technology* 59.4 (1999), pp. 547–560.

[87] Suresh G Advani and Charles L Tucker III. "The use of tensors to describe and predict fiber orientation in short fiber composites". In: *Journal of rheology* 31.8 (1987), pp. 751–784.

[88] André Chateau Akué Asséko et al. "Numerical analysis of effective thermal conductivity of plastic foams". In: *Journal of Materials Science* 51.20 (2016), pp. 9217–9228.

[89] Swantje Bargmann et al. "Generation of 3D representative volume elements for heterogeneous materials: A review". In: *Progress in Materials Science* 96 (2018), pp. 322–384.

[90] Karen Soete et al. "Variability of flax fibre morphology and mechanical properties in injection moulded short straw flax fibre-reinforced PP composites". In: *Journal of Composite Materials* 51.23 (2017), pp. 3337–3349.

[91] Joaquim S Cintra Jr and Charles L Tucker III. "Orthotropic closure approximations for flow-induced fiber orientation". In: *Journal of Rheology* 39.6 (1995), pp. 1095–1122.

[92] Du Hwan Chung and Tai Hun Kwon. "Improved model of orthotropic closure approximation for flow induced fiber orientation". In: *Polymer composites* 22.5 (2001), pp. 636–649.

[93] DA Jack and DE Smith. "An invariant based fitted closure of the sixth-order orientation tensor for modeling short-fiber suspensions". In: *Journal of Rheology* 49.5 (2005), pp. 1091–1115.

[94] Suresh G Advani and Charles L Tucker III. "Closure approximations for three-dimensional structure tensors". In: *Journal of Rheology* 34.3 (1990), pp. 367–386.

[95] Delphine Dray, Pierre Gilormini, and Gilles Régnier. "Comparison of several closure approximations for evaluating the thermoelastic properties of an injection molded short-fiber composite". In: *Composites Science and Technology* 67.7-8 (2007), pp. 1601–1610.

[96] William Aspray. "The transformation of numerical analysis by the computer: An example from the work of John von Neumann". In: *Institutions and Applications*. Elsevier, 1989, pp. 306–322.

[97] C Christiansen. "Absolute Bestimmung des Emissions-und Absorptionsvermögens für Wärme". In: *Annalen der Physik* 255.6 (1883), pp. 267–283.

[98] Benoit Cosson et al. "Infrared heating stage simulation of semi-transparent media (PET) using ray tracing method". In: *International Journal of Material Forming* 4.1 (Mar. 2011), pp. 1–10.

[99] Mirko Aden, Andreas Roesner, and Alexander Olowinsky. "Optical characterization of polycarbonate: Influence of additives on optical properties". In: *Journal of Polymer Science Part B: Polymer Physics* 48.4 (2010), pp. 451–455.

[100] Juan Manuel Vazquez-Martinez et al. "Evaluation of the joining response of biodegradable polylactic acid (PLA) from fused deposition modeling by infrared laser irradiation". In: *Polymers* 12.11 (2020), p. 2479.

[101] David Grewell, Paul Rooney, and Val A Kagan. "Relationship between optical properties and optimized processing parameters for through-transmission laser welding of thermoplastics". In: *Journal of Reinforced plastics and Composites* 23.3 (2004), pp. 239–247.

[102] VA Kagan, RG Bray, and WP Kuhn. "Laser transmission welding of semi-crystalline thermoplastics—Part I: Optical characterization of nylon based plastics". In: *Journal of reinforced plastics and composites* 21.12 (2002), pp. 1101–1122.

[103] E Weingartner et al. "Absorption of light by soot particles: determination of the absorption coefficient by means of aethalometers". In: *Journal of Aerosol Science* 34.10 (2003), pp. 1445–1463.

[104] Wolfgang Knapp et al. "Laser-bonding of long fiber thermoplastic composites for structural assemblies". In: *Physics Procedia* 5 (2010), pp. 163–171.

[105] Janis Sliseris, Libo Yan, and Bohumil Kasal. "Numerical modelling of flax short fibre reinforced and flax fibre fabric reinforced polymer composites". In: *Composites part B: engineering* 89 (2016), pp. 143–154.

[106] Benoit Cosson, André Chateau Akué Asséko, and Myriam Dauphin. "A non-destructive optical experimental method to predict extinction coefficient of glass fibre-reinforced thermoplastic composites". In: *Optics & Laser Technology* 106 (2018), pp. 215–221.

[107] I. Jones. "13 - Transmission laser welding strategies for medical plastics". In: *Joining and Assembly of Medical Materials and Devices*. Ed. by Y. Zhou and Mark D. Breyen. Woodhead Publishing Series in Biomaterials. Woodhead Publishing, 2013, 344–371e. ISBN: 978-1-84569-577-4.

[108] Marcus Warwick and Marcus Gordon. "Application studies using through-transmission laser welding of polymers". In: *Joining Plastics* (2006), pp. 25–26.

[109] *Le Spécialiste du verre technique et innovant*. URL: `http://www.verrehaget.fr/`.

[110] A Roesner, M Aden, and A Olowinsky. "Laser Transmission Welding Under Special Consideration of Scattering". In: *Proceedings of the Fifth International WLT-Conference on Lasers in Manufacturing, Munich*. 2009, p. 2.

[111] Suthaphat Kamthai and Rathanawan Magaraphan. "Thermal and mechanical properties of polylactic acid (PLA) and bagasse carboxymethyl cellulose (CMCB) composite by adding isosorbide diesters". In: *AIP Conference Proceedings* 1664.1 (2015), p. 060006.

[112] Oldrich Zmeskal et al. "Thermal properties of samples prepared from polylactic acid by 3D printing". In: *AIP Conference Proceedings* 2305.1 (2020), p. 020022.

[113] Romain Léger et al. "Modeling natural fiber composites microstructures for predicting their water aging". In: *18th European Conference on Composites Materials*. 2018.

[114] *CADMOULD - plastic injection molding simulation software*. URL: `https://www.simcon.com/cadmould`.

[115] Zhidong Han and Alberto Fina. "Thermal conductivity of carbon nanotubes and their polymer nanocomposites: A review". In: *Progress in polymer science* 36.7 (2011), pp. 914–944.

[116] DM Bigg. "Thermal conductivity of heterophase polymer compositions". In: *Thermal and electrical conductivity of polymer materials* (1995), pp. 1–30.

[117] Hongyu Chen et al. "Thermal conductivity of polymer-based composites: Fundamentals and applications". In: *Progress in Polymer Science* 59 (2016), pp. 41–85.

[118] Hanna-Riitta Kymäläinen et al. "Quality of Linum usitatissimum L.(flax and linseed) and Cannabis sativa L.(fibre hemp) during the production chain of fibre raw material for thermal insulations". In: (2004).

[119] LJ Bastien and JW Gillespie Jr. "A non-isothermal healing model for strength and toughness of fusion bonded joints of amorphous thermoplastics". In: *Polymer Engineering & Science* 31.24 (1991), pp. 1720–1730.

[120] URL: `https://doc.comsol.com/5.5/doc/com.comsol.help.heat/heat_ug_interfaces.08.16.html`.

[121] Christopher Mark Stokes-Griffin et al. "Thermal modelling of the laser-assisted thermoplastic tape placement process". In: *Journal of Thermoplastic Composite Materials* 28.10 (2015), pp. 1445–1462.

[122] Woo Il Lee and George S Springer. "A model of the manufacturing process of thermoplastic matrix composites". In: *Journal of composite materials* 21.11 (1987), pp. 1017–1055.

[123] R Pitchumani et al. "Analysis of transport phenomena governing interfacial bonding and void dynamics during thermoplastic tow-placement". In: *International journal of heat and mass transfer* 39.9 (1996), pp. 1883–1897.

[124] Isabel Martin et al. "Advanced Thermoplastic Composite Manufacturing by In-Situ Consolidation: A Review". In: *Journal of Composites Science* 4.4 (2020), p. 149.

[125] Khaled Yassin and Mehdi Hojjati. "Processing of thermoplastic matrix composites through automated fiber placement and tape laying methods: A review". In: *Journal of Thermoplastic Composite Materials* 31.12 (2018), pp. 1676–1725.

[126] AC Loos and PH Dara. "Modeling the curing process of thick-section autoclave cured composites". In: *Proceedings of the 2nd Annual Review of the Center for Composite Materials and Structures* (1985).

[127] F Yang and R Pitchumani. "A fractal Cantor set based description of interlaminar contact evolution during thermoplastic composites processing". In: *Journal of materials science* 36.19 (2001), pp. 4661–4671.

[128] Gilles Regnier and Steven Le Corre. "Modeling of thermoplastic welding". In: (2016).

[129] F Yang and R Pitchumani. "Interlaminar contact development during thermoplastic fusion bonding". In: *Polymer Engineering & Science* 42.2 (2002), pp. 424–438.

[130] Christophe Ageorges et al. "Characteristics of resistance welding of lap shear coupons.: Part II. Consolidation". In: *Composites Part A: Applied Science and Manufacturing* 29.8 (1998), pp. 911–919.

[131] D Grewell and A Benatar. "Coupled temperature, diffusion and squeeze flow model for interfacial healing predictions". In: *Annual Technical Conference for the Society of Plastic Engineers Proceedings, Society of Plastic Engineers, Brookfield, CT.* 2006.

[132] Jakob Onken, Steffen Verwaayen, and Christian Hopmann. "Evaluation of healing models to predict the weld line strength of the amorphous thermoplastic polystyrene by injection molding simulation". In: *Polymer Engineering & Science* 61.3 (2021), pp. 754–766.

[133] Huagui Zhang, Khalid Lamnawar, and Abderrahim Maazouz. "Rheological modeling of the diffusion process and the interphase of symmetrical bilayers based on PVDF and PMMA with varying molecular weights". In: *Rheologica acta* 51.8 (2012), pp. 691–711.

[134] Pierre-Giles De Gennes. "Reptation of a polymer chain in the presence of fixed obstacles". In: *The journal of chemical physics* 55.2 (1971), pp. 572–579.

[135] OA Ezekoye et al. "Polymer weld strength predictions using a thermal and polymer chain diffusion analysis". In: *Polymer Engineering & Science* 38.6 (1998), pp. 976–991.

[136] H H_ Kausch and M Tirrell. "Polymer interdiffusion". In: *Annual Review of Materials Research* 19 (1989), pp. 341–377.

[137] Sang-Gook Kim and Nam P Suh. "Performance prediction of weldline structure in amorphous polymers". In: *Polymer Engineering & Science* 26.17 (1986), pp. 1200–1207.

[138] ULF Gedde. *Polymer physics*. Springer Science & Business Media, 1995.

[139] Masao Doi, Samuel Frederick Edwards, and Samuel Frederick Edwards. *The theory of polymer dynamics*. Vol. 73. oxford university press, 1988.

[140] Chenyang Liu et al. "Evaluation of different methods for the determination of the plateau modulus and the entanglement molecular weight". In: *Polymer* 47.13 (2006), pp. 4461–4479.

[141] Joseph Bartolai, Timothy W Simpson, and Renxuan Xie. "Predicting strength of thermoplastic polymer parts produced using additive manufacturing". In: *2016 International Solid Freeform Fabrication Symposium*. University of Texas at Austin. 2016.

[142] Remko Akkerman, Mark Bouwman, and Sebastiaan Wijskamp. "Analysis of the thermoplastic composite overmolding process: Interface strength". In: *Frontiers in Materials* 7 (2020), p. 27.

[143] Arthur Levy, Steven Le Corre, and Arnaud Poitou. "Ultrasonic welding of thermoplastic composites: a numerical analysis at the mesoscopic scale relating processing parameters, flow of polymer and quality of adhesion". In: *International Journal of Material Forming* 7.1 (2014), pp. 39–51.

Abstract

Laser transmission welding of thermoplastics requires the optimisation of interfacial adhesion at the weld joint. In this regard, the process modelling, and the development of numerical simulation tools are indispensable to optimize the mechanical strength of the weld joint. The task is more difficult in the case of highly heterogeneous and anisotropic composite materials. Moreover, the laser transmission is still difficult in the case of opaque or semi-transparent media such as natural fibre reinforced thermoplastic composites. The thermal and optical properties of composites depend on the properties and morphology of the constituents such as fibres and polymer, which can affect the transmission spectrum in the infrared range. The absorption and refraction of laser ray propagation in the composite materials lead to a reduction of the transmitted energy arriving at the weld interface, which directly influences the quality of the weld and its mechanical performance.

In this dissertation, the effect of absorption and diffusion phenomena on the development of temperature field at the weld interface is analysed numerically and experimentally. Considering the fibre orientation, shape, length and volume fraction, numerical 3D geometries representing composite materials are generated to simulate the propagation of laser rays with “Ray tracing” algorithm. Numerical models to estimate the strength of weld are presented while considering the influence of welding parameters (such as laser power, feeding speed and focus position), material properties and molecular interdiffusion at the weld interface. The weld bonding strength is measured by mechanical tests and their results are compared with numerical modelling results.

Keywords: Laser transmission welding, natural fibre reinforced composites, ray tracing, molecular interdiffusion

Résume

Le soudage par transmission laser des thermoplastiques nécessite l'optimisation de l'adhérence interfaciale au niveau du joint de soudure. A cet égard, la modélisation du procédé et le développement d'outils de simulation numérique sont indispensables pour optimiser la résistance mécanique du joint de soudure. La tâche est plus difficile dans le cas de matériaux composites très hétérogènes et anisotropes. De plus, la transmission laser est encore difficile dans le cas de milieux opaques ou semi-transparents tels que les composites thermoplastiques renforcés de fibres naturelles. Les propriétés thermiques et optiques des composites dépendent des propriétés et de la morphologie des constituants tels que les fibres et le polymère, qui peuvent affecter le spectre de transmission dans le domaine infrarouge. L'absorption et la réfraction de la propagation du rayon laser dans les matériaux composites conduisent à une réduction de l'énergie transmise arrivant à l'interface de soudure, ce qui influence directement la qualité de la soudure et ses performances mécaniques.

Dans cette thèse, l'effet des phénomènes d'absorption et de diffusion sur le développement du champ de température à l'interface de la soudure est analysé numériquement et expérimentalement. Compte tenu de l'orientation, de la forme, de la longueur et de la fraction volumique des fibres, des géométries numériques 3D représentant les matériaux composites sont générées pour simuler la propagation des rayons laser avec l'algorithme de "Ray tracing". Des modèles numériques pour estimer la résistance de la soudure sont présentés tout en tenant compte de l'influence des paramètres de soudage (tels que la puissance du laser, la vitesse d'alimentation et la position du foyer), les propriétés du matériau et l'interdiffusion moléculaire à l'interface de la soudure. La résistance de la soudure est mesurée par des essais mécaniques et leurs résultats sont comparés aux résultats de la modélisation numérique.

Mots clés : Soudage par transmission laser, matériaux composites, ray tracing, interdiffusion moléculaire